Drug Research Program
Faculty of Pharmacy
University of Helsinki
Finland

MICROFABRICATION OF ORGANICALLY MODIFIED CERAMICS FOR BIO-MEMS

Ashkan Bonabi

ACADEMIC DISSERTATION

To be presented, with the permission of the Faculty of Pharmacy of
the University of Helsinki, for public examination in lecture room 1041, Biocenter 2,
on 10 January 2020, at 12 noon.

Helsinki 2020

Supervised by:

Dr. Tiina Sikanen
Drug Research Program
Faculty of Pharmacy
University of Helsinki
Finland

Dr. Ville Jokinen
Department of Chemistry and Materials Science
School of Chemical Engineering
Aalto University
Finland

Professor Sami Franssila
Department of Chemistry and Materials Science
School of Chemical Engineering
Aalto University
Finland

Reviewed by:

Associate Professor Regina Luttge
Department of Mechanical Engineering
Eindhoven University of Technology
Netherland

Professor Peter Ertl
Institut für Angewandte Synthesechemie
Technische Universität Wien
Austria

Opponent:

Professor Petra Dittrich
Department of Biosystems Science and Engineering
ETH Zürich
Switzerland

ISBN 978-951-51-5765-2 (paperback)
ISBN 978-951-51-5766-9 (PDF)

http://ethesis.helsinki.fi

Helsinki University, Unigrafia Helsinki 2019

ABSTRACT

A Bio-Micro-Electro-Mechanical-System (Bio-MEMS) is a miniaturized device that has mechanical, optical and/or electrical components for biomedical operations. High sensitivity, rapid response and integration capabilities are the main reasons for their attraction to researchers and adaptation of Bio-MEMS technology for many applications. Although the recent progress in microfabrication techniques has enabled a high degree of Bio-MEMS integration, many challenges remain. For example, extending the conventional cell monolayer cultures into 3D in vitro organ models often demands fabrication of round-cross sectional microstructures (microchannels and microwells) and integration of embedded metal-sensing elements. Owing to their low cost and the ease of the fabrication process, polymers have gained much attention in terms of biological microfluidic applications. Organically Modified Ceramics (ORMOCER) are hybrid inorganic-organic polymers, a new class of negative tone photoresist. Among polymers, ORMOCERs exhibit great potential with a view to biological microfluidic applications based on their inherent biocompatibility, transparency and mechanical stability.

In this thesis, ORMOCER microfabrication methods were developed for implementation of optical, electrical and structural elements that are crucial for biological applications. A novel method, relying on controlled over-exposure of Ormocomp (a commercial formulation of ORMOCERs) was introduced for fabrication of tunable round cross-sectional microstructures, including microchannels (subprojects I-III) and microwells (subproject IV). Moreover, ORMOCER metallization was examined from the perspective of integration of embedded sensing elements (micromirrors and electrodes) into ORMOCER microfluidic channels to facilitate on-chip fluorescence (subprojects I and II) and electrochemical (subproject III) detection as well as electrical impedance spectroscopy (subproject IV). Metal adhesion, step coverage and bonding of embedded metal elements were addressed and new processes developed for various thin-film metals (subprojects III and IV). The round cross-sectional shape of the microchannel was exploited for implementation of thin-film reflective metal elements as concave micromirrors for optical detection of single cells, whereas the round shape of the microwells was applied to microfluidic three-dimensional (3D; spheroid) cell cultures. In addition to topography, the inherent surface properties of ORMOCERs were modified to allow for regulation of cell adhesion. As a result, cell monolayers (2D) and spheroids (3D) could be cultured side-by-side in a single microfluidic channel with non-invasive online impedance-based (monolayer) and optical monitoring (spheroids) of cell proliferation.

PREFACE

This work was carried out at the University of Helsinki, Faculty of Pharmacy, from October 2013-February 2019, in the context of the CUMTAS project, receiving funding from the European Research Council under the European Union's Seventh Framework Programme. I am grateful to Dr. Tiina Sikanen who recruited me and supplied me with the opportunity to become familiar with microfabrication and microfluidic fields. Without her help and support, it would have been impossible to finish my PhD project. I also wish to express my full appreciation to Dr. Ville Jokinen owing to his technical assistance and for sharing his experience surrounding microfabrication. In addition, I would like to sincerely offer my gratitude to Prof. Sami Franssila, who was always supportive and helped me integrate into his group. I am also thankful for the travel support provided by the Doctoral Program in Materials Research and Nanoscience (MATRENA). Further, I wish to express my appreciation to all co-authors for their collaboration and contributions. Genuine thanks go to Sari Tähkä, Elisa Ollikainen, Markus Haapala, Päivi Tammela, Salvatore Cito and Päivi Järvinen. Without their help, I could not have finished my doctorate. Special thanks belong to Sari who was not only a colleague but a good friend to me at all times. Finally, I am thankful to the members of the Chemical Microsystems research group (CheMiSys) and Aalto Microfabrication Group (MFG group) for all their support. Huge thanks also go to Gowtham Sathyanarayanan, Ciler Özen, Kati Piironen, Tea Pihlaja, Iiro Kiiski, Sanja Karlsson, Giulia Torrieri, Sasha Hoshian, Farzin Jahangiri, Anas Al-Azawi, Anand Tatikonda, Ville Rontu and Joonas Heikkinen, who fostered a great atmosphere within the various workplaces. Special thanks are also due to the cleanroom facility individuals, Päivikki Repo, Paula Kettula, Erkki Halonen and Victor Ovchinnikov, who assisted me in using all the cleanroom equipment.

My sincere appreciation to the Erasmus Student Network (ESN) of Helsinki University, which provided me the opportunity to participate in social events - they made my life colorful and active throughout the entirety of my PhD work.

Moreover, I would like to express my full gratitude to Professor Sohrab Behnia, my first supervisor at the BSc level and Meer Taher Shabani Rad who motivated me to continue in the field of Biomedical Engineering. Finally, I am deeply indebted to my Mother, my Father and my Brother, all of whom supported me from far away. Without their sacrifices, it would not have been possible to continue toward my ambitions.

CONTENTS

LIST OF ORIGINAL PUBLICATIONS

This thesis is based on the following publications:

I. Ashkan Bonabi, Salvatore Cito, Päivi Tammela, Ville Jokinen, Tiina M. Sikanen. "Fabrication of concave micromirrors for single cell imaging via controlled over-exposure of organically modified ceramics in single step lithography", Biomicrofluidics 2017, 11(3), 034118 (11 pp), doi: 10.1063/1.4985653

II. Ashkan Bonabi*, Sari Tähkä*, Markus Haapala, Ville P. Jokinen, Tiina M. Sikanen. ''Multiplying the optical signal of microfluidic separation chips with integrated thin-film micromirrors'', manuscript, 2019. (*Both authors contributed equally to this manuscript).

III. Ashkan Bonabi, Sari Tähkä, Elisa Ollikainen, Ville Jokinen, Tiina Sikanen. "Metallization of Organically Modified Ceramics for Microfluidic Electrochemical Assays'', Micromachines 2019, 10, 605 12 pp), doi: 10.3390/mi10090605.

IV. Päivi Järvinen*, Ashkan Bonabi*, Ville P. Jokinen, Tiina M. Sikanen. "Simultaneous Culturing of Cell Monolayers and Spheroids on a Single Microfluidic Device for Bridging the Gap between 2D and 3D Cell Assays in Drug Research'', manuscript, 2019.(*Both authors contributed equally to this manuscript).

The publications are hereafter referred to in the text by roman numerals.

Author's contribution to the publications included in this thesis:

I. The microchips and the experiments were designed by the author together with Dr. Ville P. Jokinen and Dr. Tiina M. Sikanen. The microdevice fabrication and related method development as well as all data handling was carried out by the author. The numerical script (Matlab) was conducted by Dr. Salvatore Cito and the cell culturing Prof. Päivi Tammela. The publication was written by the author with contributions from coauthors.

II. The microchips and experiments were designed by the author together with Dr. Ville P. Jokinen and Dr. Tiina M. Sikanen. The microdevice fabrication and related method development was carried out by the author. The microfluidic separations were performed by Dr. Sari Tähkä and the optical simulation by Dr. Markus Haapala. The publication was written by the author with contributions from coauthors.

III. The microchips and experiments were designed by the author together with Dr. Ville P. Jokinen and Dr. Tiina M. Sikanen. The microdevice fabrication and related method development as well as all data handling (apart from electrochemical assays) were carried out by the author. Microfluidic electrochemical detection method development was conducted by MSc Elisa Ollikainen and the proof-of-concept experiments by Dr. Sari Tähkä. The publication was written by the author with contributions from coauthors.

IV. The microchips and experiments were designed by the author together with Dr. Päivi Järvinen, Dr. Ville P. Jokinen and Dr. Tiina M. Sikanen. The microdevice fabrication and related method development and data handling was carried out by the author. The cell culturing and related data handling were performed by Dr. Päivi Järvinen. The publication was written by Dr. Päivi Järvinen with contributions from the author (microfabrication) and other coauthors.

ABBREVIATIONS

2PP	two-photon polymerization
Bio-MEMS	biological electromechanical systems
CI	cell index
CVD	chemical vapour deposition
ECIS	electrical cell impedance sensing
ECM	extra cellular matrix
EIS	electric impedance spectroscopy
HMDS	hexamethyldisilazane
ITO	indium tin oxide
LIF	laser-induced fluorescence
LOD	limit of detection
MEMS	micro-electro-mechanical system
ORMOCER	organically modified ceramic
PCR	polymerase chain reaction
PDMS	polydimethylsiloxane
PECVD	plasma-enhanced chemical vapor deposition
PEG	polyethyleneglycol
PI	polyimide
PLGA	poly (lactic-co-glycolic acid)
PMMA	poly (methyl methacrylate)
PVD	physical vapour deposition
SEM	scanning electron microscope
UV	ultraviolet

1 INTRODUCTION

Understanding the biological behavior of cellular functions and molecular processes are key requirements in many research areas, such as drug discovery and development extending from, drug delivery, distribution, metabolism, and elimination processes to underlying pharmacology. The sensitivity and selectivity of the monitoring and detection techniques are keys for discovering new information about cellular and molecular functions. Biological micro-electro-mechanical systems (Bio-MEMS) are devices featuring micrometer-dimensions that integrate electrical and optical sensors and structural elements achieved via microfabrication techniques and applied to medical and biological studies [1]. Their sensitivity is typically higher, and analysis times shorter in comparison to traditional laboratory methods [2].

Customarily, MEMS fabrication processes were developed on glass and silicon wafers. Since 1990's, polymer microfabrication methods were introduced for Bio-MEMS applications, revolutionizing the field [3]. Polymers became attractive because they are low cost, sometimes biocompatible and feasible for microfabrication by rapid prototyping methods [4, 5]. In addition to biocompatibility, transparency (in contrast to silicon) along with acceptable mechanical and thermal stability are the main reasons for using polymers as the material of choice for Bio-MEMS. By definition, Bio-MEMS covers applications ranging from small-molecule diagnostics to tissue engineering and medical implants. This thesis discusses the current state-of-the-art of microfabrication materials and methods used for implementation of biosensors and microfluidic cell-culturing platforms. The applications in these fields range from single-cell analysis to cell culturing in monolayers and 3D [6], as well as to quantification of small molecules, peptides and proteins by different sensing methods, the most important of which are optical techniques (especially fluorescence) [7, 8], electrochemical sensing [9, 10] and mass spectrometry [11]. Electrical sensing of cell (monolayer) viability by impedance spectroscopy [12] is also steadily gaining more and more attention with respect to monitoring of cell viability.

Although several materials have been introduced and a range of microfabrication techniques developed for the aforementioned applications, certain challenges persist in terms of the microfabrication or application perspectives. Optical detection sensitivity can also benefit from implementation of thin-film based metals as micromirrors [8], which requires not only metallization, but also customized microfabrication methods enabling polymer bonding over metal elements and step coverage over the edges and sidewalls of the microstructures. Ideally, the mirror elemenets should be concave to maximize the beam reflection (focusing) compared with planar micromirrors. Besides mirror elements, rounded microstructures would benefit the development of microfluidic 3D cell culture models, such as

on-chip culturing of cell spheroids in U-shaped microwells. However, the fabrication of round cross-section microstructures often necessitates multistep fabrication processes, which is somewhat time-consuming and thus impractical. New biocompatible materials feasible for straightforward, preferably single-step, patterning of rounded microstructures are thus needed to bridge these gaps. Overall, the possibility to use both optical and electrical sensing in cell and small molecule monitoring substantially increases the amount of information that can be extracted from a Bio-MEMS. Namely, not all small molecules can be optically detected, and thus electrochemical detection provides a more universal, yet low-cost supplementary tool, which typically preserves its high sensitivity upon miniaturization of electrode elements. In cell culturing, electrical (impedance) sensing facilitates online monitoring of the cull culture and thus provides a valuable complementary tool to optical, typically end-point, detection. Implementing metal-sensing elements (mirrors or electrodes) to biocompatible substrates thus poses a great promise to Bio-MEMS, which has only partially been resolved in terms of the associated technical challenges in selected in vitro applications so far [13, 14, 15, 16].

2 REVIEW OF THE LITERATURE

This chapter provides a brief overview of the common microfabrication materials and techniques used in Bio-MEMS development (2.1) and gives an introduction to metallization of microstructures (2.2), cell and small-molecule monitoring (2.3) and the possibilities to regulate cell adhesion by microfabrication means (2.4). Finally, the feasibility of ORMOCERs to Bio-MEMS fabrication is discussed (2.5).

2.1 Microfacbrication materials and techniques

2.1.1 Wafer-scale microfabrication

The applicable microfabrication materials must fulfill certain basic requirements. For bioanalytical applications, biocompatibility in term of non-toxicity of the material in vitro is the most crucial factor. From a more general perspective, the mechanical and chemical stability of the material also play important roles as during the fabrication process, multistep thermal, mechanical and chemical procedures are taking place. Another key requirement is the possibility for controlled surface modification, which has a direct impact on both cell as well as metal adhesion with a view to implementation of electrical and optical-sensing elements. Finally, optical and dielectric properties of the material also feature prominently in terms of sensing possibilities [17].

Silicon and glass have a long history within the miniaturization industry. Both materials offer excellent thermal, mechanical and chemical stabilities [17]. Glass has robust dielectric properties and optical transparency, whereas silicon acts as a semiconductor. Silicon and glass microfabrication concepts are based on selective etching of silicon/glass wafers, which is facilitated by photolithographic patterning of the photoresist applied on top of the wafer. Photoresist is employed for shielding desired parts of silicon/glass so that other components can be selectively etched. Alternatively, some photoresists (such as SU-8) can also be utilized for fabrication of microstructures on them so that the silicon/glass wafers only act as carrier plates. Overall, well-established microfabrication protocols are one of the main reasons for the wide use of silicon and glass in various applications, whereas the relatively high cost and complex processing limit their use. Sealing of glass and silicon microstructures is achieved by anodic bonding, but requires high temperatures (300-400 °C) and high voltages (300-500 V). As result of these requirements, the focus on Bio-MEMS fabrication has shifted to polymers,

which are low cost, easy to prototype and sometimes readily bio- and cell-compatible [18].

Optical masks are categorized into bright- and dark-field masks. In the case of bright-field mask, UV light is allowed through the whole mask area, but not through the printed, non-transparent microscale patterns. In contrast, with a dark-field mask, UV light is blocked by the whole mask area, but UV light is permitted through the nonprinted areas (Fig. 1) [19].

Photoresists, in turn, can be categorized into positive and negative resists. Negative resists cross-link upon UV exposure, whereas positive resists become water-soluble. Positive photoresists, such as those of the AZ family, have been used widely in the semiconductor field owing to their high feature resolution, for example, for protection of thin-film metal against etching processes. However, in general, positive photoresists cannot support thick layers like negative photoresists, which is why negative photoresists are more commonly employed in fabrication of microstructures by direct photolithography. The performance of a dark-field mask with a positive photoresist is similar to a bright-field mask with negative photoresist (Fig. 1) [19].

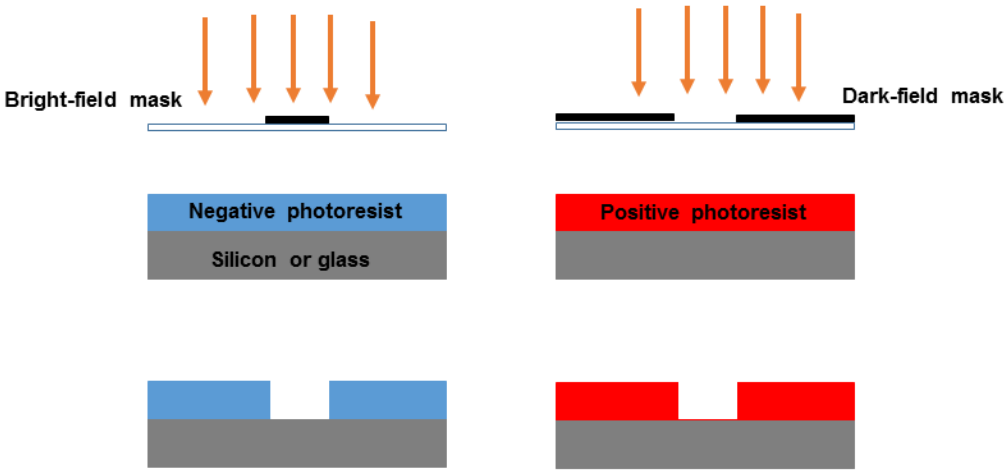

Figure 1. Illustration and and comparison of bright-field mask with positive photoresist and dark-field mask with negative photoresist under UV photolithography. Illustration drawn by the author. © Ashkan Bonabi, 2019

SU-8 is a negative photoresist that became common because of well-established fabrication procedures that facilitated fabrication of various thicknesses and high-aspect ratio microstructures for the purposes of both master mold and active chip elements. Strong optical clarity and transparency within the visible range, robust mechanical and thermal stability, favorable dielectric properties (insulating properties for high-voltage applications) and biocompatibility [20, 21, 22] are the main reasons for popularity of SU-8. However, SU-8 also has several downsides. It is difficult to remove from carrier wafers [23] but can be removed by etching silicon oxide in HF. Further,

it requires long thermal processing times, such as soft baking and post-exposure baking, to minimize film stresses, especially in thick film SU-8 [24]. Nevertheless, SU-8 has been extensively utilized for microstructure fabrication, most often as a master mold for polydimethylsiloxane (PDMS) soft lithography [25].

Owing to its simple and low-cost prototyping, resulting in flexible structures with high optical transparency, PDMS became common in many microfluidic applications. In addition, the high oxygen permeability of PDMS is a crucial advantage for microfluidic cell-culturing applications. However, PDMS easily absorbs small hydrophobic molecules, which may lead to biased results in cellular and biomolecular experiments [26]. Permeability to water vapour [27], which can reduce water volume over time, and polymer aging [28], which changes surface wettability properties, are also common drawbacks of PDMS.

With all development that has taken place so far, still needed is an alternative polymer that supports transparency, biocompatibility and mechanical stability with easy microfabrication techniques.

2.1.2 Implementation of round cross-section shape

Parabolic microstructures (rounded cross-section shape) are beneficial to many applications. For example, rounded cross-sectional profile microchannels (Fig. 2A) allow modulation of fluid flow (flow rate) by adaptation of flexible membranes on rounded cross-sectional profiles (microfluidic valve [29]), which is not possible with rectangular microchannels. In addition, rounded cross-sectional shaped microwells (Fig. 2 B) permit cell aggregation after cell seeding to form cell spheroids better, than cylindrical microwells (Fig. 2C) by enabling formation of compact cell aggregates even from small initial cell populations [30]. In cylindrical microwells, such small initial cell populations would only spread around microwell corners and form nonsymmetrical cell aggregates [31] (Fig. 2C). The symmetric shape of the spheroids formed in round microwells is however crucial to analyzing the growth rate and toxic effects on the basis of spheroid diameter.

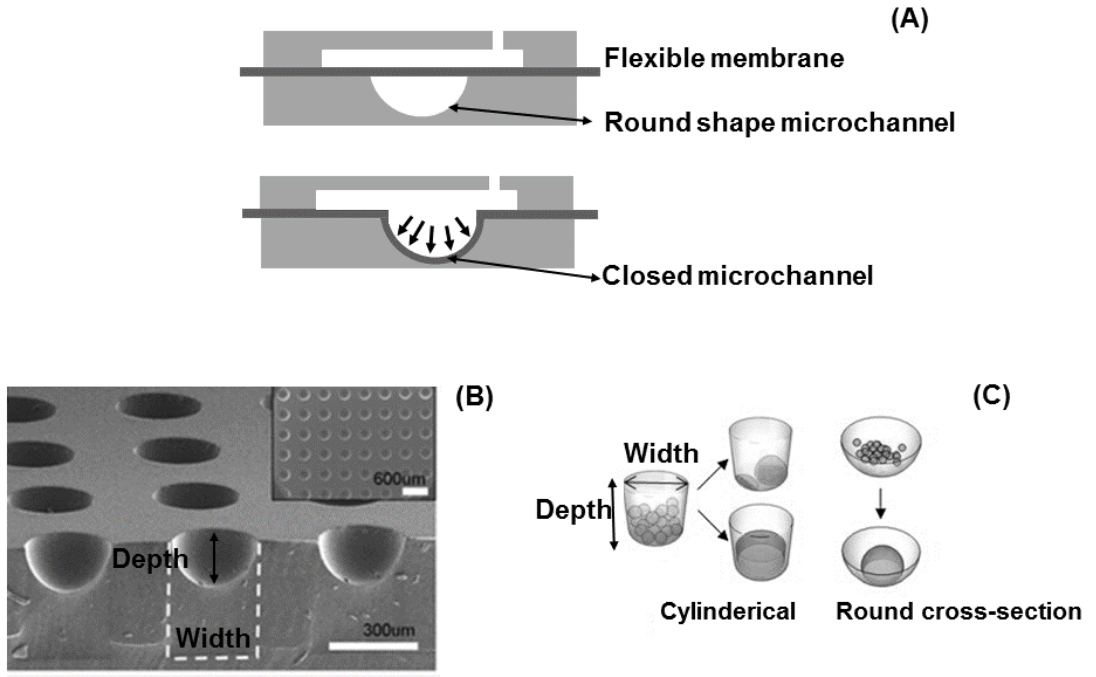

Figure 2. Round cross-sectional microstructures and applications. A) Round cross-section microchannel valve that enables controlling fluid flow with flexible membrane. B) Round cross-sectional microwells. C) Merging small cells to spheroid in round cross-sectional microwells, shaping the cylindrical form of initial cells within cylindrical microwells. A, B and C were adapted from references [29], [32] and [31] with permission of the Institute of Physic Publishing (IOP), Advance Materials and Elsevier, respectively.

Generally, most polymer microfabrication processes result in microstructures approximating near vertical-walled microstructures, the same as with plasma etching of silicon or glass [17]. Although the resulting cross-section profiles of polymer devices are generally more versatile (including tilted sidewalls) than those of silicon and glass. In contrast, isotropic wet etching of glass results in round cross-sectional profiles and anisotropic wet etching of silicon provides tilted sidewalls [17]. Lithography of SU-8 generally leads to vertical walls however; tilted sidewalls can be achieved via UV overexposure of SU-8 [33]. Further, SU-8 has been used as a master mold in PDMS soft lithography for producing various form of sidewalls. Despite the rapid development of microfabrication techniques and materials, there are still many challenges in the fabrication of round cross-sectional microstructures. Traditionally, silicon and glass isotropic etching have been used for direct patterning of them [34, 35]. Yet, controlling the shape and size independently is very challenging owing to their interconnectedness (between depth and feature size). Therefore, soft lithography became more prominent through its facilitating fabrication of convex structures, which could be replicated into a concave shape, although this often requires fabrication of a master mold, a multistep and time-consuming process [36, 37]. Photoresist

reflows have also been used for producing round, cross-sectional profile microstructures. The reflow process yields convex droplet-like structures that can be converted to concave (round cross-section) structures via soft lithography [38, 39, 40]. However, as the reflow process almost exclusively results in semicircular convex patterns, it provides only limited means to control the shape and size (aspect ratio) of the concave structures. In addition, the methods based on photoresist reflow are multistep processes, which increases the complexity, and the time required for microfabrication.

Surface tension and capillary forces have also been applied for shaping and regulating round cross-sectionally shaped microwells. Cylindrical microwells (rectangular cross-section) were previously fabricated and covered with PDMS prepolymer (Fig. 3A), and later scraped out with a glass slide (Fig. 3B) to form a concave meniscus in microwells [41] (Fig. 3C) by thermal curing.

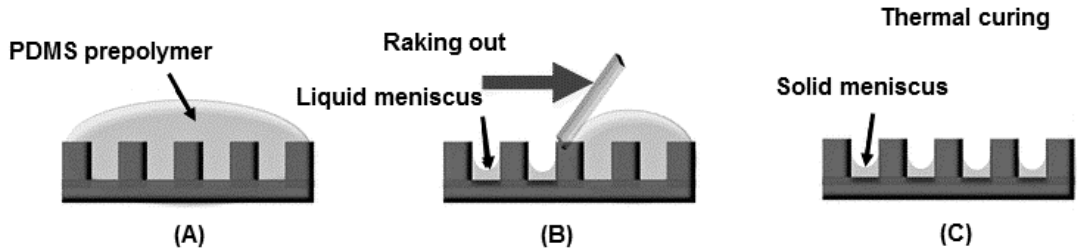

Figure 3. Fabrication of round cross-sectional microstructures utilising a meniscus. A) The PDMS prepolymer on the cylindrical microwell (rectangular cross-section) arrays. B) Raked out PDMS using a flat plate. C) After thermal curing, solid meniscus forming. Adapted from reference [41] with permission of the Royal Society of Chemistry.

In another work, after fabricating cylindrical or square microwells, they were filled with a mixture of PLGA and rhodamine B. Next, evaporation of the solvent resulted in round cross-sectionally shaped polymer microrafts inside the microwells [42]. Gas expansion based on temperature differences was leveraged for fabrication of round cross-sectionally shaped microwells. In another study, microsquare holes (95 (width) × 95 (length) × 350 (height) μm) were also patterned with soft lithography, and then PDMS was poured to cover the holes while the air was trapped. While curing at high temperature, the air expands to form spherical cavities in the PDMS [43]. High sensitivity to surface properties and difficulties in regulating the curvature and depth of wells are drawbacks of using surface-tension and capillary force methods.

Ink-jet printing and 3D printing techniques became attractive owing to direct-writing and maskless process [44] . For ink-jet printing, liquid droplets were utilized for fabrication of round, cross-sectional microstructures, requiring many steps (surface treatment) for preparation of substrate [45]. However, feature resolution is limitation for ink-jet (10 to 100 micrometer range) and 3D printing [46, 47]. In addition, roughness and non-uniformity of fabricated surface [48] limits use of 3D-printing optical applications, which require smooth surfaces to minimize optical losses at the interfaces.

Laser writing is a fast and precise direct-writing method for fabrication of round, cross-sectional shapes [49, 50]. However, after applying lasers to silicon and glass, surfaces become rough, which necessitates chemical etching that limits the throughput. In addition, it is a serial processing technique and hence expensive.

2.2 Metallization of microstructures

2.2.1 Metallization requirements for Bio-MEMS

Various types of electrical sensing elements have been integrated in microfluidic systems based on thin-film metal technologies. The performance of electrical sensing elements is strongly dependent on metal properties. Copper has excellent electrical conductivity that makes it a common choice for interconnections within integrated electrical wires [51]. For optical applications, highly reflective metals, such as Al, Ag and Cu have been employed as mirror surfaces [52, 53]. For thermal-sensor applications, silver paint is injected in PDMS as wire to convert electrical energy to thermal energy [54] as a microheater, which has been widely utilized for PCR applications. Gold is known to be bio- and cell compatible [55] and thus is often used in cell impedance measurements.

Other metals, like Pt [56], Ag/AgCl [57] and other conductore like indium tin oxide (ITO) [58] have been employed in electrochemical detection for small molecules. A great advantage of electrochemical techniques is that by miniaturization of the electrode, the signal-to-noise ratio can be increased because the noise decreases more than the signal. Electrochemical detection has also attracted significant interest based on its robust feasibility for fabrication of portable devices [59, 60]. However, frequent calibration [61], electrode-fouling problems [62] and electrode adhesion are challenges of electrochemical systems.

2.2.2 Metallization processes

Two steps are required for integrating metal-sensing elements on top of existing topography: (1) thin-film deposition; and (2) patterning of the deposited metal by etching (or lift-off). Thin-film metal deposition can be categorized into physical or chemical vapour deposition (PVD or CVD, respectively). Both techniques are vacuum-based. In the case of CVD, chemical reactions take place at the substrate surface, which may simultaneously alter surface properties. However, the step coverage of CVD is more conformational than PVD, therefore serving as a preferred choice for complex geometries [17].

PVD techniques include sputtering and evaporation, which are line-of-sight coating processes and particularly suitable for polymer metallization because they require room temperature processes. The sputtering method is a plasma-based process, where argon (Ar) ions become charged and strike the metal target source, therefore causing release of metal atoms, at which point the released metal atoms coat the substrate. Film density is very favorable and impurity is low whereas deposition rates are generally slow with the substrate potentially unnecessarily heating up. In sputtering method, the kinetic energy of atoms is higher due to short distance between target source and substarte, so they can diffuse on the surface across longer distances, rendering the sputtering method providing more conformational coverage.

The evaporation method makes use of thermal energy to heat up the source target to evaporate metal atoms, which results in coating of the substrate with thin-film metal. High deposition rates and good uniformity over planar surfaces are the main advantages, whereas poor conformality on nonplanar surfaces and low-density films limit the use of this technique. In evaporation method, depositions grow in island mode because of the thermal setup and long distance between the substrate and target, leading to rougher and more porous films.

There are two procedures for patterning of metal elements, namely the lift-off and etching processes. With the lift-off process, coating and patterning the photoresist must be carried out before deposition of metal. The lift-off process is one that least alters surface properties [17]. However, it is a relatively lengthy process and it is difficult to fabricate sharp edges of electrodes with this method, due to non-uniform residual metal around edge of patterend areas, which is a major downside for many applications that require sharp-edge electrodes. Yet, etching processes commencing after metal deposition require coating and patterning a photoresist layer on top of the thin-film metal for patterning the metal layer. Subsequently, wet- or dry-etching techniques are applied for patterning metal-sensing elements.

In cases of wet etching, the metal layer is removed by immersing liquid etchant. Wet-etching processes are based on chemical reactions between liquid etchants and metal film. They are easy and cost-effective processes, but become difficult in terms of feature sizes smaller than 1 μm and controlling for undercut (Fig. 4).

With dry (plasma)-etching, the metal layer is volatilized by utilizing plasma instead of liquid etchant, which results in better control of feature resolution in comparison to wet etching. Through plasma etching, it is possible to define feature sizes less than 100 nm. However, plasma etching is an expensive and complex process because of the need for a vacuum system [17]. In conclusion, for higher resolution control, plasma etching can be a reliable candidate, whereas wet etching is a readily performable and low-cost process. Moreover,

wet etching is a double-sided process whereas plasma etchng is a single-sided process (Fig. 4).

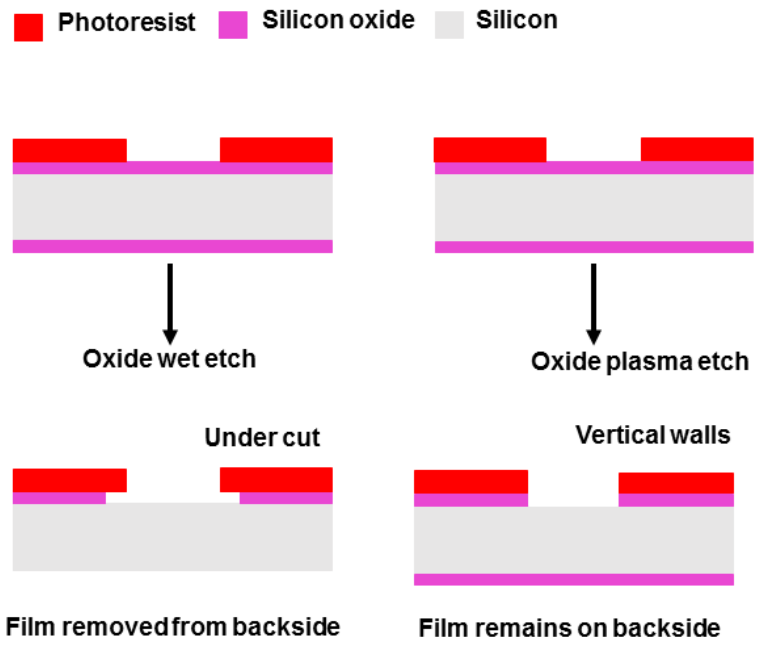

Figure 4. Illustration and comparison between wet etching and dry etching of silicon oxide on silicon substrate. Illustration drawn by the author. © Ashkan Bonabi, 2019

2.2.3 Quality of substrate metallization

Thin-film metal deposition and patterning quality are strongly dependent on substrate properties. To accomplish consistent implementation of metal elements, substrate must be compatible with various metallization techniques. Adhesion, step coverage and stability of the thin-film metal on the substrate are crucial for proper performance. Adhesion is the most important issue because huge amounts of stress are applied onto the substrate and metal during multistep microfabrication procedures. Surface smoothness and electrical insulation between electrodes are other factors that reduce electrical noise. Various microstructures have different topographic and aspect ratios. Thus, connectivity of thin-film electrodes patterned over microstructures require very robust step coverage [63]. Generally, rounded corners and tapered sidewalls offer better step coverage compared to sharp vertical topographies. Figure 5 illustrates the impact of tapered walls and round corners on the success of metal deposition [63]. As can be seen, by increasing the angle of the walls (Fig. 5 A, B, C), a metal layer covers the wall much better (Fig. 5D). In addition, it is recognized that metal coverage is disconnected at sharp edges (Fig. 5E) and by elevating the radius of the corners (Fig. 5F and G), metal deposition is smoother.

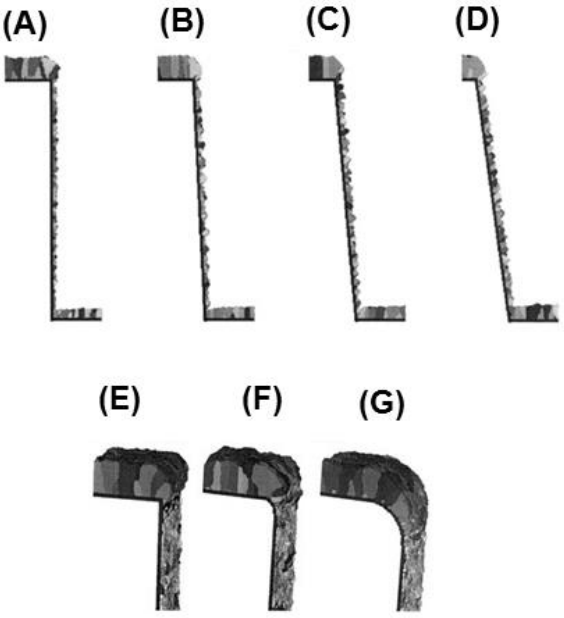

Figure 5. Cross-sectional views of deposition into trenches with differing sidewall angles. A) 90°. B) 87.5°. C) 85°. D) 82.58°. Simulation of metal deposition over corners with E) sharp corner, F) rounded corner with radius 0.005 μm and G) rounded corner with radius 0.07 μm. Reprinted from reference [63] with permission from Elsevier.

Generally speaking, glass has been used as the primary material for hosting of electrical elements [64, 65]. Silicon has also been commonly employed as the substrate material because of the many developed silicon-based techniques transferred from MEMS to Bio-MEMS. As a consequence of silicon's semiconductive property, it needs insulation with other thin films, such as silicon dioxide (SiO2) [66] or silicon nitride (Si3Ni4).

Polymers are typically challenging to metallize owing to thermal tolerance, thermal expansion and adhesion issues. Further, metallization of PDMS for fabrication of crack-free electrodes is challenging because of the soft and porous surface of PDMS [67, 68]. Another main issue is adhesion of thin-film metal on the relative rough PDMS surface [69, 70]. Thus, deposition methods, such as electrodeless plating, that provide noteworthy coverage of rough surfaces by thicker layers of metals, such as copper, were considered as a solution [71]. Based on the porous and flexible properties of PDMS, deposited metal can crack, a significant limitation. Meanwhile, the SU-8 surface has exhibited strong compatibilities for deposition of thin-film metal via sputtering, evaporation or electroplating techniques [72, 73, 74]. However, crack formation on top of the SU-8 surface because residual film stress reduces the quality of deposition and patterning of the uniform metal layer [75, 76].
Although there are several metallization approaches available, each with their inherent advantgaes and disadvantages, overall, polymer metallization requires material-specific optimization.

2.3 Cell and small-molecule monitoring

This section is focused on common cell monitoring needs and covers variety of technologies that have been applied for cell and small-molecule monitoring and detection. Generally, cell-monitoring systems can be categorized into single-cell analysis and monitoring of cell growth. Cell monitoring usually requires structural elements that enable capturing of (single) cells or cell-adhesive surfaces to allow on-chip cell culturing. Furthermore, as reviewed before, material must feasible for integration of optical and/or electrical-sensing elements, and should minimally interfere with the detection of cells and small molecules. Impedance monitoring for cell monolayers is relatively is easy to implement, whereas monitoring of 3D cell cultures by impedance requires more complicated setups. Bright-field optical detection therefore remains the most used non-invasive approach for cell spheroid monitoring as well as for single cells. In addition, on-chip monitoring systems enable analyzing the parameters governing the metabolic processes of cells (e.g., oxygen level of pH) based on electrochemical responses.

2.3.1 Impedance-based monitoring

Impedance spectroscopy is a non-invasive cell-monitoring technique that has gained increasing interest recently owing to its feasibility for integration with microfluidic cell culture platforms [77]. Impedance methods have been mostly utilized for monitoring and detection of cell monolayer (2D) cultures. By applying complex ratios of voltage and current, electrodes can measure impedance of cells, facilitating quantitative cell characterization, during growth and proliferation periods [78]. In cellular studies, the cell index (CI) has often been applied instead of cell impedance. To determine CI, first, cells are seeded into the channel. Upon cell adhesion, impedance starts to increase sharply, whereas during cell proliferation, the rise of impedance slows down. It can take a very long time until the cells reach confluence and the CI value plateaus, which means impedance magnitude from electrodes that access to cell culturing media, are not changing, because all electrode areas are covered by aggregate. When cell starts detaching or dying, CI starts to decrease. Figure 6, illustrates general example of 2D cell culturing and performance of impedance electrode.

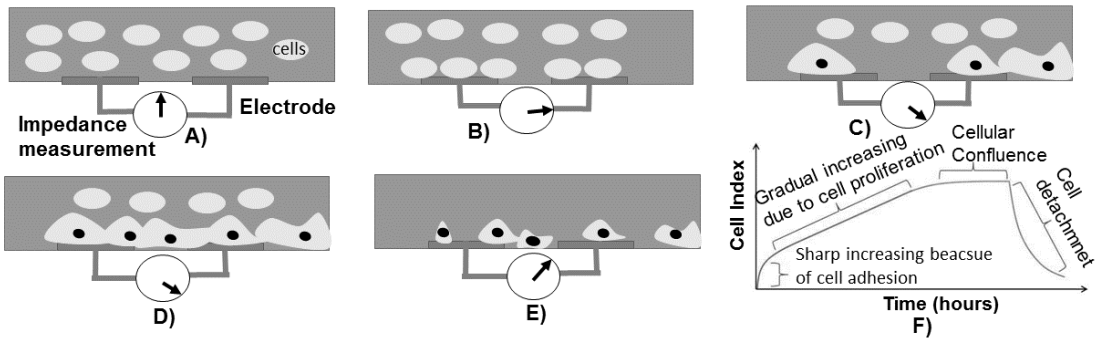

Figure 6. Impedance trace of 2D cell culturing on electrode. A) Releasing cells inside of fluidic channel. B) Settling of cells on electrode causing large jump in impedance. C) During proliferation, impedance increases gradually. D) Based on cellular confluence, impedance does not change. E) By detaching or dying cells, impedance starts to decrease. F) Graph of impedance measurements (Cell Index) in terms of variation vs. time. Illustration drawn by the author. © Ashkan Bonabi, 2019.

Impedance measurement of cells has been described in various mathematical models. The theory behind impedance sensing is Ohm's law. By applying frequency-based AC voltage signal, U (ω), as an excitation source to electrodes, electrical current response, I (ω), is quantifiable. By dividing voltage over current, complex impedance, Z (ω), is defined [79].

Herein, we summarize various models for the Electrode Cell-Impedance Sensing (ECIS) method. One of those models is based on a single-shell model – a cell will block the current on the electrode [80]. However, other models illustrate the character of merging cells according to an electric circuit model. The attached cell on the electrodes is considered capacitance [81], and the resistance-capacitance complex [82] or constant phase element [83], is part of different circuit model. It is reported that the optimal region of frequency for impedance measurement is between 100 Hz and 100 KHz, an impedance magnitude without cells is less than with cells [84]. There is impedance in the electrode-medium interface and medium, which is known as base impedance (Z0) or background impedance. By subtracting whole-system impedance (Z) from background impedance (Z-Z0), cell impedance can be arrived at [85].

Electric impedance spectroscopy (EIS) [86] enables measuring impedance of suspended cells in culture medium using metal electrodes. In addition, it is possible to also measure cell impedance when they adhere on electrodes [80]. However, by increasing the frequency of chemical reactions in the medium, the interpretation of electrical responses can be complex [87]. By insulating an electrode with polymer, there is the potential to measure just the adhered cell areas [88]. Impedance sensing permits monitoring of single cells [89] and multiple cells [90] for a long time [91]. Therefore, such applications have been expanded to cancer research [92] and drug screening [93].

For measurement of 3D cell impedance, especially that of a spheroid nature, cells should not adhere to electrodes that prevent topographical changes in spheroid character. For spheroid impedance measurements, two factors are crucial. The first is a 3D scaffold for growing symmetrical spheroid.

The second is electrodes for direct contact with spheroid that usually integrate into scaffold walls or stand vertically inside of a scaffold.

For impedance monitoring of 3D cells, such as those of a spheroid nature, multiple electrodes are required for sensing within each cavity for contact with cells in the x and y or z directions [94, 95] (Fig. 7 A). Usually, scaffolds used for culturing spheroids are in array form, so it is necessary to implement a number of electrode into each scaffold, thereby causing a great amount of wiring in a scaffold array. Providing strong step coverage for electrodes on sidewalls and the edges of scaffolds is also an issue and requires tapered sidewalls and round-shaped edges (Fig. 7B). An alternative way to measure non-adherent cell impedance is using electrodes for suspended cells placed vertically inside a scaffold. In recent work, electrodes, integrated on the ceiling of a substrate, which drops hanging and spheroid, were suspended [96] (Fig. 7C). External sensors (needle-type) were also considered [97, 16] as a non-adherent electrode to cells (Fig. 7D) in a solid matrix. However, because of the low number of cells, the concentrations in scaffolds would be small, hence highly sensitive technologies are needed.

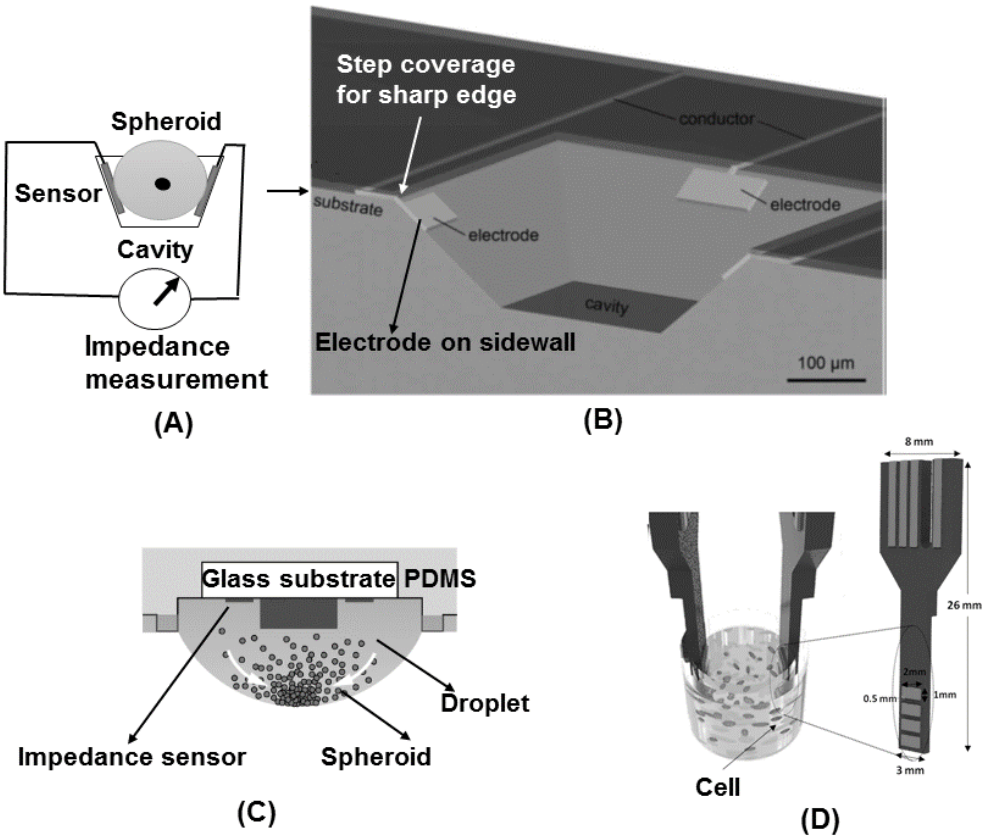

Figure 7. Electrochemical sensor for 3D cell culture model. A) Multiple sensors on sidewalls for monitoring impedance of spheroid in cavity. B) Electrone micrographs of multiple sensors in cavity for spheroid. C) Suspended spheroid in droplet. Sensor implemented on ceiling of droplet to prevent adherence between cell and electrode. D) External sensor based on capacitance model. Figure A drawn by the author. © Ashkan Bonabi, 2019. B, C and D adapted from references [94] , [96] and [16] with permission of the Royal Society of Chemistry, American Chemical Society and Elsevier, respectively.

2.3.2 Single-cell detection

The ability to monitor and detect single cells, permits characterizing electrical and mechanical properties of cells. Flow cytometry is an impedance-based technique for analysis of single cells in a flow system incorporating two electrodes located in front of each other alongside a microfluidic channel. After applying voltage, fluid medium between two electrodes becomes the electrical current path, which is called the sensing zone. By passing a single cell through this zone, small changes take place in impedance that counter electrodes and can detect variations in impedance [98]. This technique is being used for both counting single cells and measuring cell size and membrane properties. It is, however, not feasible for characterization of intercellular activities [99]. For example, Ag/AgCl wires inserted into a fluidic channel filled with highly conductive electrolyte solution [100], demonstrates a linear relationship between the amplitude of impedance peaks and volume of size-calibrated particles.

Another method for single-cell detection is capturing single cells with microfluidic system and analyzing them with optical monitoring. With this method, microdroplets were generated and encapsulated as a single cell. Next, the encapsulated single cell was conducted via arrays of the 'T-junction" and trapped by the main–bypass construction on a polydimethylsiloxane–glass chip. At this stage, evaluation and monitoring of cells was performed by optical instrumentation [101]. This system is appealing owing to its flexibilities and easy analysis. By applying bright-field or fluorescence dye [102, 103] and implementing optical elements [8], such as concave micromirrors, optical detection can improve significantly.

2.3.3 Integration of optical microelements

Optical elements (micromirrors, microlenses and waveguides) enable redirection and transferring of light from source to detector. Microlenses have been used in various shapes [104] and array form [105, 106, 107] to concentrate (Fig 8A, B) or diffract light beams (Fig. 8C, D). The main challenges related to the implementation of microlens arrays include limited control over the lens curvature and alignment. Based on the simplicity of fabrication, planar [108] (Fig. 8E) and tilted [109, 110] mirrors (Fig. 8F) are more common than concave mirrors. However, signal improvement achieved by concave mirrors is much greater because of focusing reflected light beams, while planar mirrors only facilitate back reflection of the light beam. In addition, concave micromirrors were also employed for yeast cell trapping under halogen lamp lights, by using Köhler Illumination [111].

Optical detection has been heavily applied to monolayer (2D) and 3D cell culturing. Optical detection of cells can be divided into labeled and label-free techniques. Fluorescence dyes have been used as indicators for increasing efficiency of optical monitoring. Although they constitute an invasive method

that can be harmful for cells [112], it is one of the most commonly used methods for end-point monitoring of cell monolayers (2D) and 3D cell models. For example, monitoring spheroid growth as a function of time and/or of toxicant concentration can be carried out by bright-field optical monitoring.

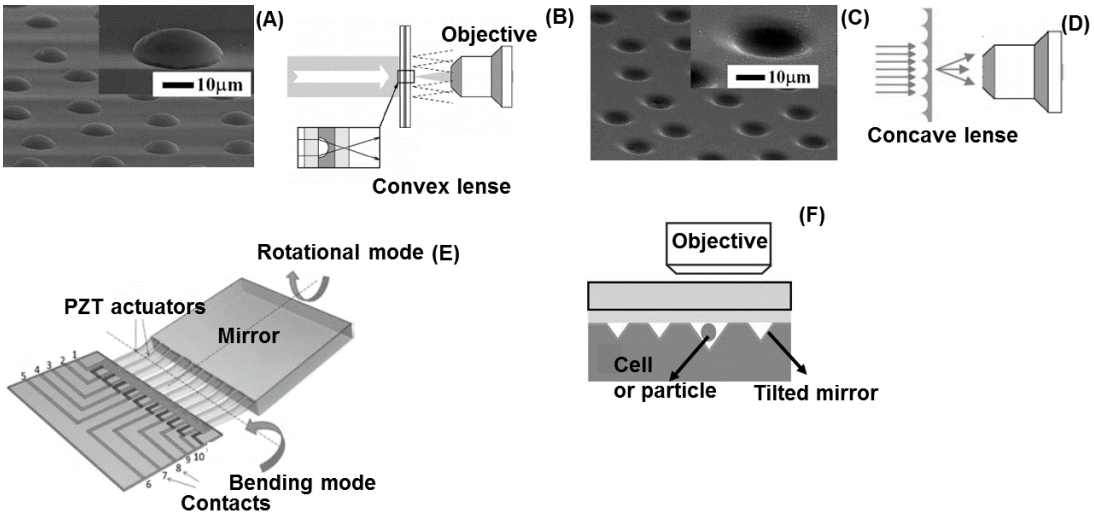

Figure 8. Schematic view of optical microelement. (A) Convex lens. (B) Performance of convex lens. (C) Convcave lens. (D) Performance of concave lens. (E) Planar mirror able to tilt. (F) Tilted mirror. A, B, C, D, E and F adapted from references [107], [113], [107] , [114], [108] and [110] with permission of Wiley Online Library, American Institute of Physics, Elsevier and the Royal Society of Chemistry, respectively.

2.3.4 Electrochemical monitoring

Electrochemical monitoring is generally label-free. However, it strongly depends on compounds that are electrochemically active. Amperometric and potentiometric methods are two most frequently employed approaches to assessing extracellular conditions and/or components. With amperometric methods, redox reactions result in flowing current in electrodes. For example, amperometric oxygen sensors are based on oxygen reduction within inert working electrodes, such as those constituted by Pt [115]. When oxygen reduction occurs, the cathode is polarized at a certain level and current is produced proportional to the oxygen concentration. Amperometric sensors with Pt, Pd and Au electrodes were used for monitoring of oxygen during monolayer (2D) cell culturing. In one study, a Pt amperometric sensor was integrated into a PDMS scaffold ceiling for measuring excreted glucose in a microfluidic spheroid culture [116]. Potentiometric sensors measure electrical potential between electrodes when oxygen appears or pH levels change. However, iridium oxide [117] was utilised for oxygen control and a ruthenium dioxide electrode was applied for pH monitoring of momolayer (2D) tumor hypoxia [118].

2.4 Regulation of cell adhesion

Naturally, cells adhere to the surface via membrane proteins. The amount of protein interactions within culture dishes depend on the wettability of the surface [119]. On the other hand, to culture cells in a 3D model, the surface should be cell-repellent. In general, polymer such as Ormocomp surfaces is inherent cell-adherent, whereas Poly(ethylene oxide) film is more anti-adherent [120] which by cell patterning techniques surface properties can be favourable for adhesion of cells. However, the material behavior regarding cell adherence strongly depends on type of cells.

One of the most commonly employed materials for making surface cells repellent is polyethyleneglycol (PEG), a non-fouling biocompatible polyether compound used for passivation of a polymer-based cell culture surface [121] by modifying the interaction of proteins with the surface. PEG patterning can be implemented by micro contact patterning (µCP). With this procedure, an elastomeric stamp was fabricated and covered by extracellular matrix (ECM). ECM is comprised of extracellular macromolecules, such as collagen or glycoproteins. Thereafter, the elastomeric stamp with ECM was microprinted on glass substrate. This was followed by PEG being covered on top of the glass substrate, thus non-stamp areas were patterned by PEG [122]. PEG can also be UV patternable [123].

Plasma-phase polymerization is coat surfacing to achieve specific properties such as hydrophobic properties. The coating is a thin layer of organic and inorganic materials with a high degree of cross-linking. Depending on the application, plasma polymers enable coating with a hydrophilic or hydrophobic layer on the surface. The deposited thin films can be patterned by photolithography and etching. With plasma polymerization methods, the aid of radio frequency (RF in MHz) facilitates plasma being generated in the plasma chamber. The monomer to be polymerized is injected from the monomer tube into the plasma chamber under vacuum conditions. The electronic impact of plasma causes fragmentation and excitation of the monomer, thereby leading to reactions with each other as well as the substrate to be coated. Therefore, a series of reaction steps occur to polymerize the monomers as well as bonding them to every surface on the object, from the nanometre to micrometre scale, for various applications [124]. Compared to other surface-treatment technologies, plasma coating offers a number of advantages. Plasma polymer coatings are extremely dense with excellent corrosion resistance. Uniform 3D coating of complex components is also possible. Moreover, it is a simple and efficient method but expensive and sensitive to metal. However, it is still the best option for complex microstructures.

Porous surfaces have also been used for surface functionalization [125]. There are various methods for creating porous surfaces depending on the type

of material. As polymer-based applications are accumulating each day, pores have been studied on polymers, such as SU-8 [126], PMMA [127], polyimide (PI) [128] and organic-inorganic polymers [129]. With respect to SU-8, the pore formation is based on incomplete soft bake and sizes are from 6 to 10 nm. For PMMA and PI, pore formation requires ion-irradiation techniques. For organic-inorganic polymers, oxygen-plasma etching is essential. It has also been stipulated that in the case of organic-inorganic polymers, by applying oxygen plasma for longer periods of time, surfaces can change to hydrophobic [130].

2.5 Organically Modified Ceramics

Organically Modified Ceramics (ORMOCER®s) are a group of hybrid polymers originally developed by Fraunhofer ISC and commercially available via, e.g., Microresist Inc. ORMOCERs are composed of a silicon-oxygen backbone cross-linked with organic side chains [131] are composed of a silicon-oxygen backbone cross-linked with organic side chains. ORMOCERs' bulk properties are a combination of those of silicone, organic polymers and ceramics as illustrated in Figure 9. In addition, ORMOCERs feature high optical clarity and transparency in visible and near-UV ranges.

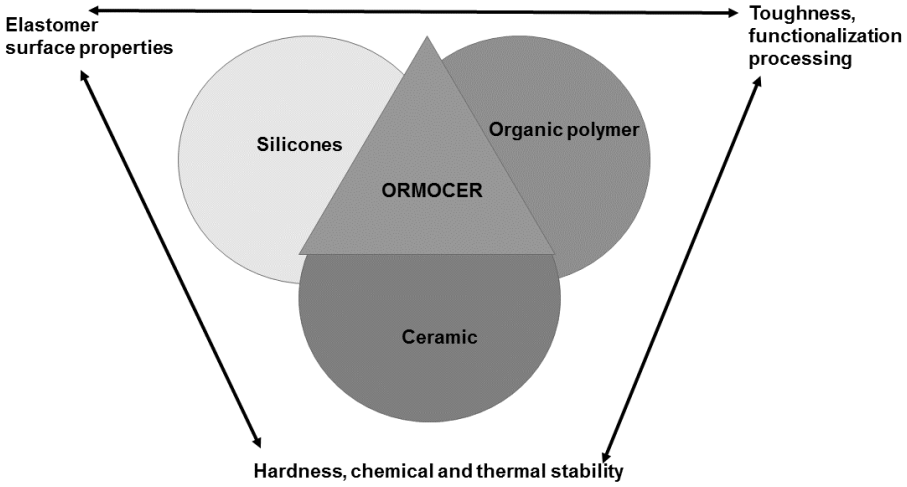

Figure 9. Illustration of Organically Modified Ceramics (ORMOCERs) relationship to silicones, organic polymers, glasses and ceramics properties. Adapted from reference [131] with permission from Elsevier.

From the microfabrication perspective, ORMOCERs are negative photoresists that foster fast, simple and low-cost patterning by UV lithography (Fig. 1) or UV embossing (Fig. 10) [132, 133]. Rapid cross-linking properties have also seen the use of ORMOCERs in fabrication of 3D micro- and nanostructures via multiphoton absorption. Direct laser-writing methods

(femtosecond laser-induced polymerization) [134] and two-photon polymerization techniques [135] have also been applied to fabricate 3D solid-matrix (scaffold) microstructures out of ORMOCERs for cell culturing. Not only do ORMOCERs allow fabrication of microfluidic structures, but also controlled porosification by plasma [129], which can be beneficial for various applications. Metallization of ORMOCERs for large-area patterning has been demonstrated by Ti, Al, Au, Ni and Cu [136], but generally speaking, ORMOCERs have been primarily utilised without further metallization in optical or biomedical applications [137, 135].

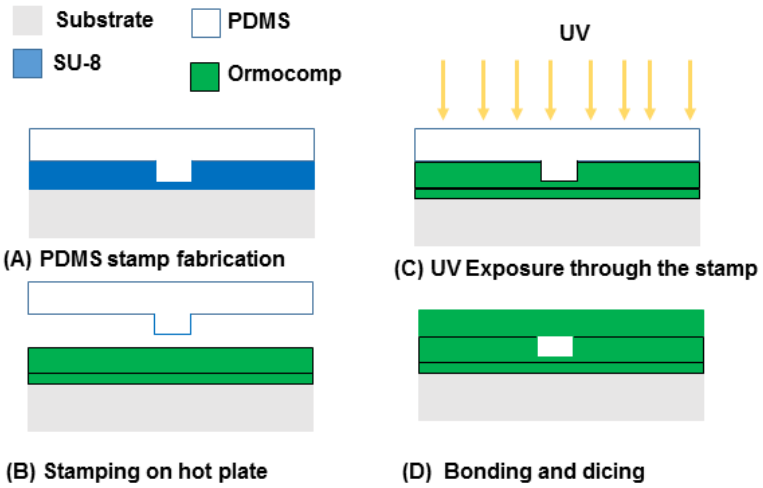

Figure 10. UV embossing of Ormocomp. (A) Stamp fabrication. (B) Stamping of Ormocomp. (C) UV exposure of Ormocomp through the PDMS stamp. (D) Bonding of the Ormocomp chips. Adapted from reference [11] with permission of Elsevier.

The robust biocompatibility together with the possibility for UV curing of hard microstructures has encouraged the use of ORMOCERs primarily in dental applications [138]. The inherent biocompatibility is, though, also attractive for microfluidic cell culturing. In contrast to glass, ORMOCERs support cell adhesion even without additional functionalization [139]. ORMOCERs are also resistant to protein fouling, which has allowed the use of native (uncoated) ORMOCER microchannels, e.g., in the separation of intact proteins by microchip capillary zone electrophoresis [11]. Besides biocompatibility, ORMOCERs possess high optical transparency down to the UV range [140]. Strong dielectric properties (3.2 in10 kHz) and high refractive index (1.44-1.59 at 635 nm) mean there can be attractiveness for radio frequency-based applications [136], optical interconnection or opto-electronic devices [137] and optical elements, such as lenses [141] (Fig. 11). Overall, ORMOCER has shown potential as a material for Bio-MEMS applications. However, integration of additional optical or electrical-sensing elements with ORMOCER microfluidic components still requires further development of the applicable microfabrication and metallization techniques.

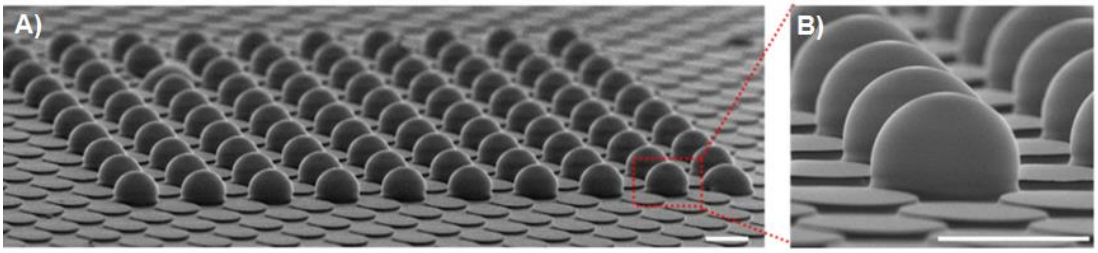

Figure 11. Electrone micrographs of an inkjet-printed and UV-cured Ormocomp microlens array (MLA) on PDMS platforms with lenses of identical curvatures: A) Full MLA with B) zoom into a few microlenses. Both scale bars are 100 µm. Adapted from reference [141] with permission from Elsevier.

3 AIMS OF THE STUDY

The overall aim of this thesis was to develop microfabrication methods for ORMOCERs with a view of optical and electrical sensing of cells and small molecules on Bio-MEMS devices. ORMOCERs were the material of choice based on their inherent bio- and cell compatibility demonstrated in the previous literature. The more detailed goals of the study were:

- To develop novel approaches for fabrication of round cross-sectional microstructures out of ORMOCERs;

- To develop Ormocomp metallization methods by improving adhesion and step coverage for implementing embedded metal-sensing elements;

- To improve the optical-detection sensitivity of small molecules and single cells with the aid of embedded micromirrors;

- To develop electrical-sensing elements for electrochemical detection of small molecules and impedance spectroscopy-based monitoring of cell proliferation; and

- To create new Ormocomp-based microdevices for monolayer (2D)-3D cell culturing on a single microfluidic chip.

4 EXPERIMENTAL

In this chapter, the chemicals and materials (4.1) as well as instrumentation (4.2) made use of in this study are briefly reviewed together with the microchip designs (4.3), microfabrication protocols (4.4), material characterizations methods (4.5) and experimental setups (4.6).

4.1 Chemicals and materials

Chemicals and materials used are listed in Tables 1 and 2.

Table 1. *Chemicals used in this study.*

Reagent/Solvent/Standard	Manufacture/Supplier	Note	Publication
Acetone	Honeywell International, USA	Solvent	I,II,III,IV
Acetaminophen	Sigma-Aldrich	Chemical standard	III
Accutase	Invitrogen, Eugen, OR, USA	Cell dissociation solution	IV
Amino acids	Gibco, Paisley, UK	Cell medium component	IV
AZ 100 remover	Microchemicals, Germany	Resist removal	I, III, IV
AZ 351 B developer	Merck Performance Material, Germany	Az developer	III
AZ 726 MIF	Merck Performance Material	Az developer	III,IV
AZ 826 MIF	AZ Electronic Materials, Germany	Az developer	III,IV
Baby hamster kidney	Sigma-Aldrich	Cell line	I
Boric acid	Riedel-de Haën, Germany	Reagent	I
Calcein AM	Invitrogen, Eugen, OR, USA	Stain	IV
Cell event caspase	Invitrogen, Eugen, OR, USA	Stain	IV
Chromium etchant	Sigma-Aldrich	Cr wet etchant	I,II,III
Dulbecco's Eagle medium	Sigma, USA	Cell medium component	IV
Dimethyl sulfoxide	Sigma-Aldrich	Stain	II
Ethanol	Sigma-Aldrich	Solvent	IV
Ethanesulfonic acid hydrate	Sigma-Aldrich	Reagent	III
Fetal bovine serum	Gibco, Paisley, UK	Cell medium component	IV
Fluorescein sodiume salt	Sigma-Aldrich	Stain	I
Fluorescent protein	Sigma-Aldrich	Reagent	I,II
FxCycle RNase/PI	Invitrogen, Eugene, OR, USA	Staining Solution	IV

Table 1 (Continued)

Reagent/Solvent/Standard	Manufacture/Supplier	Note	Publication
Geltrex	Gibco, Grand Island, NY, USA	Cell medium component	IV
Hoechst 33342	Invitrogen Eugene, OR, USA	Stain	IV
Huh-7 human hepatoma	Sigma, Saint Louis, MO, USA	Cell line	IV
Hydrochloric acid 37%	Honeywell International, USA	Au-Pt wet etchant	III,IV
Hydrogen proxide 30%	Honeywell International, USA	Ag wet etcchant	III
ice-cold ethanol	Sigma-Aldrich	Fixative	IV
L-glutamine	Sigma-Aldrich	Cell medium component	I
Methanol	Sigma-Aldrich	Solvent	II
Milli-Q water	Millipore, Molsheim, France	Solvent	I,II,III,IV
Nitric acid 69%	Honeywell International, USA	Au-Pt wet etchant	III,IV
2-propanole	Sigma-Aldrich	Solvent	I,II,III,IV
Ormo Dev	Microresist Technology	Ormocomp developer	I-IV
Penicillin	Gibco, Paisley, UK	Cell culture component	IV
Phosphoric acid	Honeywell International, USA	Al etchant	II
Propidium iodide	Invitrogen, Eugene, OR, USA	Reagent	IV
Puromycin	Sigma-Aldrich	Reagent	IV
Sodium hydroxide	Riedel-deHaën	Reagent	I-III
Sodium pyruvate	Sigma-Aldrich	Cell culture component	IV
Streptomycin	Gibco, Grand Island, USA	Cell culture component	IV
Su-8 developer Mr-600	Microresist Technology	Su-8 developer	IV
Umbelliferone	Sigma-Aldrich	Reagent	II

Table 2. *Commercially available materials and products used in this study*

Material/product	Manufacture/Supplier	Note	Publication
AZ 4562	Merck Performance, Germany	Photoresist	I,III,IV
AZ 5214E	Merck Performance, Germany	Photoresist	I
Chrome mask	Delta Mask, Enschede, Netherlands	Ormocomp pattering	I-IV
Ormocomp®	Microresist Technology	Fabrication material	I-IV
Sylgard 184	Down Corning, Midland, MI	Fabrication material	I,IV
PDMS curing agent	Down Corning, Midland, MI	Fabrication material	I,IV
Plastic mask	Microlitho, UK	Electrode patterining	I-IV
Pyrex glass	Plan Optik AG	Substrate wafer	I-IV
Silicon <100> wafers	Okmetic, Espoo, Finland	Substrate wafer	IV

4.2 Instrumentation

Commercial instruments employed in the study are listed in Table 3. In addition, custom-made chip holders, vacuum pumps and multimeters were utilized.

Table 3. *Commercially available instruments used in this study*

Instrumentation	Manufacturer/Supplier	Note	Publication
For microfabrication			
Theta Goniometer	Biolin Scientifics, Espoo, Finland	For measuring surface wettability (Contact angle)	III,IV
Dicing saw- DAD3220	Disco, Tokyo, Japan	Dicing samples	I,III,IV
Ellipsometer	Plasmos,Atlanta, USA	Measurement for metal thin-film thickness	III,IV
Evaporator MASA	Mattila, IM-9912	Au,Ag,Ti metallization	I-IV
Hot plate	UniTemp GmbH, Pfaffenhofen, Germany	Baking process of photoresist	I-IV
MA-6 mask aligner SÜS	SÜS MicroTec, Germany	UV lithography tool	I-IV
Oven	Memmert, Germany	Dehydrating Si and glass substrate	I-IV
Profilometer Dektak/XT	Bruker,Billerica, Massachusetts, USA	Measuring depth of microstructures	I-IV
Prime Oven HMDS	Yiled Engineering System ,California, USA	Adhesion promotion	I-IV
RIE Plasmalab 80	Oxford Instruments, UK	Surface modification with oxygen plasma	I-IV
Sputter	OPTON	Gold sputtering	IV
TePla 400	PVA TEPLA Wettenberg, Germany	Oxygen plasma treatment of PDMS	IV
SEM EBL Zeiss Supra 40	Zeiss, Oberkochen, Germany	SEM analysis	I-IV
For cell analysis			
AxioVert A1 FL	Carl Zeiss Oy, Espoo, Finland	Microscope for imaging cells	IV
AxioScope A1 epiFL	Q Imaging,BC, Canada	Fluorescence detection for cells	IV

Table 3 (Continued)

Instrumentation	Manufacturer/Supplier	Note	Publication
For cell analysis			
Accuri flow cytometer	BD, San Jose, USA	Flow cytometer	IV
Cytosmart camera	Cytosmart Lux2, Incyte,Netherland	Online detection	IV
Retiga 4000R CCD	Q Imaging, Surrey, BC, Canada	Camera for analyzing cells	IV
PalmSens4 potentiostat/EIS analyzer	PalmSens BV, Houten, Netherlands	EIS measurement	IV
Harvard Apparatus Pump 11 Elite	Holliston, MA, USA	Syringe pump	IV
Zeiss Axioscope A1 epifluorescence microscope	Zeiss, Espoo, Finland	For analyzing cell and small molecules	I, IV
For optical and electrochemical detection of small molecules			
Argon laser, JDS Uniphase	Cheos Oy, Espoo, Finland	Characterizing micromirror	II
Bipotentiostat	MicruX Technologies, Oviedo, Spain	Electrochemical detection	III
DI Milli-Q water	Millipore, Bedford, USA	Rinsing microchannels	I,II,III
Leica DMIL inverted epifluorescence microscope	Leica DMIL, Nilomark, Espoo, Finland	Fluorescence detection	I,II
Leica microscopes	Leica Nilomark,Espoo,Finland	For small molecule analysis	I
Microfluidic Tool Kit	Micralyne, Edmonton, Canada)	High-voltage power supply	I,II
PicoScope 2203	Pico Technology, St. Neots, UK	AD convertor	I
UV laser	Team Photonics, Cheos Oy, Espoo, Finland	Characterizing micromirror	II

4.3 Microchip designs

In this study, three different Ormocomp microchip designs were developed for optical and electrical sensing of small molecules and cell culturing (Fig. 12). Chip design I incorporated thin-film micromirrors integrated with a classical microchip electrophoresis chip and was applied to optical sensing of small molecules (publication II). The same chip design (design IB, Figure 12) was also used for single cell detection (publication I). Chip design II was developed for microchip electrophoresis with electrochemical detection so as to ensure compatibility with a commercial bipotentiostat (MicruX Technologies, publication III). Chip design III was developed for cell culturing so as to permit parallel cell monolayer and 3D cell spheroid culturing with in situ optical and impedance-monitoring systems (publication IV). All chip designs were drawn with AutoCAD (Micro Lithography Services Ltd., England). The detailed dimensions of the microstructures and metallizations are listed in Table 4.

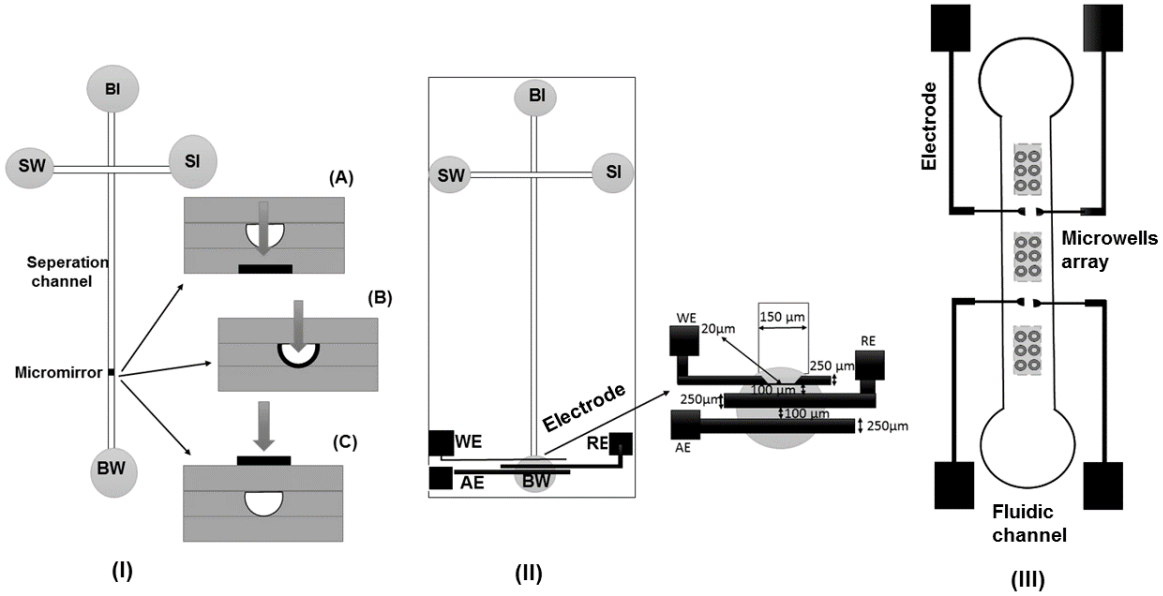

Figure 12. Schematic of microchip designs used in this study. I) Electrophoresis-based micromirror with three types of setups (design A and C: planar mirror on bottom and top, design B: concave micromirror). II) Micrux (MicruX Technologies, Oviedo, Spain) modified electrochemical detection chip. III) Monolayer (2D)-3D cell culturing with ESI electrodes. SI - sample inlet, SW - sample waste, BI - buffer inlet and BW - buffer waste inlet. WE, AE and RE are working, auxiliary and reference electrodes, respectively. Dimensions not to scale. Drawn by the author. © Ashkan Bonabi, 2019.

Table 4. *Channels, wires, electrodes and microwell dimensions for microchip designs used in this study (design numbers indicate the different microchips presented in Figure 12).*

Microchip design	Channel width(μm) × height (μm)×length(cm)	Note	Application
I	50×35×7	Al mirrors dimension: width (2mm)×length (2mm)×thickness (50nm)	Optical improvement of single cell or sensitivity of microfluidic separation system
II	150×35×7	Cr-Pt electrode dimensions width (μm) × thickness (nm)× length (mm) work and auxiliary electrode: 250×220×2 Reference electrode: 20×220×2 Distance between electrode: 100 μm	Electrochemical detection
III	3000×200×3	Ormocomp thickness: 130 μm Microwells diameter (μm): 100, 125, 150, 175, 200 Microwell array for each diameter: 4x10 Hydrophobic and porous areas around microwells : Width (2 mm) ×length (3.58 mm) Impedance wire dimension (Ti-Au 110 nm): width(μm) × thickness (nm)×length(mm) (Narrower wire) 100×110×3 (Widther wire) 1000×110×300 Half-circle electrode: 2mm diameter, 0.5 mm gap between two electrodes Electrical pad : 3mm×3mm Master mold for PDMS: length (3cm) × width (3mm) × inlet/outlet diameter(2mm)	For 2D and 3D (spheroid) cell culturing in single microfluidic chip with optical (for 3D cells) and electrical (2D cells) monitoring system.

4.4 Microfabrication protocols

All microchips used in this study were fabricated out of negative photoresist Ormocomp through standard UV lithographic processing. In addition to standard lithography, adhesive bonding techniques were applied to enclose the microfluidic channels. In this chapter, the microfabrication protocols used for creating round shape Ormocomp microstructures are described (4.4.1) along with implementation of metal elements, including micromirrors, electrochemical sensors and impedance electrodes, into Ormocomp microstructures (4.4.2). Additionally, surface modifications targeting wettability and porosification (4.4.3), and, finally, Ormocomp-Ormocomp and Ormocomp-PDMS bonding protocols (4.4.4) are outlined. Figure 13 illustrates the fabrication of round cross-sectional shape microstructures, metallizations, surface modifications and bonding processes applied to create round cross-sectional microchannel and microwells.

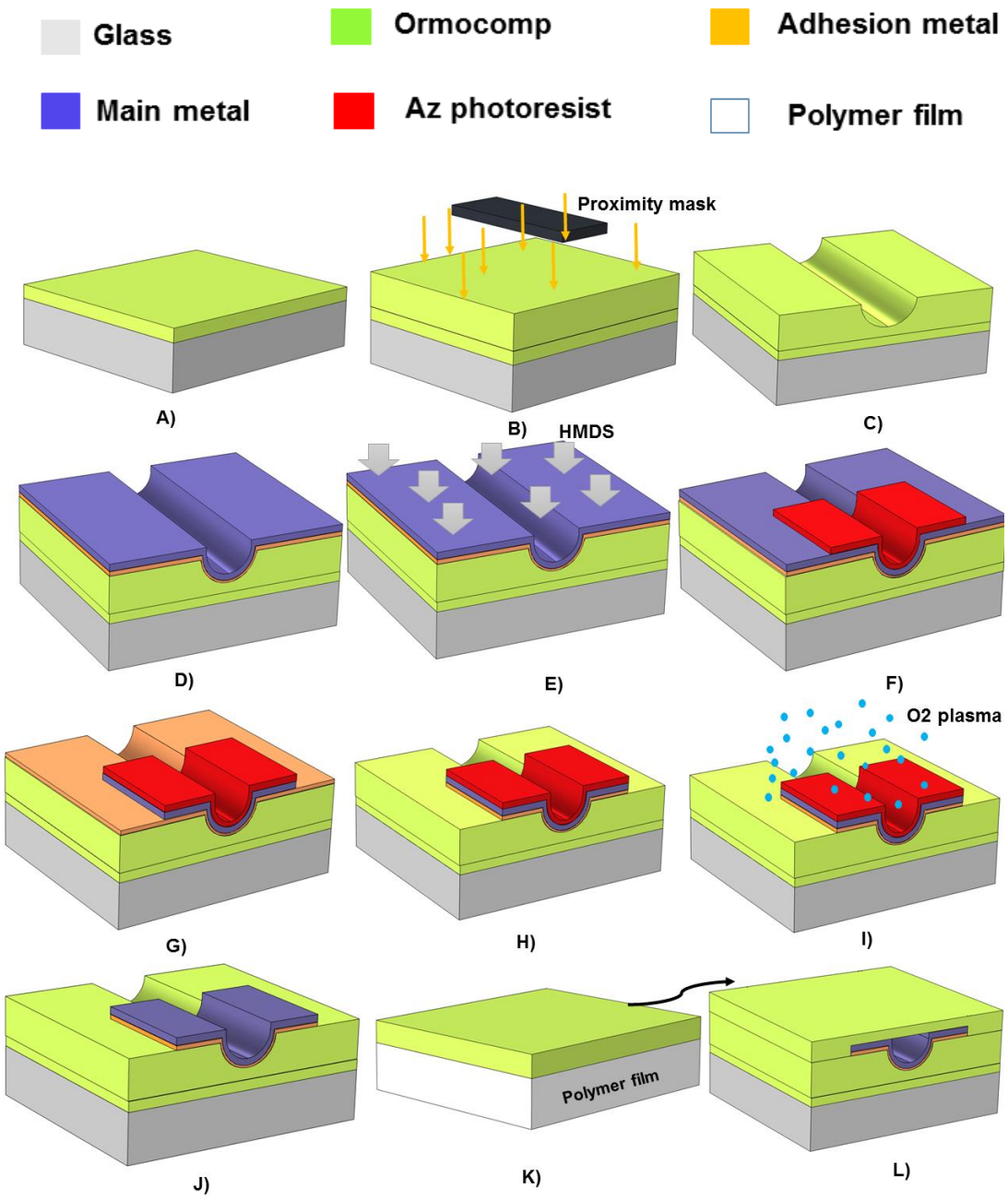

Figure 13. Schematic of fabrication process of metal sensors into Ormocomp-based microchannels. For fabrication of round cross-sectional microchannels: A) Spincoating and UV exposure of the bottom layer B) spincoating and masked UV exposure of the microchannel layer and C) Ormocomp development and hard bake. Metallization process: D) Deposition of the adhesion layer (17 nm Cr or 5 nm Ti) and main metal layer (Ag, Au, Al or Pt), E) HDMS coating, F) spincoating and patterning of the AZ photoresist, G) etching of the main metal layer and H) etching of the adhesion layer. Surface modification: (I) surface treatment for improving bonding strength by oxygen plasma and J) resist removal with AZ 100 remover. Bonding process: K) Third layer of Ormocomp was spin-coated on transparent plastic sheet (3M) then UV flood exposure was followed by adhesive bonding on career wafer. L) Final chip. Illustration by the author. © Ashkan Bonabi, 2019.

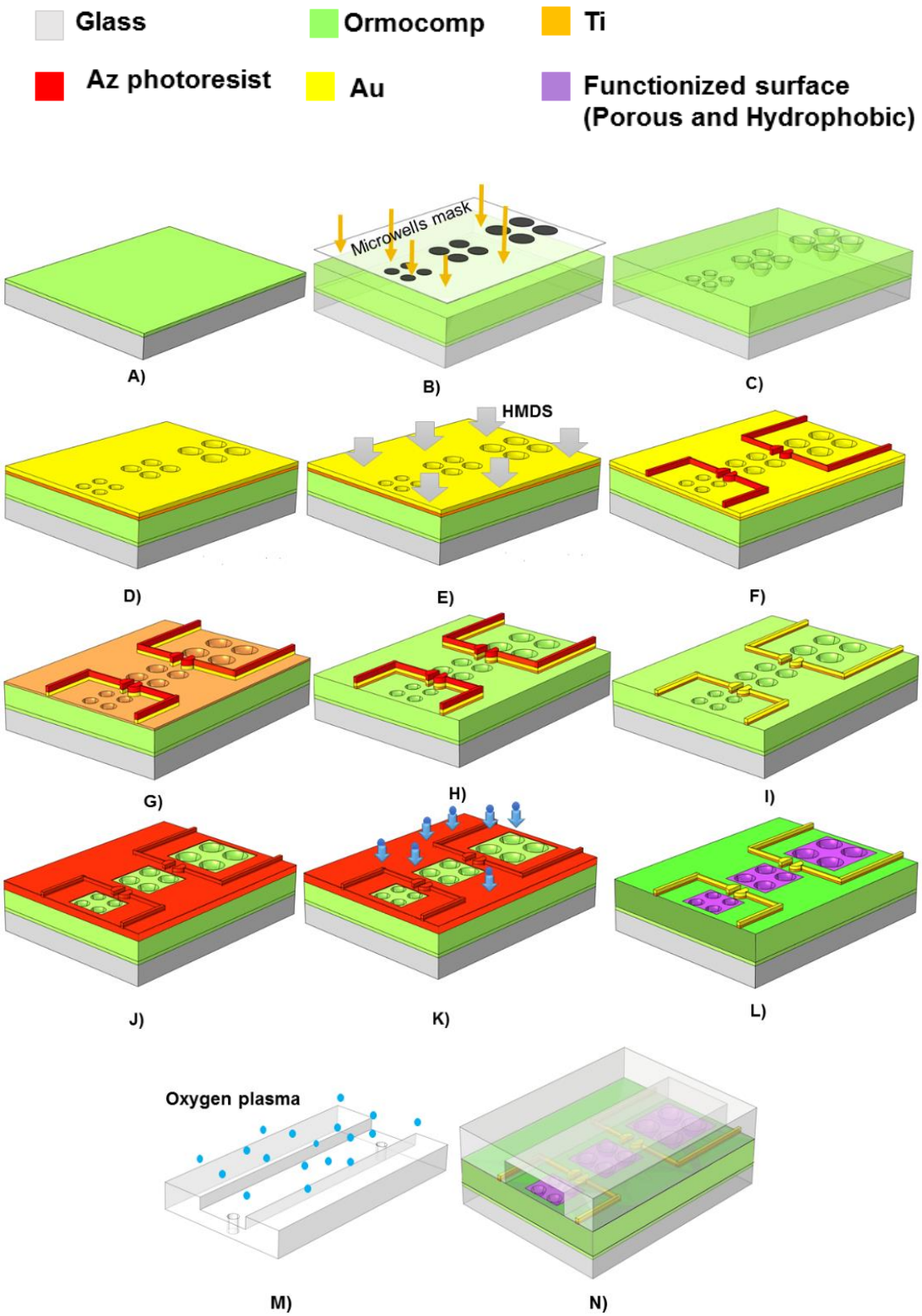

Figure 14. Schematic of fabrication process of Ormocomp microwells and impedance electrodes. For fabrication of round cross-sectional microwells: A) Spincoating and UV exposure of the bottom layer, B) spincoating and masked UV exposure of the microwell layer, C) Ormocomp development and hard bake (200 °C for 2 hr). Metallization process: D) Evaporation of adhesion layer (Ti 10 nm) and main metal layer (Au 100 nm). Patterning electrodes: E) HMDS coating, F) spincoating (10 µm) and patterning (multiple UV exposures) of the AZ photoresist (AZ 4562), G) etching of Au with 35 °C aqua regia for 10 sec, H) etching of the adhesion layer (Ti) in silver etchant for 5 min and I)

resist removal by AZ 100 in RT. Pattering areas for surface modification (microwells). Surface modification: J) Coating Az photoresist (AZ 4562) (12 um) and patterning (multiple UV exposures) areas for surface modification, K) porousification of Ormocomp microwells with oxygen plasma and deposition of fluorpolymer gas on top of patterened area of Ormocomp (hydrophobicity process) and L) resist removal with AZ 100 remover. Bonding process: M) Semi-cured PDMS was prepared and oxygen plasma was applied for surface treatment on PDMS. It was then followed by adhesive bonding. N) Final chip. Illustration by the author. © Ashkan Bonabi, 2019.

4.4.1 Fabrication of round shape Ormocomp microstructures

The first layer of Ormocomp was spin-coated (6000 rpm, 30 sec, 15 µm thick) on top of a pyrex glass substrate. Then, UV flood exposure (76 mJ/cm²) and bakeing in an oven at 95 ºC for 30 min (Fig. 13A, 14A). The spin-coating of the second layer was carried out at 2000 rpm (30 sec, 35-40 µm) for microchannels and at 800 rpm (15 sec, 130-150 µm) for microwells. The second layer was exposed in proximity mode (400 µm gap) with exposure doses of 19 mJ/cm² (microchannels) (Fig. 13B) and 450 µm gap and 43,7 mJ/cm² (microwells), and then baked at 95 ºC for 30 min in an oven (Fig. 14B). The dosage should not be less than the aforementioned amount, otherwise negative slope can be appear in the corners of microstructures (more details are presented in Section 5.1). Finally, both Ormocomp layers were developed in Ormodev developer for 5 min and hardbaked on a hotplate at 200 ºC for 2 hr (Fig. 13C, 14C).

4.4.2 Implementation of metal elements

Ormocomp metallization protocols were developed for aluminum (Al), platinum (Pt), silver (Ag) and gold (Au). Chromiume (Cr, 20 nm) was applied as the adhesion layer for Al and Pt (main metals) and titanium (Ti, 5-10 nm) for Ag and Au (main metals). Ti-Ag and Ti-Au were deposited by evapotation whereas Cr-Al and Cr-Pt by Sputtering (Fig. 13D, 14D).

For implementing mirror elements, highly reflective Al (100 nm) was used (Fig. 12, design I), whereas Pt (220nm), Au (30 nm) and Ag (100 nm) were predominantly characterized with the objective of electrical applications. Etching and lift-off parameters for the earlier described metals were optimized at this stage. After optimizing etching parameters, metal step coverage was also studied for implementation of metal elements on top of curved microstructures, and then metal-sensing elements were implemented on curved cross-sectional microchannel and planar surface of the Ormocomp. For implementing electrochemical sensor elements, Pt (200 nm) was used in the final chip design (Fig. 12, design II). Finally, owing to its cell compatibility, Au (100 nm) was employed for fabrication of impedance electrodes for cell-monolayer monitoring (Fig. 12, design III).

4.4.2.1 Etching

For adhesion promotion of photoresist onto the deposited metal, vapor deposition of Hexamethyldisilazane (HMDS) was applied to the metal surface in a 150 °C oven for 30 min (Fig. 13E, 14E). To ensure appropriate metal step coverage (over microchannel edges), thick layers of AZ4562 photoresist (6 µm, 4000 rpm and 30 s) were spin-coated for protecting the thin-film metal on the edge of the microchannel for protection against the etching process during the next steps. However, in the case of microwells - because of the thermal process (hardbake for 2 hr at 200 °C), which led to wafer warping – as such, a low spinning speed was applied (2000 rpm, 9 µm thickness). Subsequently, the photoresist was exposed (UV exposure dose of 1140 mJ/cm² for 60 sec) for patterning of the metal (Fig. 13F, 14F). The development of photoresist was performed in AZ 826 MIF for 3-4 min. However, because of the thick layer of residual AZ 4562 resist inside of the microwells after development, another UV exposure (aligned to the previous exposure) was carried out with a 380 mJ/cm² dose for 30 sec with a subsequent 3-min development time. Lithography with aligned exposures were repeated until no AZ 4562 resist remained inside of the microwells. AZ resist hardbaking was completed at 115 °C for 2 min on a hot plate. Finally, different etching process were developed to establish the metal adhesion layers (Fig. 13G, 14G) and main metal layers (Fig. 13H, 14 H), as described in Table 5.

Table 5. *Etchants for metal etching*

Metal (nm)	Etchant	Note
Al	Phosphoric acid-based (15% Nitric acid and 85% Phosphoric acid)	Adhesion loss of Ormocomp from glass
	AZ 351B alkaline photoresist developer	Basic pH
Ag	Mixture of deionized (DI) water, hydrogen peroxide and ammonium hydroxide 12:1.8:1 (volumetric ratio)	RT
Au	Aqua regia (nitric acid and hydrochloric acid 1:3)	RT or 35 °C (microwells)
Pt	Aqua Regia	55°C
Cr	Cr etchant (6% nitric acid and 16% ceric ammonium nitrat in water)	RT
Ti	Mixture of deionized (DI) water, hydrogen peroxide and ammonium hydroxide 12:1.8:1 (volumetric ratios)	RT

4.4.2.2 Lift-off

In this study, a lift-off process was developed exclusively for Ti-Ag (40 nm). After fabrication of microchannels by UV lithography (exposure dose ≥ 19 mJ/cm²), AZ4562 photoresist (6 µm, 4000 rpm and 30 sec) was spin-coated

and patterned (with dark-field mask) by a UV exposure dose of 1140 mJ/cm^2. After development, Ti-Ag (5-35 nm) was evaporated and AZ 100 remover (in room temperature for 24 hr) was used instead of the usual lift-off solvent (mr-Rem 400) based on better stability of Ormocomp adhesion to the main glass substrate.

4.4.3 Surface modification

Following the isotropic wet-etching process, the surface chemistry changed dramatically, potentially manifesting as challenges with respect to bonding and cell adhesion. Plasma technology enables tailoring of the surface chemistry and surface wettability with a view to improving bonding strength or creating pores that induce cell repellency. Three types of surface modifications were carried out in this study with plasma technology. Surface treatment with oxygen plasma was applied for designs II and III to foster better bonding between the carrier wafer and third layer of Ormocomp. For Au and Pt, an oxygen-plasma treatment (1 min) was applied (RIE Oxford Plasmalab 80) after wet etching and resist removal. In the case of Ag, the photoresist was removed only after oxygen plasma (Fig. 13I) to avoid oxidation of Ag. However, when etching Al by alkaline photoresist developer, the surface chemistry of Ormocomp did not change, thus oxygen plasma was not required. After surface treatment, AZ resist was removed by AZ 100 remover (Fig. 13J).

For altering surface wettability to create cell-repellant surfaces (for 3D-spheroid culturing), localized pore formation and fluoropolymer coating was applied to the microwells.

After resist removal by AZ 100 remover (Fig. 14I), the 12-µm AZ 4562 photoresist (1500 rpm and 30 sec with 50-sec softbaking on a hotplate at 100 °C) was spun. Next, it used as a hard mask, so was patterned using UV lithography (UV exposure dose of 570 mJ/cm^2). Multiple UV exposures were repeated with 380 mJ/cm^2 doses with a subsequent 3-min development time for eliminating possible AZ residuals inside of the microwells (Fig. 14J).

Then, pores were formed by reactive ion etching using oxygen plasma (RIE Oxford Plasmalab 80). Before the process, the chamber was cleaned with sulfur hexafluoride (SF6) and oxygen plasma for 30 min. Next, 200 W plasma with a 20-min etching time was employed (other parameters: pressure - 250 mTorr, Oxygen flow - 45 sccm and Ar flow - 5 sccm) (Fig. 14K). Hydrophobic coating (thin layer of fluoropolymer) was grown by plasma-enhanced chemical vapor deposition (PECVD) (CHF_3, 100 sccm, 50W, 250 mTorr, RT and 5 min) (Fig. 14K).

In order to prevent hydrophobic layer peel-off from the Ormocomp surface, resist removal was carried out in a AZ 100 remover (RT) for 20 min, after which the sample was handled and rinsed without mechanical pressure and very carefully with isopropanol and water (Fig. 14L).

4.4.4 Bonding

Enclosed Ormocomp structures were achieved through adhesive bonding [142], but the process was very sensitive to alterations of the physico-chemical properties of the surface, which may change, e.g., in the context of metal etching. Thus, in this study, Ormocomp adhesive bonding for embedded metal elements, like mirrors and electrodes, were developed (Fig. 12, designs II and I). After oxygen plasma (RIE Oxford Plasmalab 80) and resist removal, the third layer of Ormocomp was spin-coated (4000 rpm, 20 µm and 30 sec) and exposed on a transparency film (3M transparent plastic film) (Fig. 13K) similar to previous work [142]. Next, the cured Ormocomp that was exposed was laminated on top of the microstructures and heated to 95 °C for 3 min, followed by gradual cooling to RT (Fig. 13L). Adhesive bonding of Al at room temperature (RT), without additional oxygen plasma treatment, thus allowed sealing of the Ormocomp microchannels.

In addition to Ormocomp-Ormocomp bonding, PDMS was applied for adhesive bonding of Ormocomp-based cell-culturing devices (Fig. 12, design III). The strong oxygen permeability was the main reason to choose PDMS over Ormocomp for bonding of design III. For PDMS bonding of Ormocomp, the master mold (Table 4, design III) was fabricated from SU-8 100 negative photoresist under clean room conditions. The PDMS prepolymer was mixed with the curing agent at a ratio of 15:1 and poured onto the SU-8 mold to achieve an approximately 5-mm thick PDMS microchannel wafer. After degassing, PDMS was semi-cured in a 75 °C oven for 40 min, peeled off from the master mold and treated with oxygen plasma to activate the surface (60 W, 500ml/min for 60 s with TePla 400) (Fig. 14M). Finally, the PDMS microchannels were diced, bonded on top of the Ormocomp microwells and cured at 80 °C in the oven overnight (Fig. 14N). To have strong adhesion between PDMS and the Ormocomp surface, a 500-1000-gram weight was applied on top of PDMS during the curing process.

4.5 Material characterization methods

4.5.1 Ormocomp microstructures

The effects of UV exposure dose and gap on the height (h) of the microstructures (microchannels and microwells) were measured with three replicate samples for several microchannel widths (20-200 µm), microwell diameters (100-200µm) and nominal layer thicknesses (35, 45 and 130 µm) using a Dektak/XT Profilometer with a 15-mg stylus force and scan resolution of 0.02 µm. The effects of UV exposure dose on microchannel and microwell cross-sectional shape were determined with minimum of three replicate samples of each type using a scanning electron microscope (SEM EBL Zeiss

Supra 40, Oberkochen, Germany). Before SEM imaging, the microchannels and microwells were diced with a dicing saw and sputtered with 20-nm Cr (microchannels) or Au (microwells) layers. The SEM images of the microchannels were analyzed with Matlab. The radius of curvature (r) of the microchannel cross-section was determined via in-house written Matlab code. For each case, three independent images were analyzed to calculate the variances. The calculations were also repeated six times for each image and these results were averaged to yield robust results and estimation of possible errors (Publication I). To characterize the impact of UV exposure on the shape of the microwells, four independent SEM images were analyzed by in-built function of Matlab. In addition to radius of curvature (r), residual thickness and depth of the microwells were also determined and variances between four microwells of each type were calculated and reported (Publication IV).

4.5.2 Bonding strength

The bonding strength test was carried out with double-sided transparent adhesive tape (double sided, removable Scotch tape, 3M, Maplewood, MN, USA) of the size 30 ×20 mm^2 was applied manuallty on top of the bonded areas and peeled off by hand, pulled fast and rigorously after ca. 5 s. The results were investigated by visual characterization under light microscope and by scanning electron microscope (SEM) (Publication III).

4.5.3 Stability of surface modification

The effects of various etchants and oxygen plasma treatments on the Ormocomp surface properties were measured with the advancing and receding contact angles through contact-angle goniometry in all cases before and after treatment (Publication III). The contact angles of the porous-hydrophobic layer and native Ormocomp were measured for 45 days to confirm stability of the surface properties (both cell adhesive and cell repellant) for cell-culturing applications (Publication IV).

4.5.4 Characterization of metallization

The sheet resistances of the thin-film metals on Ormocomp were measured in the center and edges of each wafer by a four-point probe meter, averaged and multiplied by the layer thickness to calculate the bulk resistivity (ρ) [17]. Furthermore, metal wires with various widths and lengths (Table 4) were fabricated. The wire resistances were measured by a multimeter and compared with theoretical resistances computed based on the wire dimensions and measured bulk resistivities (Publication III). Metal adhesion was assessed with and without adhesion layers using adhesive tape (scotch tape), which was

applied on top of the metallized surface and then peeled off rapidly and forcefully. Additional visual characterization was performed under light microscope and ultrasound testing in acetone bath (full power, 5 min; Publication III).

4.6 Experimental set ups

In this section, the main experimental setups used in this study are reviewed, including microchip capillary electrophoresis (4.6.1), optical detection with the help of micromirrors (4.6.2) and electrochemical detection with of the assistance of microelectrodes (4.6.3). Furthermore, microfluidic cell-culturing conditions and impedance detection of cell monolayers are described in chapters 4.6.4.

4.6.1 Microchip capillary electrophoresis

Before use, the microchannels were sequentially rinsed with DI Milli-Q water and separation buffer by negative (vacuum) pressure for 2-5 min each. Before analysis, the microchannels were filled with fresh buffer solution and quantities of 20 µL for buffer inlet, 20 µL for buffer waste and 10 µL for sample waste reservoirs were used. Lastly, 8 µL of the sample solution was applied into the sample reservoir followed by immediate application of the injection voltage.

In Publication II, a computer-controlled, high-voltage power supply was employed to apply the separation voltages and record current readings. Sample introduction was performed in pinched injection mode (electric field strength - 800 Vcm-1) for 20 sec and the effective separation length (from intersection to the detection window) was 40 mm for measurement on the mirror side and 39 mm for measurements on the channel side without the mirror. The MCE analyses were performed in 20-mM sodium borate buffer (pH 10.0) under electric field strengths of 600 Vcm^{-1} (voltage applied to the separation inlet = 3.6 kV). In order to prevent sample leakage, small push-back voltages (3.0 kV) were applied to the sample inlet and sample waste during separation.

In Publication III, a commercial bipotentiostat with integrated power source (Micrux) was employed to apply the separation voltages. In this case, sample introduction was performed in floating mode (electric field strength - 800 Vcm^{-1}) and the effective separation length (from intersection to the electrodes) was 30 mm. The MCE analyses were performed in 20-mM 2-(N-Morpholino) ethane sulfonic acid (MES) hydrate (pH 6.5) for 10-15 min buffer under an electric field strength of 300 Vcm^{-1} (voltage applied to the separation inlet = 1 kV).

4.6.2 Mirror set up

Analytical characterization of embedded mirrors (Fig. 12, design I) was carried out by halogen lamp (100 W) or high-power lasers as excitation sources. For 488-nm laser measurements, a continuous wave of argon laser (488 nm, 13 mW) was utilized and for a 355-nm UV range, a pulsed UV laser (355 nm, 15 µJ at 1 kHz) was utilized (Publication II).

The impact of micromirrors on optical-detection sensitivity was determined by comparing the fluorescence signal intensities achieved with the mirror and without it. For performance study of planar and concave mirror layouts, the limits of detection (LOD) were determined based on residual standard deviations by following the ICH guidelines for validation of analytical procedures (Q2). For microchannels with embedded planar mirrors (Fig. 12, design I), the signal enhancement was demonstrated in the microchip capillary electrophoresis analysis, whereas the concave, embedded micromirrors were characterized with a view to single-cell analysis (Publication II).

4.6.3 Electrochemical detection setup

First, the microchip (Fig. 12, design II) was rinsed with DI Milli-Q water (Millipore, Bedford, USA) and 20 mM MES (pH 6.5) buffer for 10-15 min. The injection and separation voltages (1000 V) were applied with an external power source. The amperometric detection of the chemical standard (20 µM acetaminophen) was performed by applying a working electrode potential of 0.8 V (Publication III).

4.6.4 Cell culturing and monitoring

The single cells analyzed with concave micromirrors were derived from the BHK-CHIKV-NCT cell line cultured off-chip in Dulbecco's modified Eagle's medium with 4.5 g/l glucose, 580 lg/ml L-glutamine and 25mM HEPES supplemented with 7.5% fetal bovine serum, 2% tryptose phosphate broth, 1 mM sodium pyruvate, 100 IU/ml penicillin, 100 lg/ml streptomycin and 5 lg/ml puromycin, then incubated at 37 °C, 5% CO2 and 95% humidity (Publication I).

The cell lines used for on-chip cell culturing (Publication IV) were human hepatoma cells (Huh-7) maintained in DMEM cell-culturing medium supplemented with 10% fetal bovine serum, 1% non-essential amino acids (Gibco, Paisley, UK), 10 000 U/ml penicillin and 10 000 µg/ml streptomycin (Gibco, Grand Island, USA) in standard culture conditions (+37 °C, 5% CO2 and 95% humidity) and sub-cultured when reaching <90% confluence. Before seeding into microchannels (Publication IV), the cells were detached from the culture flask. The microwell-based chip was flushed with 70% ethanol (aq) and

complete growth medium. Next, cells (2.5 M/mL) were seeded into the microchip device and allowed to settle for 30 min. The initial flow rate was set at 3.5 µl/min (5.83 mm/min) for the first 8 h for removing bubbles, then at 1.4 µl/min (2.33 mm/min). After given periods of time (24, 48, 72 and 96 hr), the cells were imaged and stained for analysis (Publication IV). In addition, impedance spectra were recorded (Fig. 12, design III) to evaluate cell monolayer confluence during cell culturing. PalmSens4 potentiostat/EIS analyzer was utilized for measuring the spectra once every hour for 24, 48, 72 and 96 hr at a frequency range of 5-100 000 Hz (n = 44) using AC with a voltage of 10 mV (Publication IV).

5 RESULTS AND DISCUSSION

The main results obtained in this study are briefly described in this chapter, addressing controlled fabrication of the round cross-sectional Ormocomp microstructures by adjusting the UV-curing conditions (5.1), considerations for step coverage and metal adhesion (5.2) and Ormocomp bonding over metal (5.3). Additionally, material compatibility issues (5.4) and device performance in selected applications (5.5) are discussed. More detailed information can be found in Publications I-IV.

5.1.1 Regulated UV exposure of Organically Modified Ceramics

The key finding in this thesis was that the residual layer formed upon overexposure of Ormocomp can be used for regulating the cross-sectional shape. In this work, the effects of UV exposure parameters (UV dose and gap) on the shape of the cross-sectional profile of the microchannels and microwells were examined.

5.1.2 Effect of UV exposure doses

Overregulation of exposure of Ormocomp in proximity mode enabled implementation of microstructures with a round cross-sectional shape in a controlled manner. The effect of UV exposure dose (ranging from 13 to 48 mJ/cm²) was assessed with various microchannel widths (20 to 200 µm) and microwell diameters (100 to 200 µm). The nominal thickness of the Ormocomp layer was 35 µm (microchannel) or 130-150 µm (microwells). When examining the impact of UV exposure dose, a fixed proximity gap of 400 µm (microchannel) and 450 µm (microwells) was opted for. Under these conditions, round-shaped cross-sections with a tunable radius of curvature (r) was obtained for microchannels and microwells.

The shape of the microchannels with fixed dose is shown in Figure 15 and the evolution of the shape as a function of the exposure dose in Figure 16 for various channel sizes. For channel widths ≤30 µm, round cross-sectional shapes were reproduced only at the lowest UV dose ≤19 mJ/cm² (Fig. 15A), whereas higher UV doses fully filled the channels with a residual layer (Fig. 16A, B, C, D). All microchannels narrower than 150 µm (nominal width) became round cross-sectional when exposed to UV with doses ≥19 mJ/cm² (Fig. 15), whereas microchannels wider than 150 µm featured vertical-walls (Fig. 15F) and flat, planar bottom under these conditions (Fig. 16I, J). However, the wider channels also became round cross-sectional by exposure to higher dose (Fig. 16 K L). By further increasing the width of microchannel

beyond 150 μm, even higher exposure dose was required to produce a round cross-sectional profile. Again, the evolution of the radius of curvature (r) by increasing UV exposure dose for different microchannel widths is presented in Figure 16.

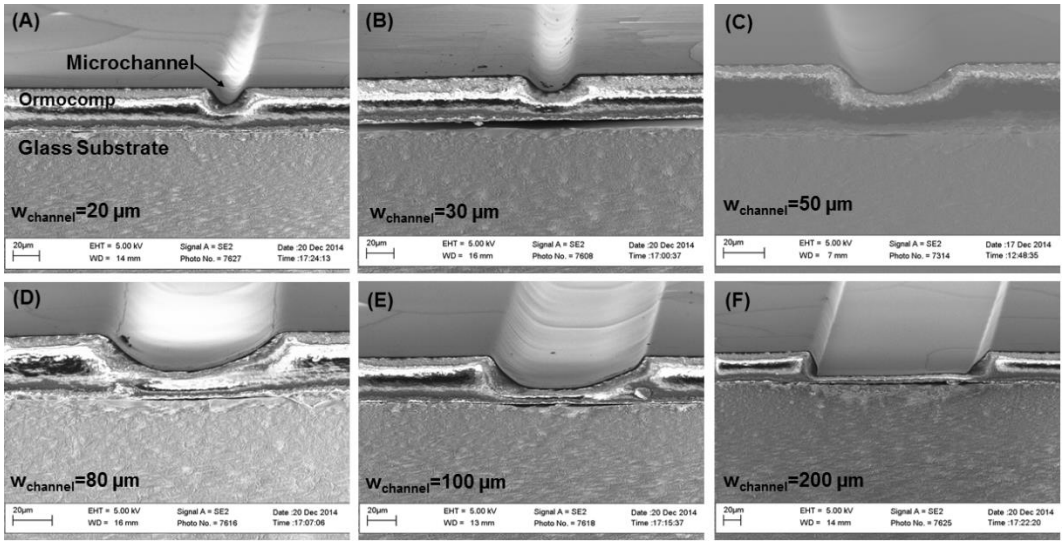

Figure 15. Formation of round cross-sectional shape profile as a function of the microchannel nominal width. In all cases, the nominal Ormocomp layer thickness was 35 μm, UV exposure dose 19 mJ/cm² and proximity gap during UV exposure 400 μm. All images reproduced from publication [I] are with permission of American Institute of Physics (AIP).

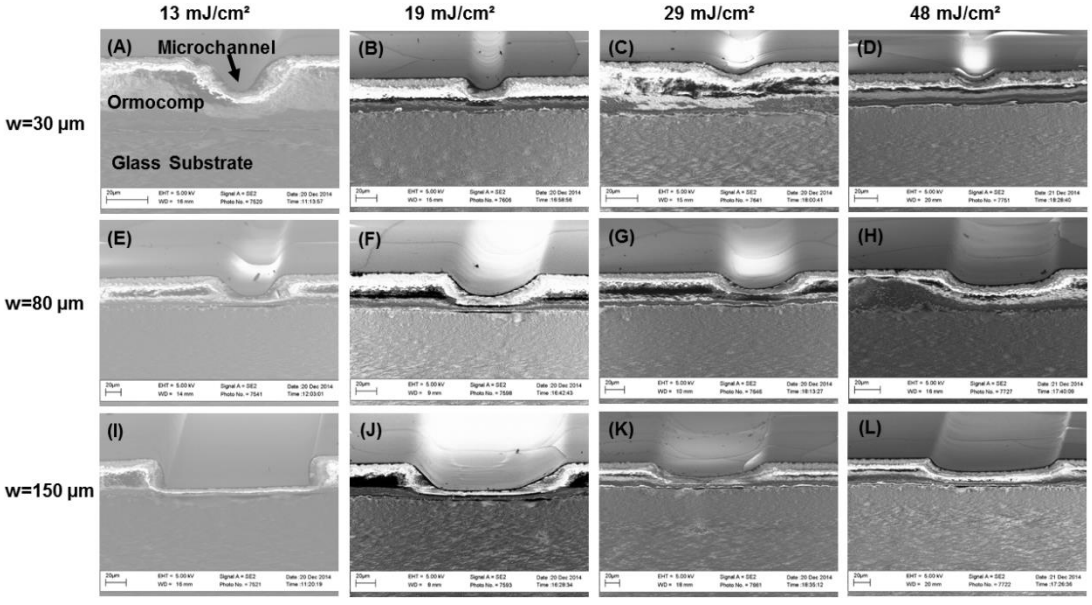

Figure 16. Electron micrographs illustrating evolution of microchannel shape with 30-, 80- and 150-μm diameter widths under UV exposure doses from 13 to 48 mJ/cm². In all cases, the nominal Ormocomp layer thickness was 35 μm and proximity gap during UV exposure 400 μm. All image adapted from publication [I] are with permission of American Institute of Physics (AIP).

Similar phenomena were observed for microwells. The shape of the microwells with diameters of 100 and 125 µm at fixed doses is shown in Figure 17 and the evolution of the shape as a function of the exposure dose in Figure 18 for 150 to 200 µm microwell sizes. By adjusting the UV exposure dose, a round cross-sectional residual layer was formed in microwells. For example, microwells with diameters between 100-125 µm and UV exposure doses of ≤26.6 mJ/cm² were required to produce round-shaped, cross-sectional profile (Fig. 17). For microwells larger than 150 µm, negative slope was observed at corners (Fig. 18A, F, K), which poses a major challenge for subsequent photolithography processes, such as metallization.

Upon increasing diameter, higher UV exposure doses were needed to form round cross-sectional profiles (Fig. 18 for 175- and 200-µm diameters). Nevertheless, similar round-shaped profiles could be reproduced for all sized microwells by adjusting the UV exposure dose (Fig. 18).

On the basis of SEM characterization, round cross-sectional profiles were formed in both microchannels and microwells via residual layer formation upon controlled overexposure. In both cases, round cross-sectional profiles were produced with lower UV exposure doses in narrower microstructures (Fig. 16A, E; Fig. 17A, E), whereas wider microstructures required greater UV exposure doses (Fig. 16K, Fig. 18C). However, owing to thicker layers of Ormocomp (130 µm) in microwells, higher UV exposure doses were required (Fig. 18D) compared with microchannels (35-µm thickness) to yield the round cross-sectional profile (Fig. 16K).

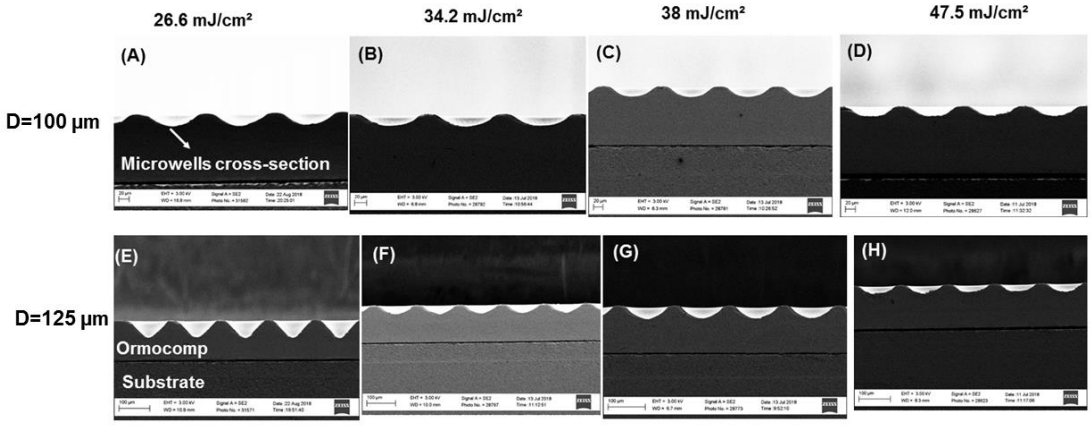

Figure 17. Electron micrographs depicting the evolution of shape forming in 100- and 125-µm diameter microwells under UV exposure doses from 26.6 to 47.5 mJ/cm². In all cases, the nominal Ormocomp layer thickness was 130-µm and proximity gap during UV exposure 450-µm (Publication IV).

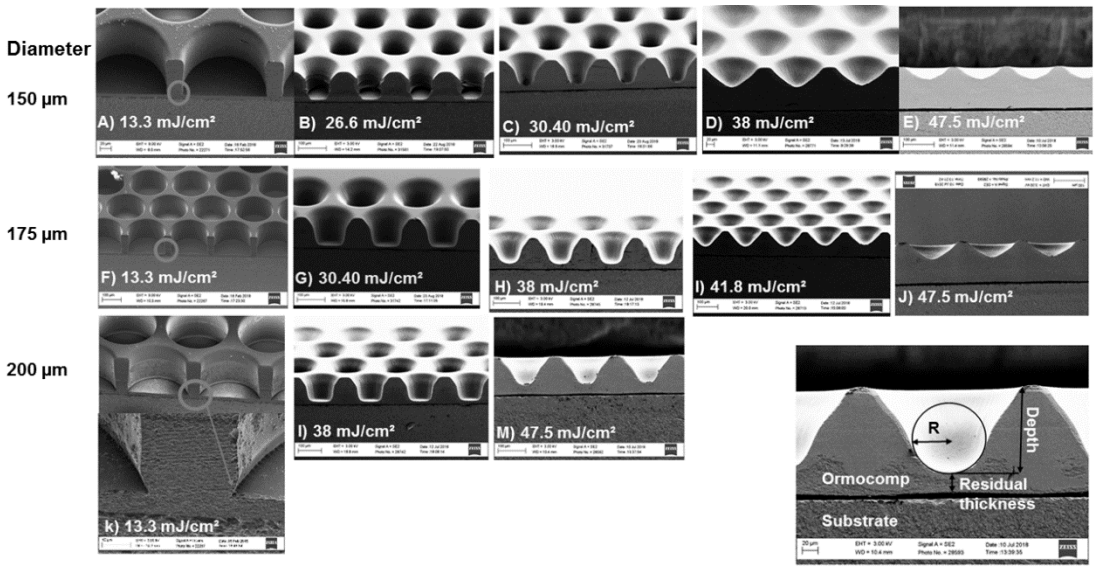

Figure 18. The impact of UV dose on the Ormocomp microwell profiles for 150-, 175- and 200-µm wells (nomical diameter) and an illustration of the circle fit (in SEM images) performed with the help of Matlab (Publication IV).

For better quantification of the impact of the residual layer on the cross-section shap, the radius of curvature (r), the height of microstructures and the thickness of residual layer were evaluated as a function of the UV dose: The radius of curvature was determined with the help of a circle fit in SEM micrographs in Matlab (Figure 18) and the height of the microstructures was determined by a profilometer. The residual layer thickness was then determined on the basis of these data. It was recognized that by increasing UV exposure dose, the residual layer became thicker and the height of the microchannels and microwells was reduced (Fig. 19B, Fig. 20A). Meanwhile the radius of curvature became larger (Fig.19C, Fig. 20B) and the microwell shallower (Fig. 20 A). However, the layer thickness also plays a role in terms of achievable shape, which is illustrated by the difference between the radius of curvature in microchannels (layer thickness 35 µm, Figure 19) and microwells (layer thickness 130 µm, Figure 20). However, in both cases, the thickness of the residual layer reaches saturation at ca.48 mJ/cm². To account for the experimental variation (microfabrication) and the error in image analysis (Matlab circle fit), the impact of UV dose was determined from at least n=3 replicate samples and n=3 replicate determinations in each case. A more detailed error analysis is given in the original paper (publication I).

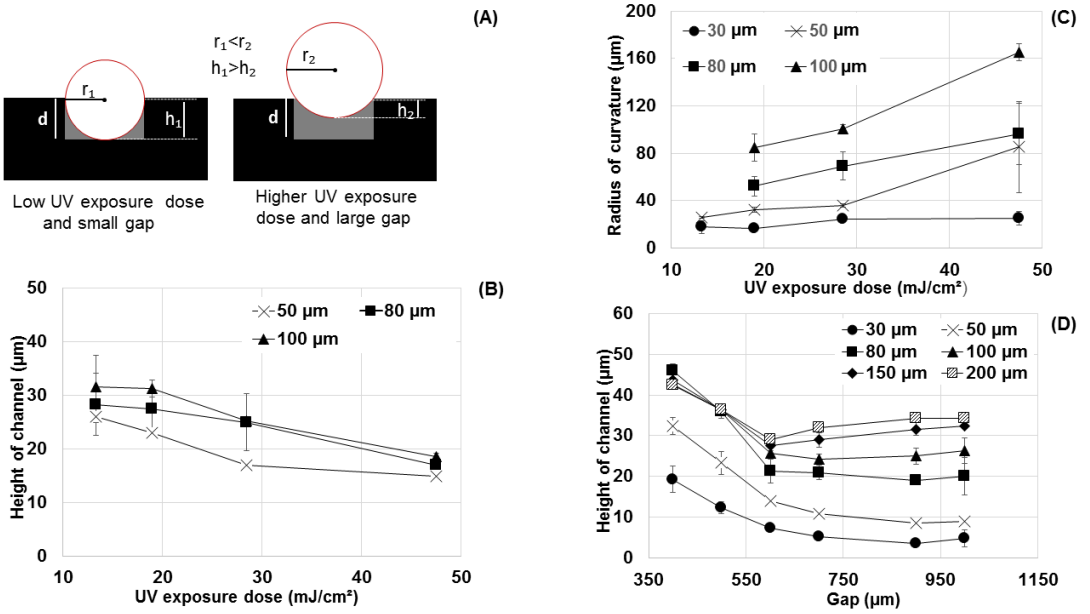

Figure 19. Demonstration of the effects of the UV dose and proximity gap on microchannel height (h) and radius of curvature (r). The symbol, d, represents the nominal thickness of the microchannel layer. Residual layer thickness is the difference between the nominal thickness (d) and the measured height (h) A) Curvature behavior under exposure dose and gaps. B) Microchannel height (h) as a function of UV exposure dose. C) Microchannel radius of curvature (r) as function of UV exposure dose and in all cases, the nominal Ormocomp layer thickness was 35 µm and proximity gap during UV exposure 400 µm. D) Microchannel height (h) as a function of the distance of the proximity gap from 400 to 1000 µm. The Ormocomp layer thickness was 35 µm and the UV exposure dose was 19 mJ/cm². The error bars represent the standard deviation from three replicate samples and three replicate determinations (radius of curvature). Adapted from Publication [I] with permission of the American Institute of Physics (AIP).

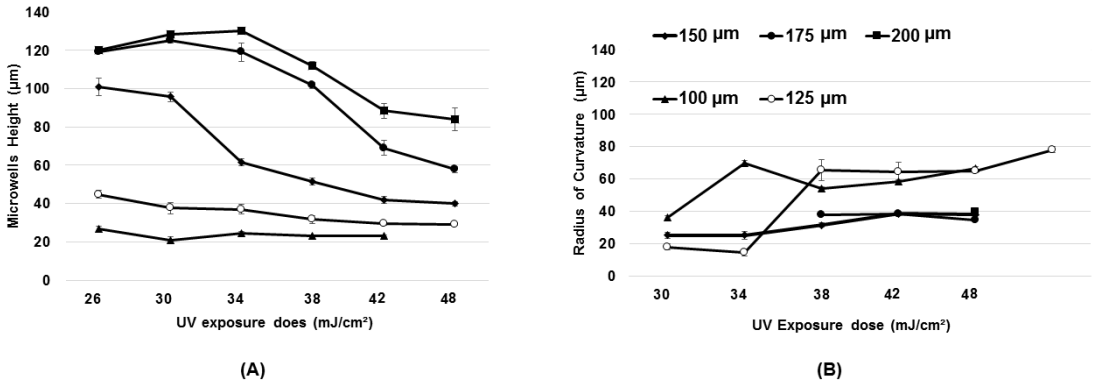

Figure 20. Effect of UV dose on microwells' (A) height (h) and (B) radius of curvature (r). The error bars represent the standard deviation from four replicate samples and four replicate determinations (radius of curvature). (Publication IV)

5.1.3 Effect of proximity gap

The effect of proximity gap on the evolution of the microchannel and microwell heights (h) and the radii of curvature (r) was also examined as a function of microchannel width (20 to 200 µm) or microwell diameter (100 t0 200 µm).

The study was carried out using gap distances ranging between 400 and 1000 µm for microchannels with layer thickness of 35 µm and constant UV exposure doses of 19 mJ/cm². In the case of microwells with a layer thickness of 130 µm, proximity gap distances of 450 and 990 µm were used with a constant UV exposure dose of 48 mJ/cm².

It was observed that the microchannel height (h) decreased as a function of gap distance from 400 to 600 µm (Fig. 19D). Residual layer thickness became saturated (growth rate almost constant) after the 600-µm gap. It was also noticed that a similar effect (evolution of round cross-sectional shape) was obtained by tuning the gap (constant UV exposure dose) as well as with tuning the UV exposure dose (constant gap distance). The narrower the channel, the sooner it filled with the residual layer. Similarly, the wider channels filled more with the residual layer if the gap distance was increased (Fig. 19 D).

In microwells, by increasing the proximity gap, radius of curvature became larger and microwells became shallower (Fig 21A and B), as illustrated with SEM images in Figure 21C and D. The impact of the proximity gap was thus similar in both microchannels and microwells. However, in the case of microwells specifically, based on the thicker layer of Ormocomp, the height of the microwells diminished smoothly, whereas in microchannels, the residual layer thickness saturated at a proximity gap of 600 µm.

It was concluded that high sensitivity of Ormocomp and diffraction of light in the proximity (non-contact) exposure mode leads to tapered sidewalls and a round cross-sectional profile of Ormocomp microstructures. The resulting cross-section profile is unique to Ormocomp and different from the typical negative slope profile obtained by other commonly used negative photoresists, such as SU-8 [143, 144]. However, utilizing SU-8 lithography via overexposure from the backside, it might be possible to fabricate tilted, V-shape sidewalls [144], similar to Figure 15F, but controlled fabrication of round cross-sectional profiles similar to this work is likely not possible.

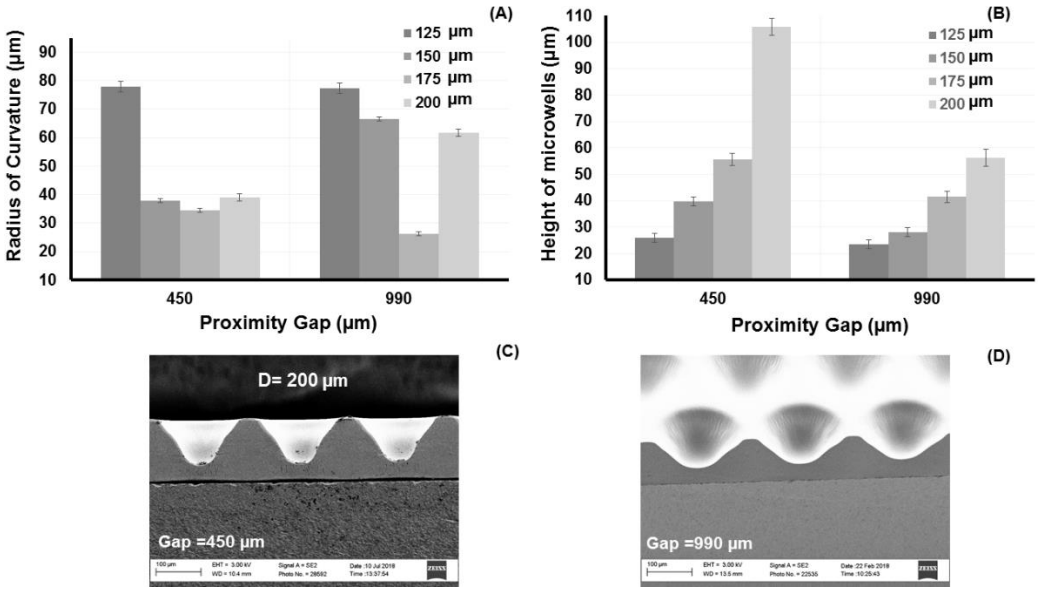

Figure 21. Effect of proximity gap on microwells height and radius of curvature as a function of microwells diameter. Effect of 450 and 990 µm gap on A) radius of curvature B) height of microwells with 125-,150-,175- and 200 -µm diameter. Electrone micrograph illustrates changing shape of microwells with diameter of 200 µm under proximity gap with C) 450 µm and D) 990 µm. In all cases, the nominal Ormocomp layer thickness was 130 µm, UV exposure dose was 47.5 mJ/cm² The error bars represent the standard deviation from four replicate samples and four replicate determinations. (Publication IV)

5.1.4 Effect of aspect ratio

The effect of the microchannel aspect ratio on the radius of curvature and height of the microchannels was further determined by varying the thickness (15, 35 or 45 µm) and microchannel width from 50 to 100 µm. A constant UV exposure dose of 19 mJ/cm² and proximity gap of 400 µm were applied across all cases. It is observed that the narrower and thicker the channel, the steeper round cross-sectional profile that was produced, whereas thinner and wider channels resulted in milder slopes closer to a circular arc (Fig. 22A, C, D). These results further evidence that the layer thickness also has effect, which explains the differences between microwells (130-µm thick) and microchannels (35-µm thick). Similar profiles were observed for microchannels (H/W=1.16) (Fig. 16A) and microwells (H/W=1.04) (Fig. 17E) featuring similar aspect ratios. For an aspect ratio of approximately 1, the round, cross-sectional profiles are steeper (Fig. 22C), however by decreasing the aspect ratio, the round cross-sectional profile became smoother (Fig. 18H, M; Fig. 22D). Thus, by altering the residual layer thickness and/or the aspect ratio, the UV exposure dose, and the proximity gap distance, the radius of curvature of the Ormocomp microstructures can be flexibly tuned for microchannels and microwells.

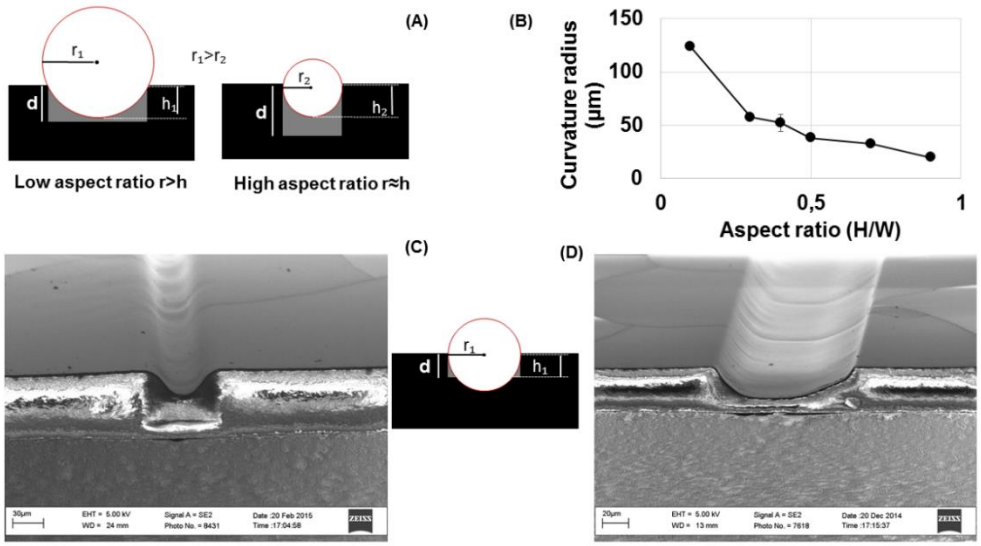

Figure 22. A) Schematic illustration of the effect of aspect ratio (h/w) on microchannel radius of curvature (r) and height of channel (h). The symbol d represents the nominal thickness of the microchannel layer. Residual layer thickness is the difference between the nominal thickness (d) and the measured height (h). B) The microchannel radius of curvature (r) as a function of aspect ratio under a constant UV exposure dose of 19 mJ/cm² and proximity gap of 400 µm. C) Electrone micrograph images of the cross-sectional shapes produced with aspect ratios of 0.9 (nominal channel width 50 µm and layer thickness 45 µm) D) 0.35 (nominal channel width 100 µm and layer thickness 35 µm). The error bars represent the standard deviation from three replicate samples and three replicate determinations. Adapted from Publication [I] with permission of the American Institute of Physics (AIP).

5.2 Metallization

In this work, Ormocomp metallization processes were developed to create strong adhesion, robust step coverage and different protocols for bonding of Ormocomp microchannels after various metal wet-etching processes. The developed metallization methods enable integration of metal elements (sensor and mirror) into Ormocomp microstructures.

The lift-off process in mr-Rem-400 and acetone solvents led to adhesion loss between Ormocomp and glass substrate. In contrast, Az 100 resist remover exhibit great compatibility with the lift-off process of Ormocomp. However, metal layers around patterned areas were not detached fully, referred to as residual metal. Based on the remaining of residual metal (Fig. 23), after lift-off, we focused on the development of etching-based metallization processes (Fig. 24) to accomplish clean and sharp-edged electrodes.

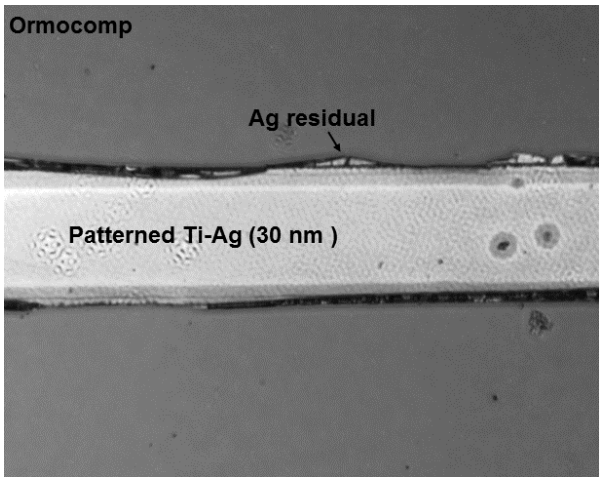

Figure 23. Patterned Ag with lift-off process. After the lift-off process, residual Ag remained around the edges of patterned areas (Publication III).

5.2.1 Step coverage

The step-coverage efficiency of the developed metallization processes were evaluated by patterning three types of wires with different length and widths across a 150-µm wide microchannel (nominal thickness of 35 µm). To produce tapered sidewalls and smooth edges, the microchannels were fabricated with a UV exposure dose of ≥19mJ/cm² (Fig. 24). The electrical resistance of the wires was measured to confirm continuity of wires over edges. It was observed that proper step coverage required deposition of thicker metal, of which an Al thickness of 140 nm and Pt thickness of 220 nm were required. Ag and Au required an approximately 100- and 30-nm thickness, respectively. The electrical resistance of wires patterned across the channel were in accordance with theoretical resistances calculated from sheet resistances of thin-film metals (Table 6 and 7).

Table 6. The average sheet resistance of the metallized areas (n=3 measurements) and comparison of the measured and theoretical resistances of the conductive wires patterned on top of the Ormocomp

Adhesion layer - Main Metal	**Ti-Ag (100 nm)**	**Ti-Au (30 nm)**	**Cr-Al (140 nm)**	**Cr-Pt (220 nm)**
Average sheet resistance (Ω/sq)	0.53±0.063	1.65±0.088	6.01±0.54	8.89±0.456
Calculated resistivity (Ω-cm)	0.53±0.063 e-5	0.49±0.0264 e-5	8.41±0.756e-5	19.5±1.0032e-5
Literature based resistivity (Ω-cm) for main metal	0.159e-5 [145] [146]	0.244e-5 [145]	0.265e-5 [145]	1.06e-5 [145]

Table 7. *The comparsion of the measured (n=3 measurements) and theoretical resistances of the conductive wires patterned on top of the Ormocomp*

Width (μm)	**Length (mm)**	**The measured resistance of the wires (kΩ)** **The theoretical resistance of the wires (kΩ) based on measured sheet resistance**			
50	15	0.11±0.03 0.16±0.02	0.45±0.008 0.49±0.03	0.55±0.3 1.82±0.16	2.35±0.12 2.66±0.13
100	75	0.19±0.08 0.40±0.05	1.07±0.01 1.22±0.07	1.47±0.03 4.5±0.4	5.3±0.4 6.65±0.34
150	75	0.12±0.049 0.26±0.031	0.715±0.01 0.816±0.044	1.54±0.29 3.00±0.27	4.15±0.95 4.43±0.23

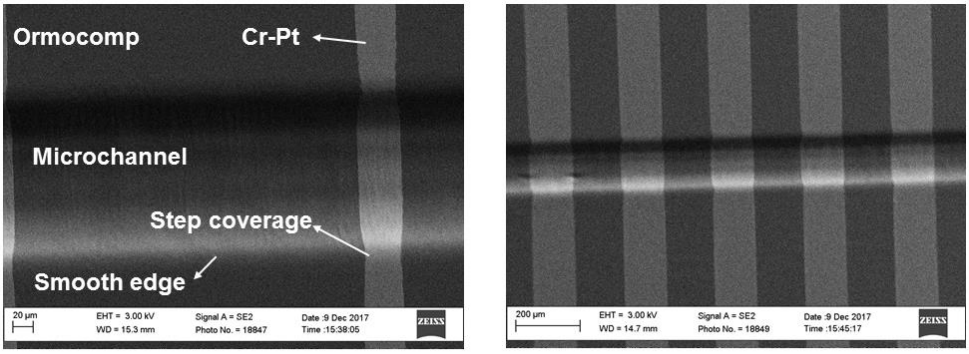

Figure 24. Step coverage of patterned Cr-Pt (220 nm) on microchannels featuring 150-μm width with smoothed edges and tapered sidewalls. A) 50-μm width wire. B) 150-μm width Cr-Pt wire (Publication III).

5.2.2 Metal adhesion

On the basis of the adhesion tests, all patterned metal survived in the ultrasound vibration, even without the adhesion layer under the main metal. However, only Ag exhibited strong adhesion without the adhesion promotion layer in the scotch tape pull-off test. Meanwhile, the other metals (Au, Al and Pt) necessitated the use of the adhesion layer. The thickness of all metals in the adhesion test was 30 nm, which was sufficient thickness for optical and non-electrical applications. In the electrochemical detection setup, the Al, Ag and Au metals quickly etched in borate buffer (20 mM, pH 10) after applying a voltage of (2000V, 5.5 cm) in the inlet and outlet of the microchip device. The main reason might be adhesion loss between the metal and Ormocomp owing to applying high voltage.

5.3 Surface modification

During the metallization processes, Ormocomp surface chemistry was altered after multiple processing steps and various etchants. Thus, contact goniometry was applied to characterize surface properties during the process. An advancing contact angle of 77°±12 and receding contact angle of 57°±10 were measured for the native Ormocomp. After the metal-etching process for all of the etchant, contact angles were around 0°. In spite of the low contact angles and high surface energy, the surface chemistry after metal etching was not suitable for bonding. The plasma treatment dropped in terms of advancing and receding contact angles to nearly 0°, meaning high surface energy is favored for the bonding process.

In addition to bonding, the surface chemistry played a crucial role in terms of cell adhesion. The native Ormocomp has been shown to support cell adhesion and the same was also confirmed by our own studies (with Huh-7 cells). For changing surface wettability for cell-repellent applications, hydrophobic polymers were deposited after forming porous Ormocomp via reactive ion etching. SEM imaging portrayed the difference between ordinary Ormocomp surfaces and porous surfaces (Fig. 25A, B). In addition, both contact angles (advancing and receding) over the deposited hydrophobic layer on top of the porous Ormocomp and native Ormocomp were measured for 45 days. The advancing contact angle was ≥110°and receding contact angle was ≥34°, which confirmed the stability of the hydrophobic surface properties. It should be noted that the measured data were remarkably constant during the entire period (Fig. 25C), which confirms the stability of the hydrophobic surface properties for a longer time.

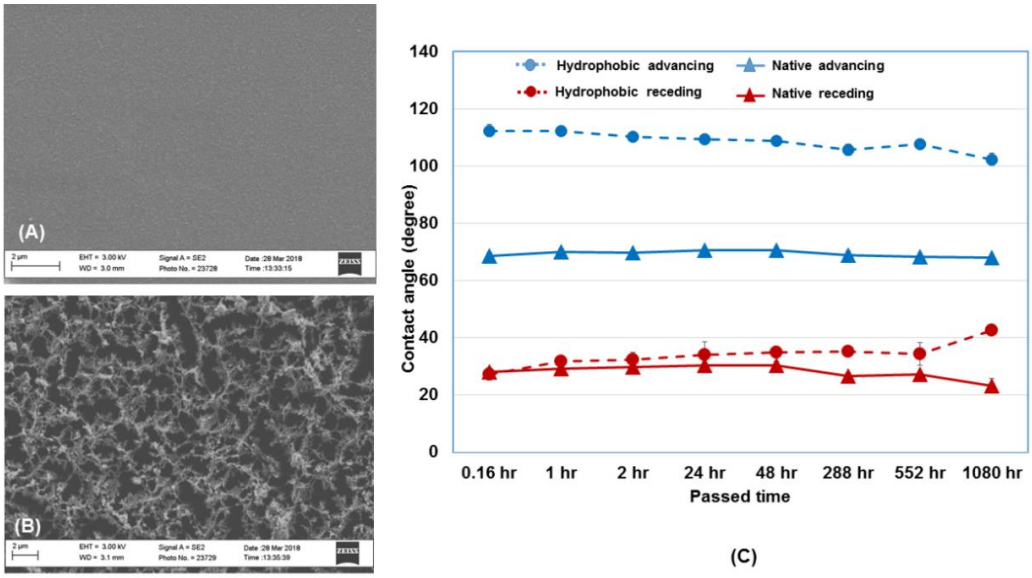

Figure 25. SEM image of Ormocomp A) Native surface B) Porous surface (after 20 min ion-reactive etching). C) Contact angle of native Ormocomp and hydrophobic area on top of the porous

surface for 45 days. The error bars represent the standard deviation from three replicate samples and three replicate determinations. (Publication IV)

5.4 Sealing of Ormocomp structures

In order to seal the microchannels, two bonding processes were developed. First, bonding over metal to implement sealing of Ormocomp structures with embedded metal elements was carried out. Second, a PDMS-bonding method was developed for cell-culturing devices.

5.4.1 Ormocomp to Ormocomp

It was observed that 30-nm thick metal was adequately thin to prevent creation of trapped air around patterned metal areas after bonding with Ormocomp layer. However, this thickness might not be sufficient for electrical applications based on discontinuity, i.e., poor step coverage across the microchannels.

In the case of Al metallization on top of the Ormocomp microchannel, the typical phosphoric acid-based Al etchant passivated the Ormocomp surface. Instead, it was seen that a basic-pH AZ 351 B developer could be a suitable etchant for Al with negligible impacts to the Ormocomp surface properties. However, non-uniform etching effects, such as scallop effects (Fig. 26A), may emerge when etching Al with Az 351 B developer. This was, however, eliminated by applying Cr as an adhesion layer under Al thin film (Fig. 25B). For the other metals, the scallop effect was not observed (Fig. 26C, D, E), even without an adhesion layer.

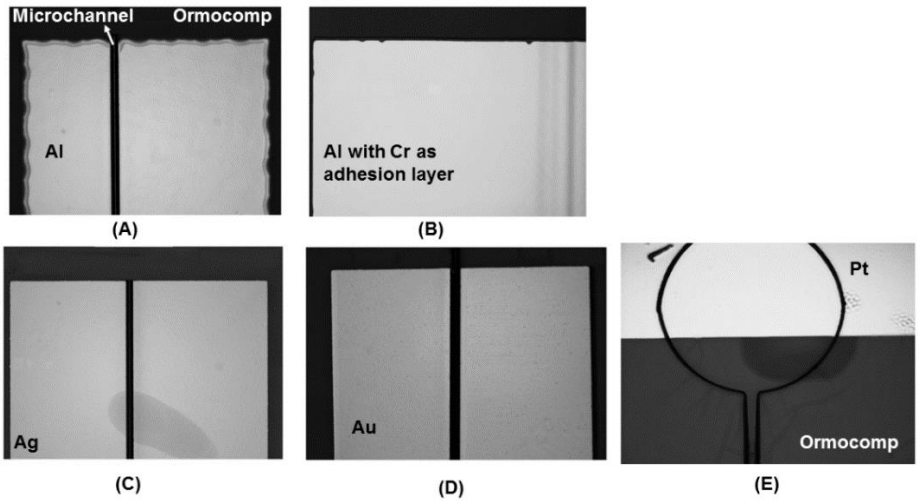

Figure 26. Microscope imagery. (A) Bare Al and (B) Cr-Al on top of an Ormocomp microchannel, specifically visualizing the non-uniform etching effect on the edge of bare Al etched via AZ351B. (C) Ag etched with standard Ag etchant, (D) Au and (E) Pt, which was etched with aqua regia (Publication III).

In the case of Ag, Au and Pt, passivation effects of metal etchants were documented, which required surface treatment prior to bonding. An oxygen plasma treatment was applied after wet etching. However, to avoid Ag oxidation during the plasma treatment, the photoresist used for the wet etching was left in place and only removed after oxygen plasma. In addition, it was determined that bonding required higher temperatures (95 ºC). Table 8 presents an overview of the optimized parameters for Ormocomp bonding after metallization. The bonding strength was tested by the scotch tape pull-off test in all cases and the samples were investigated under light microscope. By SEM imaging of the bonded cross-sections (Fig. 27), it was confirmed that after the scotch tape test, the microchannels were still enclosed within the upper layer of Ormocomp (Fig. 27).

Table 8. *Optimized parameters after metal etching process for bonding Ormocomp*

Metal (nm)	Etchant	Etching time	Oxygen plasma	Bonding Temp
Al (30)	Az 351B	30 min	No	25 °C
Cr (17)	Cr etchant	7-10 sec	Yes	25°C
Ti(5-10)	Ag etchant	1 min	Yes	95 °C
Ag (30)	Ag etchant	10 sec	Yes (with photoresist)	95 °C
Au (30)	Aqua regia (RT)	10 sec	Yes	95 °C
Pt (200)	Aqua Regia (55°C)	3-4 min	Yes	95 °C

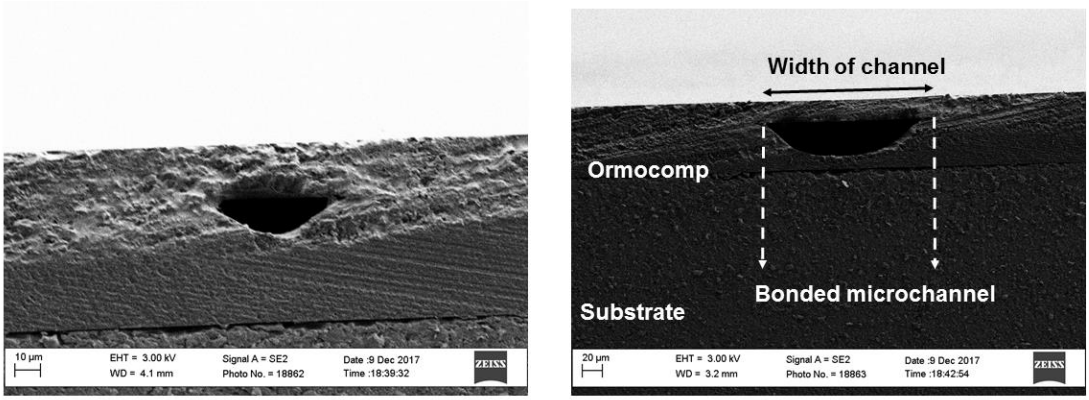

(A) **(B)**

Figure 27. Electrone micrograph cross-section of fully enclosed bonded metallized (Cr-Al 100 nm) microchannel (50 and 150 µm width) after scotch tape test A) 50 µm width B) 150 µm width. (Publication III).

5.4.2 PDMS to Ormocomp bonding

For cell culturing (Fig. 12, design III), high-aspect ratio structures were required to ensure proper exchange of oxygen and nutrients. In addition, high-

aspect ratio fluidic structures were necessary to facilitate harvesting of on-chip grown spheroids for further analysis. Thus, PDMS was the obvious material of choice for bonding. However, the cell cultures needed to be maintained for days (here, max 96 hr) without leakage, and, therefore, PMDS bonding had to be strong. To ensure strong bonding, semi-cured PDMS with high elastic properties (15:1 mixing ratio) and thickness of 5 mm was utilized. Owing to the risk of etching away the previously patterned hydrophobic layer, it was not possible to apply oxygen plasma to the Ormocomp surface, and it was only applied onto the PDMS surface. However, it was observed that oxygen plasma treatment (60 W) longer than 1 min can reduce bonding strength. After the bonding process, full curing was conducted in 80 °C temperature by pressing the PDMS cover against the Ormocomp substrate and applying a weight of 500-1000 g overnight. Afterwards, the bonding strength was tested manually by pulling the PDMS from the Ormocomp substrate and by flushing ethanol through the bonded device at a flow rate of 20 µl/min for 1-2 hrs followed by visual investigation of the bond. Bonded PDMS survived all tests.

5.5 Material biocompatibility

The biocompatibility of both the metallized and plasma-treated Ormocomp surfaces was assessed through monitoring the cell viability on such surface. Both Au (100 nm, electrode material) and Pt (100 nm, negative control material) electrodes were patterned on top of the planar Ormocomp surface. Next, Huh7 cells were seeded and grown under static conditions on top of patterned electrode areas for 96 hr and stained with appropriate dyes for live/dead cells and all nuclie. These in combination with the optical micrographs (cell morphology) did paint a decent picture of the biocompatibility and cell adhesion on the different surfaces. As expected, the cells did not attach on patterned Pt electrodes (data not shown), but Au featured excellent biocompatibility and supported cell adhesion and proliferation (Fig. 28). On Au, cell morphology was similar to conventional culture platforms.

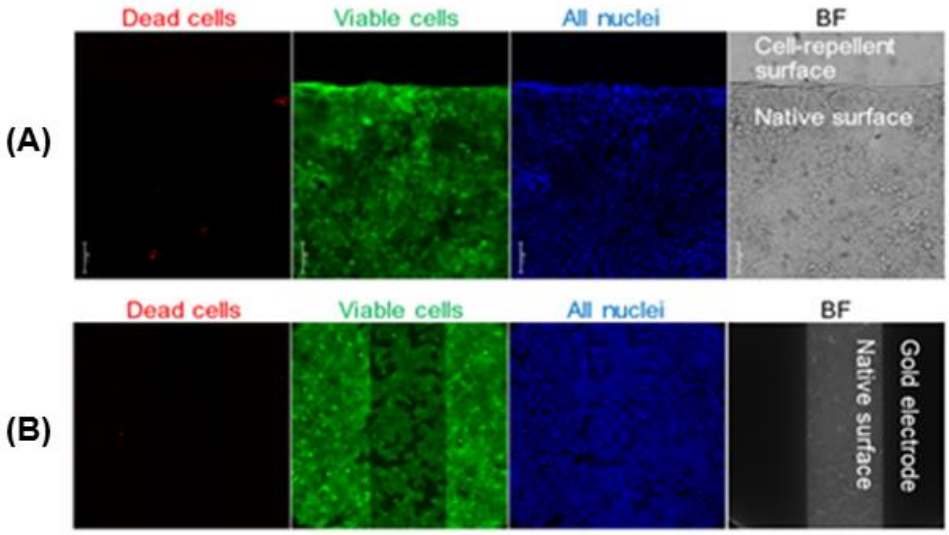

Figure 28. A) The impact of surface modification on the cell adhesion illustrating sharp edge of the cell monolayer culture between cell-repellent and native surfaces at 96 h. Cell-repellent: hydrophobic and porous. Native: hydrophilic and nonporous. B) Proper cell adherence on electrodes. Scale bars 100 µm. The cell stains used were Hoechst 33342 (blue, all nuclei), calcein AM (green, live cells) and PI (red, dead cells). (Publication IV).

The possibility to create Ormocomp surfaces cell-repellant was also studied by applying fluoropolymer coating (CF3 plasma) on top of native Ormocomp. In addition, the surface was made porous by oxygen plasma prior to fluoropolymer deposition, since porosification has been shown to promote hydrophobic properties [130]. In this manner clearly cell-repellant surfaces were achieved (Fig. 28). The feasibility of these surfaces for promoting cell aggregation and spheroid formation in concave microwells is described in the following chapter.

5.6 Cell and small-molecule monitoring

5.6.1 Cell Monitoring of 3D cell growth

Tunability of the Ormocomp residual layer allowed fabricating and controlling microwell shapes with UV exposure doses. Besides, the possibility of surface modification on Ormocomp (porous and hydrophobic layer) provided an excellent opportunity to change surface wettability for cellular applications. In this study, using single-step UV lithography, round cross-sectional profile microwell arrays with various diameters (150, 175 and 200 µm) were fabricated (Fig. 12, design III) and microwell surfaces and the surrounding areas were functionalized by growing hydrophobic polymers after local porous formation (Fig. 29A, B). Between microwell arrays, the native Ormocomp surface was obtained that were non-functionalized and Au (100 nm) electrodes

were integrated for impedance measuring of monolayer cell cultures in these places (Fig. 29 B). Finally, thick PDMS layers were bonded the device (Fig. 29C). Microwells with a functionalized surface were used for growing spheroid (Fig. 29D) with bright-field optical monitoring. Huh 7 cell lines were used in this study for 96 hr, enabling calculation of spheroid diameter during growth periods (Fig. 29E) to facilitate monitoring of cell growth. The results confirmed that we can control the size of the spheroid by the size of the microwell, as expected. In contrast, toxic effects of paclitaxel (anti-cancer drug) were analyzed by calculation of spheroid diameters, as well. After specific numbers of cells were trapped and gathered inside of each microwell, the unique shape of microwells (Fig. 29A) with the aid of a functionalized surface were made to form uniform spheroids (Fig. 29D) over time. It was important to keep cells in close proximity inside of wells to avoid trapping and growing. After growing of spheroids, they could collide with other spheroid in neighbor microwells, which was not preferable.

Meanwhile, cells were also grown on the native Ormocomp surface (Fig. 29F) in monolayer form (2D) and on top of the electrode (Fig. 29G), however cells did not adhere to the functionalized surface around the microwells array (Fig. 29F). It was observed that non-porous and hydrophilic areas (native Ormocomp) between Au electrodes, there were grown cells in a uniform monolayer (Fig. 29F, G). On the contrary, the porous-hydrophobic layer of microwells prevented adhering of cells to wells (Fig. 29F).

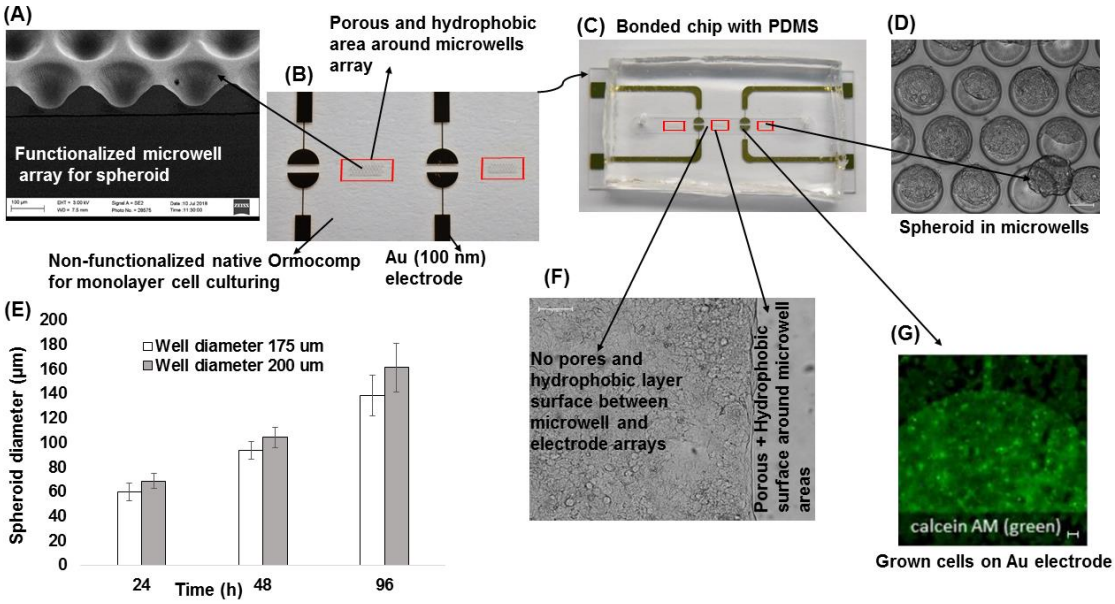

Figure 29. Monolayer (2D)-3D cell culturing concept. A) SEM image of 200-µm dimeter microwells. B) Au patterned electrode with microwells (porous and hydrophobic surface (red indicators). C) Microchip device for monolayer and 3D cell culturing in single microfluidic chip with porous and hydrophobic surface (red indicators). D) Grown 3D spheroid after 96 hr inside of functionalized surface of microwells. E) Spheroid grown diameter during 96 hr inside of microwells (175- and 200-µm diameter). F) Surface modification (porous and hydrophobic) enabled for non-

adherent surface for cells while they adhered to native Ormocomp surface (no porous or hydrophobic layer). G) Grown cells on Au electrode (2D) for impedance measurement. The error bars represent the standard deviation from three replicate samples and three replicate determinations. (Publication IV).

It was observed that cellular trapping efficiency in microwells was dependent on well diameter and population of cells. The experiments were carried out in 150-, 175- and 200-µm diameter wells with two different cell populations - 2.5 M cells/ml and 3.5 M cells/ml. Thus, 200-µm diameter wells captured the highest number of cells for both populations (Fig. 30A). Spheroid diameters were calculated through image-based software for 24, 48 and 96 hr durations of cell culturing, as mentioned earlier (Fig. 29E). Thereafter, paclitaxel, which had toxic effects, was used to show that the spheroids on our chips react to toxins in the expected manner, and therefore the use of such chips for drug screening has at least that evidence behind them. Paclitax was tested on monolayer cells and spheroids that caused dead cells in monolayer (2D) (Fig. 30B) and changed cellular topography (Fig. 30C). The combination of monolayer and 3D cell cultures within single Ormocomp microfluidic chips enabled fast screening and analysis of drug effects under flow conditions. There are no similar studies that have been completed with Ormocomp chips.

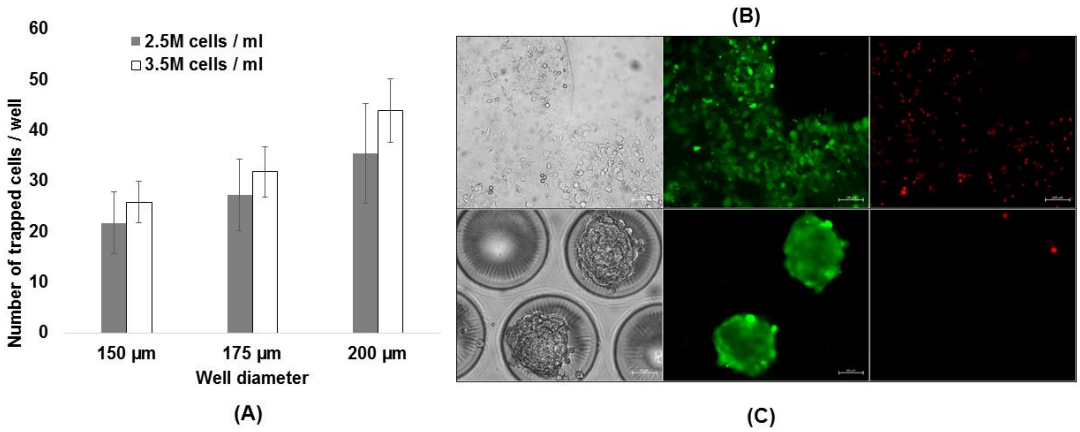

Figure 30. Dependency of cell trapping on microwell diameter and cell populations or paclitaxel effects on 2D and 3D cells. A) Cell trapping efficiency with three different microwell diameters (150, 175, 200 µm) with two categories of cell populations. B, C) Effects of 50 nM paclitaxel for 48 hr after growing up to 80% confluence monolayer and spheroid for 48 hr. Many dead cells were detected in the monolayer (B), but just a few in 3D were grown spheroids (C). Cells were stained with calcein AM (green, viable cells) and PI (red, dead cells). Scale bars 100 µm (top rows) and 50 µm (bottom row). The error bars represent the standard deviation from three replicate samples and three replicate determinations (Publication IV).

5.6.1.1 Monitoring of cell monolayers

Although optical monitoring is one of the most simple methods for monitoring cells, it has sensitivity limitations for monitoring proliferation in early stages. Labeled techniques, such as fluorescence-based detection, can improve sensitivity but they are invasive, which is not favorable in cellular studies. The combination of Ormocomp and biocompatible metal electrodes as a sensor could serve as an excellent opportunity for cell culturing (as monolayers) and monitoring non-invasively. The developed metallization and bonding techniques of Ormocomp-based microdevices not only allowed implementing the mirror element, but also integrating impedance electrodes as integral components of Ormocomp devices. In this study, Au (100 nm) electrodes were patterned on top of a 130-µm thick Ormocomp surface and bonded with a thick PDMS layer for Huh 7 culturing (Fig. 12, design III). Impedance electrodes therefore supplied complementary data on cell monolayer growth to support optical monitoring. It was recognized that impedance increased over time as the cells reached confluency, approaching a maximum at 16 kHz (Fig. 31A).

.

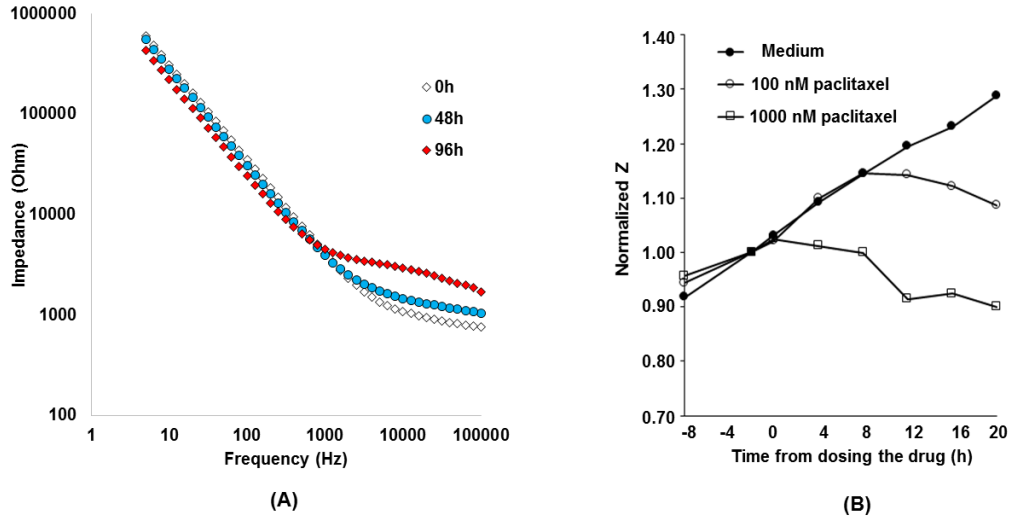

Figure 31. Impedance measurement of 2D cell culturing on Ormocomp with native surface. A) Impedance measurement for growing cells for 0, 48 and 96 hr. B) Disruption of the cell monolayer integrity (2D) observed with the on-chip impedance sensor. Signals were normalized to the value at 2 hr before dosing the drug. Baseline impedance values at time 0 hr (the time of dosing the drug) were 2108 Ω, 1366 Ω, and 1458 Ω for control (medium) or 100 nM and 1000 nM paclitaxel, respectively (Publication IV).

Impedance spectroscopy was also applied for monitoring the impact of paclitaxel on cell growth after 48 hr cell culturing. Paclitaxel (100 nM and 1000 nM) were introduced to the cell culture for 20 hr, which resulted in an obvious diminution in impedance signal (Fig. 31B). Morphology and viability of cells were dependent on dose of paclitaxel. It was demonstrated that the combination of native Ormocomp surface and Au electrodes provided

excellent possibilities for monitoring cell proliferation in cell monolayers via impedance spectroscopy measurements (Publication IV).

5.6.1.2 Single-cell detection

The feasibility of Ormocomp microdevices for single-cell monitoring was examined using microchannels featuring several different widths (round cross-sectional profiles) metallized with Al. (Fig. 12 I design B). After patterning Al on top of Ormocomp channels (nominal thickness 35 µm), the channels were covered by a thin layer of PDMS (Fig. 32 A).

The signal enhancement ratio was first determined using a 1 µM fluorescein solution. The fluorescence excitation beam was introduced to the channel using an epifluorescence microscope and the reflected beam (both excitation and emission) was concentrated with the concave shape of the Al micromirror prior to recording fluorescence. The signal enhancement obtained in this manner was roughly eight-fold higher compared with the signal recorded without mirrors (Fig. 32B, C). The maximum gain improvement was achieved when focal length of the concave micromirror was equal to the microchannel height as in 80-µm and 100-µm wide channels (Fig. 32D, E). By analyzing SEM images for 80-µm (Fig. 16F) and 100-µm (Fig. 15E) microchannels, it is possible to observe large concave areas that led to greater signal enhancement compared with other microchannel widths. Similar enhancement in fluorescence signal (eight-fold) was reached in a prior study, which used a combination of planar silver mirror elements under the flat bottom of a PDMS channel and polymer MLA (fabricated with a thermal reflow technique using positive photoresist AZ9260) [8]. The process described in this study is a more straightforward fabrication with similar results (eight-fold improvement). However, direct contact with sample solution could cause mirror metal corrosion and adhesion loss upon application of electrikinetic flows. Hence, embedded planar micromirrors were also fabricated to serve in contactless mode in the context of small molecule analysis (to be discussed in the next chapter).

Concave micromirrors can also be employed to obtain a magnified image of the cell and thus improve the spatial resolution of single-cell imaging. In this case, however, the single cell needs to be between the focal point (F) and center of radius (2F).

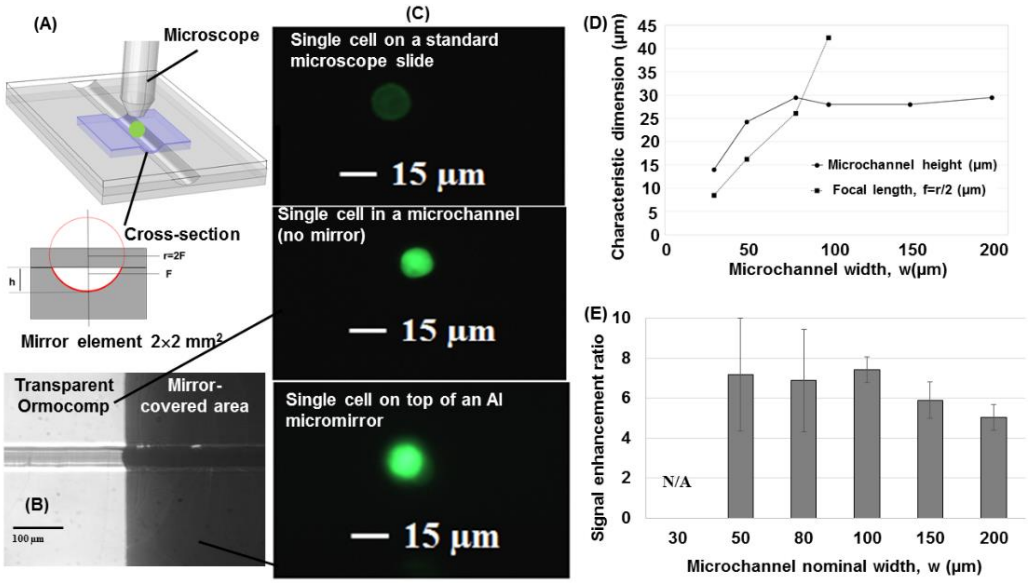

Figure 32. Concave micromirrors in various Ormocomp microchannel via epifluorescence microscopy for optical improvement of single cell. (A) Schematic view of the setup with concave mirror cross-sectional view. h=microchannel height, r=radius of curvature, and F=focal point. (B) 80-µm wide Ormocomp microchannel with mirror element on top of round cross-sectional profile, and non-mirror area (C) Comparison of the single cells' fluorescence under constant exposure conditions through the microscope slide, round cross-sectional Ormocomp channel (no mirror) and on top of the mirror element. (D) Microchannel height (h) as function of microchannel width and focal lengths (f) of micromirror (E) Signal enhancement ratios (for 1 lM fluorescein) with various microchannel widths. The nominal microchannel layer thickness was 35 µm, and UV exposure dose was 19 mJ/cm², and proximity gap was 400 µm. The error bars represent the standard deviation from three replicate samples and three replicate determinations. (Publication I).

5.6.2 Small-molecule monitoring

5.6.2.1 Microchip electrophoresis with fluorescence detection

The possibility of improving the fluorescence detection sensitivity of microchip electrophoresis with the assistance of micromirrors was also assessed by running a series of MCE-FL experiments with selected fluorescein derivatives in this study. Comparison of the signal enhancement ratio was based on the slopes of the calibration curves determined with and without the mirrors and by using both laser- and lamp-based fluorescence excitation sources. The results were compared to those with the concave mirrors.

The planar mirror setups (Fig. 12 I design A and C) were implemented under and top of bonded the microchannel respectively. In addition, the concave micromirrors (Fig. 12 I design B) were patterned on surface of round cross-sectional microchannel (similar to previous section (5.6.1.2)).

All mirror setup performances were characterized by determining the sensitivity gain ratios reached in a concentration dependent manner compared with bare Ormocomp microchannels.

First, fluorescein solutions (5 nM-5 μM in 20 mM borate buffer pH 10.0) filled into the microchannels (for concave and planar micromirror setups) seperately and the signals were recorded with the micromirrors and through the bare microchannel (next to the mirrors). For each micromirror setup the linear regression lines (y=ax+b) with slope of (a) were formed and compared with each other to quantify the sensitivity increase ratios obtained by micromirrors (Fig. 33A and B) according to equation:

$$\frac{a_{mirror}}{a_{no\ mirror}} = sensitivity\quad increase\quad ratio$$

where a_i is the slope of the linear regression line. It was obsereved that the highest sensitivity increase ratio (ca. 6-fold over bare microchannel) was obtained with the concave micromirror in comparsion with planar micromirrors (ca. 3-fold over bare microchannel). However, when patterned inside the microchannel (concave micromirror setup), the thin-film aluminum was easily etched away upon application of the high voltage (needed for electrophoretic separation). Therefore, the planar micromirror that was implemented under the bottom layer and was thus not in contact with the electrolyte solution was consideredthe better alternative for electrophoresis applications.

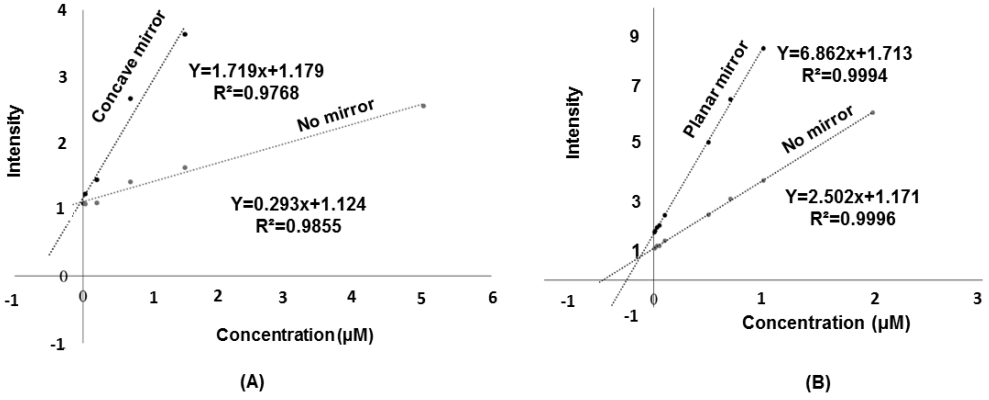

Figure 33. Calibration curves of (A) concave micromirror and (B) planar micromirror analyses performed with 488 nm lamp as excitation source.

The planar micromirrors' performances were also characterized by using both a laser-based and a broad-band lamp-based excitation sources, both in upright epifluorescence microscopy configuration, in UV (ex 355 nm) and visible (ex 488 nm) wavelength ranges. Calibration curves were determined to quantify sensitivity increase ratios ($a_{mirror}/a_{no\ mirror}$), by microchip electrophoresis in combination with fluorescence detection with the planar

micromirror and through the bare Ormocomp channel. Umbelliferone was used as the probe compounds in the UV range and fluorescein in the visible range. Calibration curves were established by averaging the signals from four repeated injections at each concentration. As expected, the sensitivity increase ratio ($a_{mirror}/a_{no\ mirror}$) in the visible range was ca. 3-fold and slightly less (ca. 2.5-fold) in the UV-range (Fig. 34 A). Similar result was obtained regardless of the excitation source type (laser vs. lamp) (Fig. 34 A). In terms of sensitivity increase, this translated into about 10 times lower detection limits (ca. 50 nM) compared with those obtained through the bare microchannel (ca. 500 nM) (Fig. 34B). Overall, it was concluded that instead of using relatively expensive LIF instrumentation, somewhat similar sensitivity increase in regular (lam-based) epifluorescence microscopy could be achieved by implementing on-chip thin-film aluminum micromirrors as integral part of the microdevice.

In addition to upright microscopy, another micromirror configuration was developed for inverted epiflurescence microscopy. In this experiment, the planar aluminum mirror (Fig. 12 I design C) was patterned on top of the bonded cover layer and excitation light was brought in from below the chip. Due to concave shape of microchannel, the light beam was seemingly collimated at the water-Ormocomp interface, which resulted in as good as ca. 8-fold sensitivity increase ratio ($a_{mirror}/a_{no\ mirror}$) (Fig. 34C). Considering the straightforward fabrication process, this setup was concluded most cost-efficient out of the three tested configurations.

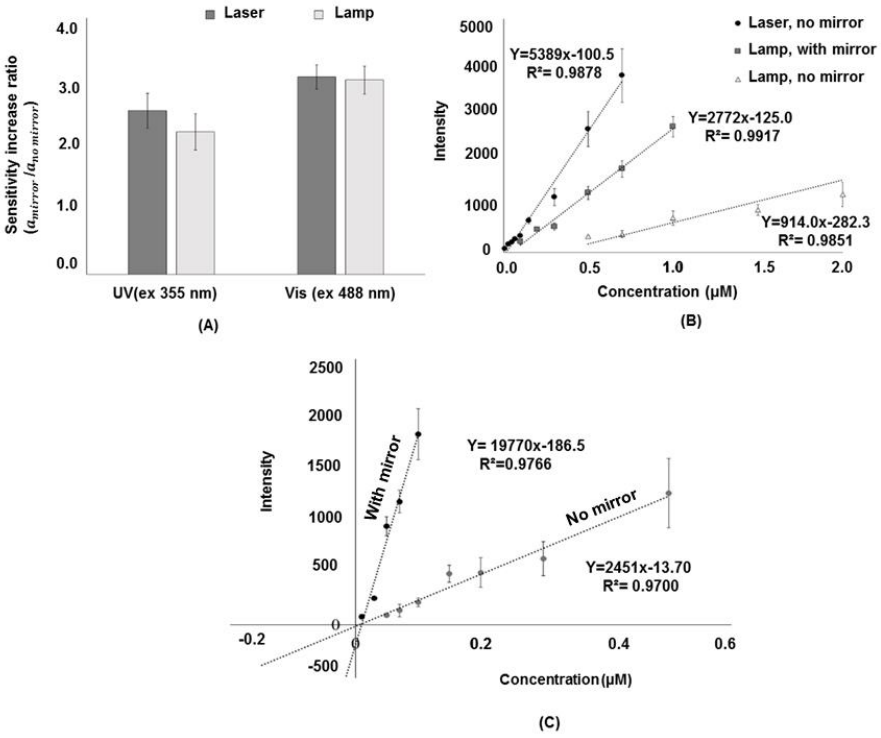

Figure 34. (A) Sensitivity increase ratios ($a_{mirror}/a_{no\ mirror}$) measured by both laser and broad-band lamp excitations in UV and visible ranges (B) Calibration curves of microchip electrophoresis analyses with mirror under microchannel (B design chip) with laser and lamp (C) Calibration curves

of microchip electrophoresis analysis with mirror on top of covered channel (C design chips) with and without mirror. The error bars represent the standard deviation from three replicate samples and three replicate determinations

5.6.2.2 Microchip electrophoresis with electrochemical detection

Electrochemical detection of small molecules is needed in parallel with fluorescence detection. However, most compounds are not inherently fluorescent. Electrochemical detection is more universal and leverages miniaturization. Advanced metallization (metal adhesion, step coverage) and bonding techniques, carried out in this study on Ormocomp, allowed us to integrate Cr-Pt (17-200 nm) (Fig.35 A) electrochemical detection sensors into Ormocomp microfluidic channels (150 µm width × 35 µm height) and its sealing with another layer of Ormocomp (Fig. 12, design II) to examine robustness of the developed metallization techniques. Amperometric detection of acetaminophen (20 µM in 20mM 2-(N-Morpholino)ethanesulfonic acid (MES) hydrate, pH 6.5, including 0.2% ethanol) was carried out by applying 0.8 V to the working electrode. The analysis is shown in Figure 36B. It is observed that migration times and peak areas were 29.8±0.7 sec (RSD of 2%,) and 15.6±2.8 sec (RSD of 18%), respectively. This indicates that the surface chemistry is uniform as it provides stable electroosmotic flow. The experiment was repeated five times, which results in the same peak area (Fig. 35B). This suggests acceptable performance and stable developed metal electrodes (Publication III).

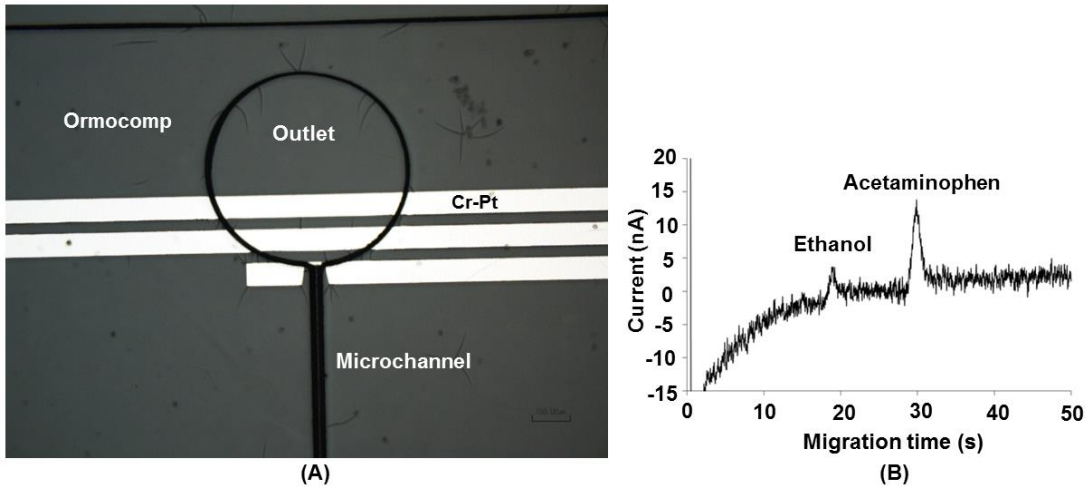

Figure 35. Proof of amperometric detection concept for Cr-Pt electrodes on Ormocomp microchannels. A) Micrograph of Cr-Pt-based electrode in outlet of microcapillary electrochemical detection chip. B) Analysis of 20 µM acetaminophen response under 0.8 V potential for working electrode (Publication III).

6 SUMMARY AND CONCLUSIONS

The inherent biocompatibility, robust mechanical and thermal stability, high optical transparency and possibility for surface functionalization via physico-chemical surface treatments have been shown herein for ORMOCERs, rendering them an attractive material for Bio-MEMS devices. In this study, ORMOCER microfabrication and metallization techniques were developed for a commercial ORMOCER formulation, Ormocomp.

The unique behaviour of the Ormocomp residual layer under UV exposure enabled us to fabricate and tune round cross-sectionally shaped microstructures via single-step UV lithography. It was demonstrated that the curvature of the round cross-sectional profile could be regulated by the UV exposure dose, the distance of the proximity gap and the nominal thickness of the spin-coated Ormocomp layer so as to achieve round cross-sectional microchannels and microwells. However, it was observed there are limitations with smaller-sized microstructures, which are easily filled by the residual layer. Moreover, new metallization processes were developed for integration of optical and electrical-sensing elements into Ormocomp microfluidic channels for the first time. Strong metal adhesion was proven in this study by performing adhesion testing. The tapered sidewalls and rounded edges of the round cross-sectional microchannels bestowed substantial improvement to step coverage of the metal film, which is difficult to produce with other materials as seen in previous works. In addition, various bonding scenarios applicable after metal wet-etching were formulated to be able to seal the metallized microstructures.

Although the unique shape (concave profile) provided substantial optical signal enhancement with implementation of thin-film reflective metal as the mirror element, signal enhancement was limited to approximately an order of magnitude (eight-fold) improvement, which was similar to enhancement with planar embedded micromirrors. The electrochemical sensor electrodes implemented into an enclosed Ormocomp microfluidic channel facilitated detection of electroactive small molecules, as demonstrated with amperometric detection of acetaminophen. In addition, impedance electrodes implemented at the bottom of the Ormocomp channel were shown to allow monitoring of the cell monolayer (viability) over time.

In addition to on-chip sensing of cells and small molecules, selective functionalization of the Ormocomp surface, supported by surface topography, enabled parallel culturing of 2D cell monolayers (native, hydrophilic and planar surface) and creation of 3D cell spheroids (hydrophobic and porous microwells). The developed organ-on-a-chip platform permitted screening of the toxic drug effects simultaneously with both 2D and 3D models. Optical

monitoring of 3D cells during early stages could be difficult but it is possible to implement impedance electrodes on microwells' tapered walls that afford electrical monitoring of 3D cells inside of microwells, even during early stages. On the other hand, the platform created is not able to monitor 3D cells based on impedance, thereby necessitating further study surrounding implementing electrical sensors on sidewalls of microwells for 3D cell impedance measurement.

Despite the several advantages offered by Ormocomp microfabrication, there are still certain recognized limitations. For one, Ormocomp chemistry was not stable at temperatures higher than 270 °C. Further, a large number of cracks were observed on the Ormocomp and patterned metal layer. Additionally, the safety margin for temperature was approximately 270 °C. Thus, Ormocomp may not be suitable for, e.g., CVD-based thin film deposition techniques or annealing processes.

Moreover, the chemistry of Ormocomp was not readily compatible with strong acid etchants, like hydrofluoric acid and warm aqua regia (70 °C temperature) or acetone. Substantial adhesion loss was observed in both cases. Therefore, it was challenging for lift-off process based on loss of adhesion between Ormocomp and glass substrate by acetone and mr-Rem 400. In addition, the surface chemistry of Ormococmp was altered by most of the metal wet etchants, which complicated bonding and necessitated the development of case-specific protocols to allow for proper sealing of metallized microstructures. For almost all metals (other than Al), surface refreshment was required to bolster bonding. Electrochemical etching of metals also took place in many buffer solutions used in microfluidic separations, which may complicate wider use of metallized Ormocomp devices in electrochemical experiments. Thus, there is the requirement of further development of metal adhesion for high-voltage applications.

In addition, Ormocomp was very sensitive to UV exposure. With the smallest change in UV dose or proximity gap, or thickness of Ormococmp, the residual layer may behave very differently. Although in this work, the high UV sensitivity was turned into an advantage through controlled overexposure to yield tunable round cross-sectional shapes, precise control over this process requires case-specific method development. Ormococmp layer thickness is another limitation at the wafer scale. In particular, Ormocomp layers thicker than 150 µm had non-uniform edges that were similar to edge-bead effects associated with thick SU-8 layers. Furthermore, based on film stress of the thick Ormocomp layer, wafer edges were deflected during the thermal process.

All in all, Ormocomp has very competitive properties for Bio-MEMS comparesd to silicon, glass and SU-8 when processability, tunability, surface properties etc. are all taken into account. And what has been lacking has been fabrication processes to take advantage of these properties, and this thesis now provides those fabrication processes.

References

[1] D. L. Polla, "BioMEMS applications in medicine," in *International Symposium on Micromechatronics and Human sience*, Nagoya, Japan, 2001.

[2] K. Menon, R. A. Joy, N. Sood and R. Mittal, "The Applications of BioMEMS in Diagnosis, Cell Biology, and Therapy: A Review," *BioNanoScience*, vol. 3, pp. 356-366, 2013.

[3] X.-M. Zhao, Y. Xia and G. M. Whitesides, "Soft lithographic methods for nano-fabrication," *Materials Chemistry*, vol. 7, pp. 1069-1074, 1997.

[4] S. S. Saliterman, Fundamentals of Bio-MEMS and medical devices, Belingham, Washington: SPIE Press, 2006.

[5] Y. Xia and G. M. Whitesides, "Soft Lithography," *Annual Review of Materials Science*, vol. 28, pp. 153-184, 1998.

[6] V. N. Vernekar, D. K. Cullen, N. Fogleman, Y. Choi, A. J. Garcıa, M. G. Allen, G. J. Brewer and M. C. LaPlaca, "SU-8 2000 rendered cytocompatible for neuronal bioMEMS applications," *Biomedical Material Research*, vol. 89A, pp. 138-151, 2009.

[7] P. Müller, D. Kopp, A. Llobera and H. Zappe, "Optofluidic router based on tunable liquid–liquid mirrors," *Lab on a Chip*, vol. 14, pp. 737-743, 2014.

[8] J. Lim, P. Gruner, M. Konrad and J.-C. Baret, "Micro-optical lens array for fluorescence detection in droplet-based microfluidics," *Lab on a Chip*, vol. 13, pp. 1472-1475, 2013.

[9] B. Weigl, R. Bardell and C. Cabrera, "Lab-on-a-chip for drug development," *Advanced Drug Delivery Reviews*, vol. 55, pp. 349-377, 2003.

[10] H. Andersson and A. v. d. Berg, "Microfluidic devices for cellomics: a review," *Sensor and Actuators B: Chem*, vol. 92, pp. 315-325, 2003.

[11] T. Sikanen, S. Aura, S. Franssila, T. Kotiaho and R. Kostiainen, "Microchip capillary electrophoresis-electrospray ionization-mass spectrometry of intact proteins using uncoated Ormocomp microchips," *Analytica Chimica Acta*, vol. 711, pp. 69-76, 2012.

[12] J. Hong, K. Kandasamy, M. Marimuthu, C. S. Choic and S. Kim, "Electrical cell-substrate impedance sensing as a non-invasive tool for cancer cell study," *Analyst*, vol. 136, pp. 237-245, 2011.

[13] F.Heer, W.Franks, A.Blau, S.Taschini, C.Ziegler and A. Baltes, "CMOS microelectrode array for the monitoring of electrogenic cells," *Biosensors and Bioelectronics,* vol. 20, pp. 358-366, 2004.

[14] H. Trieu, G. Blume, L. v. Mirbach-Wahn, D. V. Rojas, K. Kalaydzhyan, R. Pörtner, N. Meyne, A. Jacob and M. Jücker, "BioMEMS for sensing in cell characterization,drug screening and biofilm detection," in *AMA Conferences 2017 – SENSOR 2017 and IRS2 2017*, Nürnberg, Germany, 2017.

[15] A. Tourovskaia, X. Figueroa-Masot and A. Folch, "Differentiation-on-a-chip: A microfluidic platform for long-term cell culture studies," *Lab on a Chip,* vol. 5, pp. 14-19, 2005.

[16] S.-M. Lee, N. Han, R. Lee, I.-H. Choi, Y.-B. Park, Jeon-SooShin and K.-H. Yooa, "Real-time monitoring of 3D cell culture using a 3D capacitance biosensor," *Biosensors and Bioelectronics,* vol. 77, pp. 56-61, 2016.

[17] S. Franssila, Introduction to Microfabrication, 2nd ed., West Sussex: John Wiley & Sons Ltd, 2010.

[18] O. Rötting, W. Röpke, H. Becker and C.Gärtner, "Polymer microfabrication technologies," *Microsystem Technologies,* vol. 8, pp. 32-36, 2002.

[19] M. J. Madou, Fundamentals of Microfabrication: The Science of Miniaturization, Second Edition, Boca Raton: CRC Press, 2002.

[20] B. F. E. Matarèse, P. L. C. Feyen, A. Falco, F. Benfenati, P. Lugli and J. C. d. Mello, "Use of SU8 as a stable and biocompatible adhesion layer for gold bioelectrodes," *Sientific Reports,* vol. 8, pp. 5560-5572, 2018.

[21] L. Amato, S. S.Keller, A. Heiskanen, M. Dimaki, J. Emnéus, A. Boisen and M. Tenje, "Fabrication of high-aspect ratio SU-8 micropillar arrays," *Microelectronic Engineering,* vol. 98, pp. 483-487, 2012.

[22] K. V. Nemani, K. L. Moodie, J. B. Brennick, A. Su and B. Gimi, "In vitro and in vivo evaluation of SU-8 biocompatibility," *Materials Science and Engineering: C,* vol. 3, pp. 4453-4459, 2013.

[23] G. Hong, A. S. Holmes and M. E. Heaton, "SU8 resist plasma etching and its optimisation," *Microsystem Technologies,* vol. 10, pp. 357-359, 2004.

[24] E. Koukharenko, M. Kraft, G. J. Ensell and N. Hollinshead, "A comparative study of different thick photoresists for MEMS applications," *Materials in Electronics,* vol. 16, pp. 741-747, 2005.

[25] D. C. Duffy, J. C. M. Donald, O. J. A. Schueller and G. M. Whitesides, "Rapid Prototyping of Microfluidic Systems in Poly(dimethylsiloxane)," *Analytical Chemistry,* vol. 70, pp. 4974-4984, 1998.

[26] M. W. Toepke and D. J. Beebe, "PDMS absorption of small molecules and consequences in microfluidic applications," *Lab on a Chip,* vol. 6, pp. 1484-1486, 2006.

[27] Y. Zhang, M. Ishida, Y. Kazoe, Y. Sato and N. Miki, "Water-vapor permeability control of PDMS by the dispersion of collagen powder," *Transactions on Electrical and Electronic Engineering* , vol. 4, pp. 442-449, 2009.

[28] A. Kurian, S. Prasad and A. Dhinojwala, "Unusual Surface Aging of Poly(dimethylsiloxane) Elastomers," *Macromolecules,* vol. 43, pp. 2438-2443, 2010.

[29] S. Huang, H. Qiaohong, H. Xianqiao and H. Chen, "Fabrication of micro pneumatic valves with double-layer elastic poly(dimethylsiloxane) membranes in rigid poly(methyl methacrylate) microfluidic chips," *Micromachines and Microengineer,* vol. 22, p. 085008, 2012.

[30] M. Vinci, S. Gowan, F. Boxall, L. Patterson, M. Zimmermann, W. Court, C. Lomas, M. Mendiola, D. Hardisson and S. A. Eccles, "Advances in establishment and analysis of three-dimensional tumor spheroid-based functional assays for target validation and drug evaluation," *BMC Biology,* vol. 10, pp. 1-21, 2012.

[31] Y. Y. Choia, B. G. Chung, D. H. Lee, A. Khademhosseini, J.-H. Kime and S.-H. Lee, "Controlled-size embryoid body formation in concave microwell arrays," *Biomaterial,* vol. 31, pp. 4296-4303, 2010.

[32] G. S. Jeong, J. H. Song, A. R. Kang, Y. Jun, J. H. Kim, J. Y. Chang ja S.-H. Lee, ”Surface Tension-Mediated, Concave-Microwell Arrays for Large-Scale, Simultaneous Production of Homogeneously Sized Embryoid Bodies,” *Advance Health Care Material,* osa/vuosik. 2, pp. 119-125, 2012.

[33] J. Zhang, M. B. Chan-Park and S. R. Conner, "Effect of exposure dose on the replication fidelity and profile of very high aspect ratio microchannels in SU-8," *Lab on a Chip,* vol. 4, pp. 646-653, 2004.

[34] Y. Bao, F. Zhou, T. W. LeBrun and J. J.Gorman, "Concave silicon micromirrors for stable hemispherical optical microcavities," *Optical Express,* vol. 25, pp. 15493-15503, 2017.

[35] Y. S. Ow, M. B. H. Breese and S. Azimi, "Fabrication of concave silicon micro-mirrors," *Optical Express,* vol. 18, pp. 14511-14518, 2010.

[36] Y. Xu, F. Xie, T. Qiu, L. Xie, W. Xing and J. Cheng, "Rapid fabrication of a microdevice with concave microwells and its application in embryoid body formation," *Biomicrofluidics,* vol. 6, pp. 1-11, 2012.

[37] M. Abdelgawad, C. Wu, W.-Y. Chien, W. R. Geddie and M. A. S. Jewettbe, "A fast and simple method to fabricate circular microchannels in polydimethylsiloxane (PDMS)," *Lab on a Chip,* vol. 11, pp. 545-551, 2011.

[38] G.-J. Wang, K.-H. Ho, S.-h. Hsu and K.-P. Wang, "Microvessel scaffold with circular microchannels by photoresist melting," *Biomedical Microdevices,* vol. 9, pp. 657-663, 2007.

[39] J. S. Choi, Y. Piao and T. S. Seo, "Fabrication of a circular PDMS microchannel for constructing a three-dimensional endothelial cell layer," *Bioprocess and Biosystems Engineering,* vol. 36, pp. 1871-1878, 2013.

[40] G.-J. Wang, C.-C. Hsueh and S.-h. Hsu, "Fabrication of PLGA microvessel scaffolds with circular microchannels using soft lithography," *Micromechine and Microengineering,* vol. 17, pp. 2000-2005, 2007.

[41] L. Seung-A, N. D. Yoon, K. Edward, J. Jongil, K. Dong-Sik and L. Sang-Hoon, "Spheroid-based three-dimensional liver-on-a-chip to investigate hepatocyte–hepatic stellate cell interactions and flow effects," *Lab on a Chip,* vol. 13, pp. 3435-3766, 2013.

[42] Y. Wang, C. N. Phillips, G. S. Herrera, C. E. Sims, J. J. Yeh and N. L. Allbritton, "Array of biodegradable microrafts for isolation and implantation of living, adherent cells," *RSC Advances,* vol. 3, pp. 9264-9272, 2013.

[43] G. Ut-Binh, D. Lee and D. M. R. King, "Microfabrication of cavities in polydimethylsiloxane using DRIE silicon molds," *Lab on a Chip,* vol. 7, pp. 1660-1662, 2007.

[44] B. Bin, J. Jieke, L. Fengyu, Z. Pengchao, C. Shuoran, Y. Qiang, W. Shutao, S. Bin, J. Lei and S. Yanlin, "Fabrication of Patterned Concave Microstructures by Inkjet Imprinting," *Advance Functional Material,* vol. 25, pp. 3286-3294, 2015.

[45] H. Yu and G. Zhou, "Deformable mold based on-demand microchannel fabrication technology," *Sensors and Actuators B: Chemical,* vol. 183, pp. 40-45, 2013.

[46] H. C. M. Benjamin, N. S. Huan, L. K. H. Holden and Y. Yong-Jin, "3D printed microfluidics for biological applications," *Lab on a Chip,* vol. 15, pp. 3627-3637, 2015.

[47] G. Bethany, E. Jayda, L. Sarah, C. Chen and S. Dana, "Evaluation of 3D Printing and Its Potential Impact on Biotechnology and the Chemical Sciences," *Analytical Chemistry,* vol. 86, pp. 3240-3253, 2014.

[48] R. Walczak and K. Adamski, "Inkjet 3D printing of microfluidic structures on the selection of the printer towards printing your own microfluidic chips," *Micromechine and Microengineering,* vol. 25, p. 085013 (11pp), 2015.

[49] D. H. Kam and J. Mazumder, "Three-dimensional biomimetic microchannel network by laser direct writing," *Laser Applications,* vol. 20, pp. 1-9, 2008.

[50] D. Nieto, T. Delgado and M. T. Flores-Arias, "Fabrication of microchannels on soda-lime glass substrates with a Nd:YVO4 laser," *Optics and Lasers in Engineering,* vol. 63, pp. 11-18, 2014.

[51] M. O. Abdelgawad and A. R. Wheeler, "Rapid Prototyping in Copper Substrates for Digital Microfluidics," *Advanced Materials,* vol. 19, pp. 133-137, 2006.

[52] L. J. Hyun, K. H. Nam, S. J. Hyun and M. Jay, "Reflection characteristics of a copper metal-organic chemical-vapor-deposited thin film for vertical micromirror applications," *Optics Letters,* vol. 27, pp. 728-730, 2002.

[53] H. Xie, "Package and integration of micro scanning mirror," in *MEMS Mirrors*, Basel, Micromachine, 2008, p. 84.

[54] W. Jinbo, C. Wenbin, W. Weijia and C. D. Choy, "Polydimethylsiloxane microfluidic chip with integrated microheater and thermal sensor," *Biomicrofluidics,* vol. 3, pp. 012005-7, 2009.

[55] N.-C. Chen, C.-H. Chen, M.-K. Chen, L.-S. Jang and M.-H. Wang, "Single-cell trapping and impedance measurement utilizing dielectrophoresis in a parallel-plate microfluidic device," *Sensors and Actuators B: Chemical,* vol. 190, pp. 570-577, 2014.

[56] K. Cheung, S. Gawad and P. Renaud, "Impedance spectroscopy flow cytometry: On-chip label-free cell differentiation," *Cytometry Part A,* vol. 65A, pp. 124-132, 2005.

[57] T. D. Chung and H. C. Kim, "Cytometry and Velocimetry on a Microfluidic Chip Using Polyelectrolytic Salt Bridges," *Analytical Chemistry*, vol. 77, pp. 2490-2495, 2005.

[58] O. Pänke, W. Weigel, S. Schmidt, A. Steude and A. A.Robitzki, "A cell-based impedance assay for monitoring transient receptor potential (TRP) ion channel activity," *Biosensors and Bioelectronics,* vol. 26, pp. 2376-2382, 2011.

[59] L. Nyholm, "Electrochemical techniques for lab-on-a-chip applications," *Analyst*, vol. 130, pp. 599-605, 2005.

[60] J. Daniels and N. Pourmand, "Label-Free Impedance Biosensors: Opportunities and Challenges," *Electroanalysis*, vol. 19, pp. 1239-1257, 2007.

[61] K. Swinney and D. J. Bornhop, "Detection in capillary electrophoresis," *Electrophoresis,* vol. 21, no. 7, pp. 1239-1250, 2000.

[62] D. P. Manica, Y. Mitsumori and A. G. Ewing, "Characterization of Electrode Fouling and Surface Regeneration for a Platinum Electrode on an Electrophoresis Microchip," *Analytical Chemistry,* vol. 75, pp. 4572-4577, 2003.

[63] T. Smy, S. Dew and R. Joshi, "Modeling 3D effects of substrate topography on step coverage and film morphology of thin metal films," *Thin Solid Films,* vol. 415, pp. 32-45, 2002.

[64] S. Gawad and L. S. a. P. Renaud, "Micromachined impedance spectroscopy flow cytometer for cell analysis and particle sizing," *Lab on a Chip,* vol. 1, pp. 76-82, 2001.

[65] J. Wang, C. Wu, N. Hu, J. Zhou and L. D. a. P. Wang, "Microfabricated Electrochemical Cell-Based Biosensors for Analysis of Living Cells In Vitro," *Biosensors,* vol. 2, pp. 127-170, 2012.

[66] A. Manz, D. Harrison, E. M.J.Verpoorte, James.C.Fettinger, A. Paulus, H. Lüdi and H. Widmer, "Planar chips technology for miniaturization and integration of separation techniques into monitoring systems: Capillary electrophoresis on a chip," *Journal of Chromatography A,* vol. 593, pp. 253-258, 1992.

[67] J. N. Patel, B. Kaminska, B. L. Gray and B. D. Gates, "A sacrificial SU-8 mask for direct metallization on PDMS," *Micromechanics and Microengineering,* vol. 19, p. 115014 (10pp), 2009.

[68] N. Bowden, S. Brittain, A. G. Evans, J. W. Hutchinson and G. M. Whitesides, "Spontaneous formation of ordered structures in thin films of metals supported on an elastomeric polymer," *Letters to Nature,* vol. 393, pp. 146-149, 1998.

[69] A. Delcorte, S. Befahy, C. Poleunis, M. Troosters and P. Bertrand, "Improvement of metal adhesion to silicone films: a ToF-SIMS study," *Adhesion Aspects of Thin Films,* vol. 2, pp. 1-12, 2004.

[70] D. Hilbich, "A new, low-cost, PDMS metallization process for highly conductive flexible and stretchable electronics," Simon Freaser University, Vancouver, 2010.

[71] A. Ryspayeva, T. D.A.Jones, M. N. Esfahani, M. P.Shuttleworth, R. A.Harris, R. W. Marc, P.Y.Desmulliez and J. Marques-Hueso, "A rapid technique for the direct metallization of PDMS substrates for flexible and stretchable electronics applications," *Microelectronic Engineering,* vol. 209, pp. 35-40, 2019.

[72] S. C. Kilchenmann, E. Rollo, P. Maoddi and C. Guiducci, "Metal-Coated SU-8 Structures for High-Density 3-D Microelectrode Arrays," *Microelechtromechanical Systems,* vol. 25, pp. 425-431, 2006.

[73] B. Moazzez, S. M. O'Brien and E. F. Merschrod, "Improved Adhesion of Gold Thin Films Evaporated on Polymer Resin: Applications for Sensing Surfaces and MEMS," *Sensors,* vol. 13, pp. 7021-7032, 2013.

[74] J. A. v. Kan, I. Rajta, K. Ansari, A. A. Bettiol and F. Watt, "Nickel and copper electroplating of proton beam micromachined SU-8 resist," *Microsystem Technologies,* vol. 8, pp. 383-386, 2002.

[75] S. Keller, G. Blagoi, M. Lillemose and D. Haefliger, "Processing of thin SU-8 films," *Micromech.ine and Microengineer,* vol. 18, p. 125020 (10pp), 2008.

[76] S.Bystrova, R.Luttge and A. d. Berg, "Study of crack formation in high-aspect ratio SU-8 structures on silicon," *Microelectronic Engineering,* vol. 84, pp. 1113-1116, 2007.

[77] B. Wolf, M. B. wein, W. Baumann, R. Ehret and M. Kraus, "Monitoring of cellular signalling and metabolism with modular sensor-technique: The PhysioControl-Microsystem (PCM®)," *Biosensors and Bioelectronics,* vol. 13, pp. 501-509, 1998.

[78] T. A. Nguyen, T.-I. Yin, D. Reyes and G. A.Urban, "Microfluidic Chip with Integrated Electrical Cell-Impedance Sensing for Monitoring Single Cancer Cell Migration in Three-Dimensional Matrixes," *Analytical Chemistry,* vol. 85, pp. 11068-11076, 2013.

[79] H. Morgan, T. Sun, D. Holmes, S. Gawad and N. G. Green, "Single cell dielectric spectroscopy," *Physics D: Applied Physics,* vol. 40, pp. 61-70, 2006.

[80] I. Giaever and C. R. Keese, "Micromotion of mammalian cells measured electrically," *PNAS,* vol. 88, pp. 7896-7900, 1991.

[81] D. Krinke, H.-G. Jahnke, O. Pänke and A. A. Robitzki, "A microelectrode-based sensor for label-free in vitro detection of ischemic effects on cardiomyocytes," *Biosensors and Bioelectronics,* vol. 24, pp. 2798-2803, 2009.

[82] C. Rümenapp, M. Remm, B. Wolf and B. Gleich, "Improved method for impedance measurements of mammalian cells," *Biosensors and Bioelectronics,* vol. 24, pp. 2915-2919, 2009.

[83] S. Cho and H. Thielecke, "Electrical characterization of human mesenchymal stem cell growth on microelectrode," *Microelectronic Engineering,* vol. 85, pp. 1272-1274, 2008.

[84] S. Arndt, J. Seebach, K. Psathaki, H.-J. Galla and J. Wegener, "Bioelectrical impedance assay to monitor changes in cell shape during apoptosis," *Biosensors and Bioelectronics,* vol. 19, pp. 583-594, 2004.

[85] L. Wang, L. Wang, H. y. Yin, W. l. Xing, Z. y. Yu and M. G. J. Cheng, "Real-time, label-free monitoring of the cell cycle with a cellular impedance sensing chip," *Biosensors and Bioelectronics,* vol. 25, p. 990–995, 2010.

[86] M. Grossi and B. Riccò, "Electrical impedance spectroscopy (EIS) for biological analysis and food characterization: a review," *Journal of Sensors and Sensor Systems,* vol. 6, pp. 303-325, 2017.

[87] K. Benson, S. Cramer and H.-J. Galla, "Impedance-based cell monitoring: Barrier properties and beyond," *Fluids and Barriers of the CNS,* vol. 10, pp. 1-11, 2013.

[88] Y. Zhang, X. Zhang, J. Fang, S. Jiang, Y. Zhang, D. Gu and R. D. Nelson, "Application of SU-8 as the insulator toward a novel planar microelectrode array for extracellular neural recording," in *Proceedings of the IEEE- 5th Conference on Nano/Micro Engineered and Molecular Systems*, Xiamen, China, 2010.

[89] T. A. Nguyen, T.-I. Yin and D. R. a. G. A. Urban, "Microfluidic Chip with Integrated Electrical Cell-Impedance Sensing for Monitoring Single Cancer Cell Migration in Three-Dimensional Matrixes," *Analytical Chemistry*, vol. 85, pp. 11068-11076, 2013.

[90] C. R. Keese, J. Wegener and S. R. W. a. I. Giaever, "Electrical wound-healing assay for cells in vitro," *PNAS*, vol. 101, pp. 1554-1559, 2004.

[91] X. Y. chun, X. X. wu, D. Yong, W. Lei and C. Z. Cheng, "A review of impedance measurements of whole cells," *Biosensors and Bioelectronics*, vol. 77, p. 824–836, 2016.

[92] J. Hong, K. Kandasamy, M. Marimuthu and C. S. C. a. S. Kim, "Electrical cell-substrate impedance sensing as a non-invasive tool for cancer cell study," *The Royal Society of Chemistry*, vol. 136, pp. 237-245, 2011.

[93] H. Pick, S. Terrettaz, O. Baud, O. Laribi, C. Brisken and H. Vogel, "Monitoring proliferative activities of hormone-like odorants in human breast cancer cells by gene transcription profiling and electrical impedance spectroscopy," *Biosensors and Bioelectronics*, vol. 50, pp. 431-436, 2013.

[94] D. Klo, M. Fischer, A. Rothermel, J. C. Simonc and A. A.Robitzki, "Drug testing on 3D in vitro tissues trapped on a microcavity chip," *Lab on a Chip*, vol. 8, pp. 879-884, 2008.

[95] S. Poenick, H.-G. Jahnke, M. Eichler, S. Frost, H. Lilie and A. A.Robitzki, "Comparative label-free monitoring of immuno toxin efficacy in 2D and 3D mamma carcinoma invitro models by impedance spectroscopy," *Biosensors and Bioelectronics*, vol. 53, pp. 370-376, 2014.

[96] Y. R. F. Schmid, S. C. Bürgel, P. M. Misun, A. Hierlemann and O. Fery, "Electrical Impedance Spectroscopy for Microtissue Spheroid Analysis in Hanging-Drop Networks," *ACS Sensor*, vol. 1, pp. 1028-1035, 2016.

[97] A. Weltin, J. Kieninger, B. Enderle, A.-K. Gellner, B. Fritsch and G. A.Urban, "Polymer-based, flexible glutamate and lactate microsensors for in vivo applications," *Biosensors and Bioelectronics*, vol. 61, pp. 192-199, 2014.

[98] F. Liu, K. C. Pawan, G. Zhang and J. Zhe, "A microfluidic sensor for single cell detection in a continuous flow," in *19th International Conference on Solid-State Sensors, Actuators and Microsystems (TRANSDUCERS)*, Kaohsiung, Taiwan, 2017.

[99] C. Petchakup, K. H. H. Li and H. W. Hou, "Advances in Single Cell Impedance Cytometry for Biomedical Applications," *Micromachines*, vol. 8, pp. 1-20, 2017.

[100] W. Tang, D. Tang, Z. Ni, N. Xiang and O. H. Yi, "Microfluidic Impedance Cytometer with Inertial Focusing and Liquid Electrodes for High-Throughput Cell Counting and Discrimination," *Analytical Chemistry*, vol. 89, pp. 3154-3161, 2017.

[101] F. Weihua, Q. Miaomiao, J. Yan, Z. Hongbo, G. Yuqing, J. Qinghui and Z. Jianlong, "High efficiency single-cell capture based on microfluidics for single cell analysis," *Micromechine and Microengineer*, vol. 29, p. 035004 (6pp), 2019.

[102] S. Boddington, E. Sutton, T. Henning, A. Nedopil, B. Sennino, A. Kim and H. Daldrup-Link, "Labeling Human Mesenchymal Stem Cells with Fluorescent Contrast Agents: The Biological Impact," *Molecular Imaging and Biology*, vol. 13, pp. 3-9, 2011.

[103] E. Ragni, M. Viganò, P. Rebulla, R. Giordano and L. Lazzari, "What is beyond a qRT-PCR study on mesenchymal stem cell differentiation properties: How to Choose the Most Reliable Housekeeping Genes," *Cellular Molecular Medicine*, vol. 17, pp. 168-180, 2013.

[104] V. J. Cadarso, J. Perera-Núñez, L. Jacot-Descombes, K. Pfeiffer, U. Ostrzinski, A. Voigt, A. Llobera, G. Grützer and J. Brugger, "Microlenses with defined contour shapes," *Optics Express*, vol. 19, pp. 18665-18670, 2011.

[105] P. B. Guk, C. Kiwoon, J. C. Jin and L. H. Sup, "Micro lens-on-lens array," *Soft Matter*, vol. 8, pp. 1751-1755, 2012.

[106] D. Dan, Microlens Arrays, London: Taylor and Francis, 2001.

[107] J. S. Kim, D. S. Kim, J. J. Kang, J. D. Kim and C. J. Hwang, "Replication and Comparison of Concave and Convex Microlens Arrays of Light Guide Plate for Liquid Crystal Display in Injection Molding," *Polymer Engineering*, vol. 50, pp. 1696-1704, 2010.

[108] K. H. Koha, T. Kobayashib, F.-L. Hsiao and C. Lee, "Characterization of piezoelectric PZT beam actuators for driving 2D scanning micromirrors," *Sensors and Actuators A: Physical*, vol. 162, pp. 336-347, 2010.

[109] S. Choi, S.-H. Kim and J.-K. Park, "Optical path-length modulation for three-dimensional particle measurement in mirror-embedded microchannels," *Lab on a Chip*, vol. 10, pp. 335-340, 2010.

[110] H. Hajjoul, S. Kocanov, I. Lassadi, K. Bystricky and A. Bancaud, "Lab-on-Chip for fast 3D particle tracking in living cells," *Lab on a Chip*, vol. 9, pp. 3054-3058, 2009.

[111] A. Matsutani, M. Sato, K. Hasebe and A. Takada, "Microfabrication of Concave Micromirror for Microbial Cell Trapping Using Köhler Illumination by XeF2 Vapor Etching," *Sensors and Materials*, vol. 31, pp. 1325-1334, 2019.

[112] J. M. Hum, A. P. Siegel, F. M. Pavalko and R. N. Day, "Monitoring biosensor activity in living cells with fluorescence lifetime imaging microscopy," *International Jornal of Molecular Science,* vol. 13, pp. 14385-14400, 2012.

[113] P. Smith, C. M. Taylor, E. McCabe, D. Selviah, S.Day and L.Commander, "Switchable fiber coupling using variable-focal-length microlenses," *American Institute of Physics,* vol. 72, no. 7, pp. 3132-3134, 2001.

[114] L. Feng, C. Sihai, L. Huan, Z. Yifan, L. Jianjun and G. Yiqing, "Fabrication and characterization of polydimethylsiloxane concave microlens array," *Optics & Laser Technology,* vol. 44, no. 4, pp. 1054-1059, 2012.

[115] J. W. S. a. P. B. Astrup, "History of blood gas analysis. IV. Leland Clark's oxygen electrode," *Clinical Monitoring,* vol. 2, pp. 125-39, 1986.

[116] P. M. Misun, J. Rothe, Y. R. Schmid and A. H. a. O. Frey, "Multi-analyte biosensor interface for real-time monitoring of 3D microtissue spheroids in hanging-drop networks," *Microsystems & Nanoengineering,* vol. 2, pp. 1-9, 2016.

[117] R. Martinez-Manez, J. Soto, J. Lizondo-Sabater, E. Garcia-Breijo, L. Gil, J. Ibanez, I. Alcaina and S.Alvarez, "New potentiomentric dissolved oxygen sensors in thick film technology," *Sensor Actuator B-Chem,* vol. 101, pp. 295-301, 2004.

[118] E. O. Pettersen, P. Ebbesen and R. G. Gieling, "Targeting tumour hypoxia to prevent cancer metastasis. From biology, biosensing and technology to drug development: the METOXIA consortium," *Enzyme Inhibition and Medicinal Chemistry,* vol. 30, pp. 689-721, 2015.

[119] L.-C. Xu and C. A. Siedlecki, "Effects of surface wettability and contact time on protein adhesion to biomaterial surfaces," *Biomaterials,* vol. 28, pp. 3273-3283, 2007.

[120] A. Ruiz, L. Buzanska, D. Gilliland, H. Rauscher, L. Sirghi, T. Sobanski, M. Zychowicz, L. Ceriotti and F. Bretagnol, "Micro-stamped surfaces for the patterned growth of neural stem cells," *Biomaterials,* vol. 29, pp. 4766-4774, 2008.

[121] M. Ochsner, M. R. Dusseiller, H. M. Grandin, S. Luna-Morris, M. Textor, V. Vogelb and M. L.Smith, "Micro-well arrays for 3D shape control and high resolution analysis of single cells," *Lab on a Chip,* vol. 7, p. 1074–1077, 2007.

[122] S. A. Ruiz and C. S. Chen, "Microcontact printing: A tool to pattern," *Soft Matter,* vol. 3, p. 168–177, 2007.

[123] M. Théry, "Micropatterning as a tool to decipher cell morphogenesis and functions," *Cell Science,* vol. 123, pp. 4201-4211, 2010.

[124] A. Goessl, D. F. Bowen-Pope and A. S. Hoffman, "Control of shape and size of vascular smooth muscle cells in vitro by plasma lithography," *Biomedical Materials Research,* vol. 57, pp. 15-24, 2001.

[125] M. R. Padgen, A. Gracias, N. Tokranova, N. Cady and J. Castracane, "SU-8 Microfluidic Channels with Porous Sidewalls for Biological Applications," in *Proceeding of SPIE* , Berline, 2009.

[126] C.-J. Chang, C.-S. Yang, Y.-J. Chuang, H.-S. Khoo and F.-G. Tseng, "Micro-patternable nanoporous polymer integrated with microstructures for molecular filtration," *Nanotechnology,* vol. 19, pp. 365301-8, 2008.

[127] H. G. Duana and E. Q.Xie, "Fabrication of nanopores with subnanometer precision on poly(methyl methacrylate) nanofibers by in situ electron beam irradiation," *Journal of Vacuum Science & Technology B,* vol. 26, pp. 332-338, 2008.

[128] S. Metz, C. Trautmann, A. Bertsch and Ph Renaud, "Polyimide microfluidic devices with integrated nanoporous filtration areas manufactured by micromachining and ion track technology," *Micromechine and Microengineer,* vol. 14, p. 324–331, 2004.

[129] S. Aura, V. Jokinen, M. Laitinen, T. Sajavaara and S. Franssila, "Porous inorganic–organic hybrid material by oxygen plasma treatment," *Micromech and Microengineer,* vol. 21, p. 125003 (8pp), 2011.

[130] K. Tsougeni, A. Bourkoula, P. Petrou, A. Tserepi, S. Kakabakos and E. Gogolides, "Photolithography and plasma processing of polymeric lab on chip for wetting and fouling control and cell patterning," *Microelectronic Engineering,* vol. 124, pp. 47-52, 2014.

[131] K.-H. Haas and H. Wolter, "Synthesis, properties and applications of inorganic–organic copolymers (ORMOCER®s)," *Current Opinion in Solid State and Materials Science,* vol. 4, pp. 571-580, 1999.

[132] R. Houbertz, L. Fröhlich, M. Popall, U. Streppel, P. Dannberg, A. Bräuer, J. Serbin and B. Chichkov, "Inorganic–Organic Hybrid Polymers for Information Technology: from Planar Technology to 3D Nanostructures," *Advanced Engineering Materials,* vol. 5, p. 551–555, 2003.

[133] Karl-Heinz, H. Sabine, Amberg-Schwab and K. Rose, "Functionalized coating materials based on inorganic-organic polymers," *Thin Solid Films,* vol. 351, pp. 198-203, 1999.

[134] M. Malinauskas, P. Danilevi, D. Baltriukien, M. Rutkauskas and A. Žukauskas, "3D artificial polymeric scaffolds for stem cell growth fabricated by femtosecond laser," *Lithuanian Journal of Physics,* vol. 50, pp. 75-82, 2010.

[135] S. Schlie, A. Ngezahayo, A. Ovsianikov, T. Fabian, H.-A. Kolb, H. Haferkamp and B. N. Chichkov, "Three-Dimensional Cell Growth on Structures Fabricated from ORMOCER® by Two-Photon Polymerization Technique," *Biomaterials Applications,* vol. 22, pp. 275-287, 2007.

[136] M. Robertsson, J. Haglund and C. Johansson, "Large area patterning of high density interconnects by novel UV-excimer lithography and photo patternable ORMOCER™-dielectrica," in *Proceeding of IMAPS*, Strasbourg, France, May 2001.

[137] R. Buestrich, F. Kahlenberg, M. Popall, P. Dannberg, R. Müller-Fiedler and O. Rösch, "ORMOCER®s for Optical Interconnection Technology," *Sol-Gel Science and Technology,* vol. 20, p. 181–186, 2001.

[138] A. Sivakumar and A. Valiathan, "Dental Ceramics and Ormocer Technology - Navigating the Future," *Trends Biomaterial Artificial Organ,* vol. 20, pp. 40-43, 2006.

[139] Z. L. Chen, W. Chen, B. Yuan, L. Xiao, D. B. Liu, Y. Jin, B. G. Quan, J. O. Wang, K. Ibrahim, Z. Wang, W. Zhang and X. Y. Jiang, "In Vitro Model on Glass Surfaces for Complex Interactions between Different Types of Cells," *Langmuir* , vol. 26, p. 17790– 1, 2010.

[140] T. Sikanen, S. Aura, L. Heikkilä, T. Kotiaho, S. Franssila and R. Kostiainen, "Hybrid Ceramic Polymers: New, Nonbiofouling, and Optically Transparent Materials for Microfluidics," *Analytical Chemistry,* vol. 82, p. 3874–3882, 2010.

[141] L. Jacot-Descombes, V. J. Cadarso, A. Schleunitz, S. Grützner, J. J. Klein, J. Brugger, H. Schift and G. Grützner, "Organic-inorganic-hybrid-polymer microlens arrays with tailored optical characteristics and multi-focal properties," *Optical Express,* vol. 23, pp. 25365-76, 2015.

[142] S. Aura, T. Sikanen, T. Kotiaho and S. Franssila, "Novel hybrid material for microfluidic devices," *Sensors and Actuators B: Chemical,* vol. 32, no. 2, pp. 397-403, 16 June 2008.

[143] R. Daunton, A. J. Gallant and D. Wood, "Manipulation of exposure dose parameters to improve production of high aspect ratio structures using SU-8," *Micromechanics and Microengineering,* vol. 22, p. 075016, 2012.

[144] Y.-J. Chang, K. Mohseni and V. M.Bright, "Fabrication of tapered SU-8 structure and effect of sidewall angle for a variable focus microlens using EWOD," *Sensors and Actuators A: Physical,* vol. 136, pp. 546-553, 2007.

[145] R. A. Serway, "Principles of Physics (2nd ed.)," Fort Worth, Texas, London: Saunders College Pub. , 1998, p. p. 602.

[146] D. Griffiths, "Introduction to Electrodynamics (3rd ed.)," New Jersey, Upper Saddle River, Prentice Hall., 1999, p. 286.